

### **Photocopy and Use Authorization**

In presenting this thesis in partial fulfillment of the requirements for an advanced degree at Idaho State University, I agree that the Library shall make it freely available for inspection. I further state that permission for extensive copying of my thesis for scholarly purposes may be granted by the Dean of the Graduate School, Dean of my academic division, or by the University Librarian. It is understood that any copying or publication of this thesis for financial gain shall not be allowed without my written permission.

Signature \_\_\_\_\_

Date \_\_\_\_\_

**CONSTRUCTION AND TESTING OF A POSITRON  
ANNIHILATION LIFETIME SPECTROMETER**

by

Brian M. Wieland

A thesis  
submitted in partial fulfillment  
of requirements for the degree of  
Masters of Science in the Department of Physics  
Idaho State University  
August 2012

To the Graduate Faculty:

The members of the committee appointed to examine the thesis of Brian M. Wieland find it satisfactory and recommend that it be accepted.

---

Dr. Dustin McNulty,  
Major Advisor

---

Dr. Erdinch Tatar  
Committee Member

---

Dr. Andrew Holland  
Graduate Faculty Representative

*To those who dared to reach beyond*

## ACKNOWLEDGMENTS

The author would like to thank his advisor, Dr. Dustin McNulty, for his expertise, advice, and tireless efforts to locate the necessary resources for the completion of this project. Without his help, I would have never had the opportunity to see the completion of this project. I would also like to thank Dr. Erdinch Tatar and my Graduate Faculty Advisor Dr. Andrew Holland for serving on my committee and offering many helpful suggestions on my thesis.

I would also like to extend heartfelt gratitude to Dr. Marcus Gagliardi for sharing his knowledge of positron and radiation detection physics, as well as his advice on annealing techniques for the materials used in this study. Additionally, I would like to thank Dr. Vesselin Dimitrov for his help with the accelerators. Although I have never met him in person, I would like to thank Dr. Jerzy Kansy for his assistance with understanding the LT10 software used in this study for data analysis, as well as Dr. Jagoda Urban-Klaehn for her assistance with understanding the fundamentals of the LT software and for donating the nickel samples used in this study. I would also like to thank the accelerator operators at the Idaho Accelerator Center for their assistance with ensuring the operation of the Pelletron for preliminary tests.

A variety of students have helped in various stages of the completion of this work. I would like to thank Edward Reedy for his help in teaching me how to calibrate the ADCs and Anna Hoskins for her help in understanding gamma spectroscopy and her friendship. I would like to thank Carlos Bula and Benjamin Satterwhite for teaching me how to anneal the materials and for cutting the thin disks used in this study.

Finally, I would like to thank my friends, classmates, and family for helping push me to work harder both in and out of the classroom, as well as being there for me during the rougher periods of graduate school. It has been an experience that I shall likely not forget.

## TABLE OF CONTENTS

	Page
List of Figures . . . . .	x
List of Tables . . . . .	xi
Abstract . . . . .	xii
1 Introduction . . . . .	1
1.1 Historical Perspective . . . . .	1
1.2 Discussion of Relevant Studies . . . . .	2
1.3 Research Goals of Study . . . . .	3
2 Theory . . . . .	5
2.1 Radionuclide Decay . . . . .	5
2.2 Proton Capture Reaction . . . . .	6
2.2.1 Accelerator Timing Coincidence Rate Estimates . . . . .	9
2.3 Photon Interactions with Matter . . . . .	14
2.3.1 Photoelectric Effect . . . . .	16
2.3.2 Compton Scattering . . . . .	16
2.3.3 Pair Production . . . . .	18
2.4 Positron Interactions with Matter . . . . .	19
2.4.1 Thermalization . . . . .	19
2.4.2 Diffusion . . . . .	20
2.4.3 Trapping . . . . .	22
2.4.4 Positron Annihilation . . . . .	23
2.5 Fundamentals of PALS . . . . .	25
2.5.1 Positron Lifetimes in Materials . . . . .	26
2.6 Gamma Spectroscopy . . . . .	28
2.6.1 Compton Spectrum . . . . .	29
2.6.2 Full Energy Peaks . . . . .	30
3 Materials and Methods . . . . .	32
3.1 Positron Sources . . . . .	32
3.1.1 $^{22}\text{Na}$ Source Positrons . . . . .	32
3.1.2 Accelerator-Induced Positrons . . . . .	33
3.2 Detection Equipment . . . . .	35
3.2.1 Scintillators . . . . .	35
3.2.2 Photomultiplier Tubes . . . . .	37

3.3	Calibration of Equipment . . . . .	39
3.3.1	Photomultiplier Tubes . . . . .	39
3.3.2	Constant Fraction Discriminator . . . . .	41
3.3.3	Analog to Digital Converter . . . . .	44
3.3.4	Time to Amplitude Converter . . . . .	46
3.3.5	Amplifiers . . . . .	48
3.3.6	Gate and Delay Generators . . . . .	48
3.3.7	ADC Timing and Energy Calibrations . . . . .	50
3.4	Determination of Optimal Timing Resolution . . . . .	53
3.5	Determination of Detector Energy Resolution . . . . .	54
3.6	Discrimination Window Settings . . . . .	56
3.6.1	Source-Based Experiments . . . . .	56
3.6.2	Accelerator-Based Experiments . . . . .	57
3.7	Metallic Samples . . . . .	59
3.7.1	Aluminum . . . . .	60
3.7.2	Nickel . . . . .	60
3.7.3	Copper . . . . .	60
3.7.4	Lead . . . . .	61
3.7.5	Summary of Positron Lifetimes in Materials . . . . .	61
3.8	Annealing of Materials . . . . .	62
4	Data Analysis and Results . . . . .	64
4.1	The LT10 Software Package . . . . .	64
4.2	Prompt $^{60}\text{Co}$ Gamma Distribution . . . . .	66
4.3	Radionuclide Source . . . . .	67
4.3.1	Fast Plastic Scintillator . . . . .	67
4.4	Summary of Results . . . . .	78
5	Discussion and Conclusion . . . . .	81
5.1	Discussion of Results . . . . .	81
5.1.1	Fast Plastic Scintillators . . . . .	81
5.1.2	$\text{BaF}_2$ Scintillators . . . . .	83
5.2	Recommendations Based Upon Results . . . . .	83
5.3	Future Work . . . . .	85
	REFERENCES . . . . .	87

## LIST OF FIGURES

	Page
2.1 The decay schemes for the $^{22}\text{Na}$ , $^{137}\text{Cs}$ , and $^{60}\text{Co}$ radionuclides used in PALS experiments [12] . . . . .	6
2.2 Using the Coulomb potential well as a model, a positron is electrically repelled by areas of positive potential and seeks less positive potentials. Eventually, the positron annihilates with a valence electron and emits a pair of 511 keV gammas. . . . .	7
2.3 Photon energy spectrum of the $^{27}\text{Al}(p, \gamma)^{28}\text{Si}$ reaction as seen using a high-purity germanium detector. . . . .	8
2.4 Interaction cross-sections of the $^{27}\text{Al}(p, \gamma)^{28}\text{Si}$ reaction for various proton energies [23] . . . . .	9
2.5 Mass interaction coefficients as a function of photon energy for (a) Polyvinyltoluene and (b) $\text{BaF}_2$ scintillators. These show the three major processes by which photons interact with matter [2]. . . . .	14
2.6 (a) Compton Scattering as seen from the laboratory frame. (b) The Feynman diagram depicts Compton Scattering as a quantum electrodynamical process . . . . .	17
2.7 (a) Pair production as seen in the laboratory frame. (b) From the Feynman diagram, pair production is another example of a quantum electrodynamical interaction. . . . .	18
2.8 (a) The energy spectrum of positrons emitted from a $^{22}\text{Na}$ as a function of intensity. Positrons are emitted with an average energy of 194.9 keV, which upon thermalization in a material is reduced to an energy of less than 0.1 eV. (b) These positrons typically only travel about 0.1 mm into a sample. . . . .	20
2.9 Feynmen diagrams of positron annihilation . . . . .	25

2.10	Theoretical spectrum produced in gamma spectroscopy experiments. As products of pair-production within the scintillator, the creation of the single and double escape peaks requires incident photons of energies greater than 1.022 MeV. More specifically for BaF <sub>2</sub> and fast plastic scintillators, the incident photon energies must be greater than approximately 2.5 MeV, as seen in Fig. 2.5. Otherwise, only the Compton continuum and Compton edge will be visible, with the full-energy photopeak additionally visible with BaF <sub>2</sub> scintillators. . . . .	29
2.11	A comparison of the <sup>22</sup> Na energy spectrum as seen by the fast plastic and BaF <sub>2</sub> scintillators. . . . .	31
3.1	(a) The <sup>22</sup> Na source and surrounding Kapton tape. (b) The <sup>22</sup> Na source is sandwiched between the sample materials when completing source-based studies . . . . .	33
3.2	Experimental configuration of photomultiplier tubes when completing source-based studies . . . . .	39
3.3	Determination of spectrometer timing resolution as a function of the detector bias for the (a) fast plastic and (b) BaF <sub>2</sub> scintillators using Hamamatsu R3377 photomultiplier tubes. This plot is used to determine the optimal settings of the bias on each detector. The FWHM refers to the FWHM of the timing peak created by the START 1173.2 keV and STOP 1332.5 keV decay gammas of <sup>60</sup> Co. . . . .	40
3.4	The optimization of the timing resolution as a function of CF Delay Cable lengths for the (a) fast plastic and (b) BaF <sub>2</sub> scintillators using Hamamatsu R3377 photomultiplier tubes . . . . .	44
3.5	Flow chart of PALS system setup to perform calibration of ADC . . . . .	45
3.6	Flow chart of PALS system setup to perform calibration of Time to Amplitude Converter . . . . .	46
3.7	MPA-NT output from PALS with fast plastic scintillators to perform calibration of Time to Amplitude Converter . . . . .	47
3.8	Flow chart of PALS system setup to perform calibration of Amplifiers . . . . .	49
3.9	Flow chart of PALS system set up to perform calibration of Gate and Delay Generators . . . . .	50
3.10	Images of the (a) unadjusted and (b) adjusted Gate and Delay Generator as seen on Tektronix TDS 2024 oscilloscope . . . . .	51
3.11	Flow chart of PALS system set up to perform energy calibration of MPA-NT software and perform positron lifetime measurements . . . . .	52
3.12	The resultant energy spectrum of <sup>137</sup> Cs as seen by the fast plastic and BaF <sub>2</sub> scintillators. . . . .	55
3.13	The energy spectrum of <sup>22</sup> Na before and after setting discrimination windows when using the fast plastic scintillators. Fig. 3.13a and 3.13b depict the energy spectrum of <sup>22</sup> Na before setting discrimination windows while Fig. 3.13c and 3.13d depict the energy spectrum with the proper discrimination windows applied. . . . .	57

3.14	The annealing profile for (a) aluminum, (b) nickel, and (c) copper materials used in PALS experiments . . . . .	63
4.1	Prompt $^{60}\text{Co}$ resolution curves for the PALS system with (a) conical fast plastic and (b) $\text{BaF}_2$ scintillators. The timing resolution with the conical fast plastic scintillator is found to be $170.17 \pm 0.73$ ps and the timing resolution with the $\text{BaF}_2$ scintillator is found to be $213.34 \pm 1.79$ ps. These were fit as a single Gaussian with the background fit provided by the MPA-NT software. . . . .	67
4.2	Experimental $^{22}\text{Na}$ lifetime data with no sample used with thin foil experiments. . . . .	69
4.3	Experimental $^{22}\text{Na}$ lifetime data with no sample used with $\sim 1$ mm thick disk experiments. . . . .	70
4.4	Experimental results of (a) annealed and (b) unannealed aluminum foils using $^{22}\text{Na}$ source. . . . .	71
4.5	Experimental results of (a) annealed and (b) unannealed aluminum disks using $^{22}\text{Na}$ source. . . . .	73
4.6	Experimental results of annealed nickel foils using $^{22}\text{Na}$ source. This material is the same sample that was accidentally oxidized in Fig. 4.7b, tested, and annealed again to remove the oxidation. . . . .	74
4.7	Experimental results of (a) unannealed, and (b) oxidized nickel foils using $^{22}\text{Na}$ source. Both samples of nickel are reported to have a purity of 99.9994%. However, the material history is unknown. The second sample shown in Fig. 4.7b was accidentally oxidized during the annealing process. . . . .	75
4.8	Experimental results of (a) annealed and (b) unannealed copper foils using $^{22}\text{Na}$ source. The copper foils used in this study have an unknown material purity. The discrepancy in the theoretical to experimental data fits of the annealed copper may be the result of an additional lifetime component not accounted for in the data analysis. The disagreement is very slight and likely does not affect the reduced $\chi^2$ . . . . .	76
4.9	Experimental results of (a) annealed and (b) unannealed copper disks using $^{22}\text{Na}$ source. . . . .	77
4.10	Source-based lifetime data with lead foil sample . . . . .	78

## LIST OF TABLES

	Page
2.1 Data used in coincident rate calculation. . . . .	15
3.1 Theoretical and experimental positron lifetimes in picoseconds of materials under study. . . . .	62
3.2 Melting and annealing points of materials under study . . . . .	62
4.1 Positron lifetimes and intensities of Kapton tape and background as determined by this study. . . . .	79
4.2 Bulk and defect positron lifetimes in foils as determined by this study. The bulk positron lifetimes refer to the positron lifetimes as found in the annealed materials while the defect positron lifetimes refer to the positron lifetimes as found in the unannealed materials. As the lead is a self-annealing material, no data was collected to find the defect positron lifetimes. The oxidized nickel was oxidized during the process of annealing, resulting in a defect positron lifetime near the bulk lifetime literature value. No history of either nickel materials is known. . . . .	79
4.3 Bulk and defect positron lifetimes in disks as determined by this study. The bulk positron lifetimes are in excellent agreement with accepted literature values. . . . .	79
4.4 Statistical and rate information for data collection . . . . .	80
5.1 Comparison of current literature positron lifetimes to experimentally determined values in picoseconds of materials under study. . . . .	81

## ABSTRACT

Positron Annihilation Lifetime Spectroscopy (PALS) is a nuclear technique that was developed in the 1970s as a method to assess defects in materials. This technique has tremendous potential as a powerful tool for non-destructive quantification of the types and densities of defects within solids. Following the injection of positrons into a solid material, the positrons pair-annihilate at a rate dependent upon the density of electrons near the injection site. If there are lattice vacancies or dislocation defects near the injection site, the positrons are attracted to these areas, which have lower electron densities and thus give rise to longer positron lifetimes. Typical positron lifetimes in defect-free conductor-type metals are  $\sim$ 100 ps, while lifetimes within defect regions are  $\sim$ 200 ps. In order to discern between these minute lifetime differences, a spectrometer with very good timing resolution has been constructed and optimized. The capabilities of the spectrometer have been tested using a  $^{22}\text{Na}$  positron emitter by performing source-based measurements of positron lifetimes in high-purity samples of aluminum, nickel, copper, and lead. Test results are in excellent agreement with currently accepted literature values, thus validating the apparatus and data analysis technique. This study is an important first step towards the development of a modern positron annihilation lifetime spectrometer for use in accelerator-based, gamma-induced positron annihilation spectroscopy (AG-PAS).

---

CHAPTER  
**ONE**

---

INTRODUCTION

## 1.1 Historical Perspective

A series of important discoveries occurred within a relatively short period of time of two or three decades which allowed for the technique of positron annihilation spectroscopy to be developed. The first such event begins with Paul Dirac, an English theoretical physicist, who laid the groundwork for much of modern day atomic, nuclear and particle physics through the then newly developed fields of quantum mechanics and quantum electrodynamics. Upon solving the relativistic wave equation, Dirac in 1931 arrived at

$$E^2 = m^2 c^4 + p^2 c^2 \quad (1.1)$$

where E is the energy eigenvalue of a particle, m is the particle rest mass, p is the particle linear momentum and c is the speed of light. While most physicists of the time dismissed the negative energy solution of the energy eigenvalue as a non-physical solution, Dirac came to a different conclusion and postulated the existence of both particles and their anti-particles. This prediction motivated the first experimental discovery of the anti-particle of an electron, the positron, in 1932 by Anderson using a cloud chamber while studying cosmic radiation [5, 6, 13].

It was the Dirac equation, published in 1928, which allowed for Dirac, Heitler and Sauter in 1933 to calculate cross-sections of electron-positron annihilation using quantum electrodynamics. It also motivated studies into the phenomenon of pair production, which was first observed in a cloud chamber in 1932 by Blackett and

Occhialimi and then studied more in-depth on a theoretical basis independently by Nishina and Tomonaga, Oppenheimer and Plesset, and Heitler and Sauter in 1933 [5, 6].

With the theoretical framework of the positron, pair production and positron annihilation established, advancements in the area of gamma spectroscopy allowed for study of the finer details of what would become positron annihilation spectroscopy. An accurate measurement of the energy and width of the 511 keV annihilation peak was made in 1949 by DuMond, Lind, and Watson using a crystalline scintillator spectrometer. The width of this peak was correctly identified by their group as being the result of Doppler broadening. In that same year, DeBenedetti's research group correctly attributed the slight deviation from 180° between positron annihilation gammas to the thermalization of the positron within materials [6].

These discoveries paved the way for using the technique of Positron Annihilation Spectroscopy as a means to glean information regarding defects of materials on the atomic level.

## 1.2 Discussion of Relevant Studies

Positron Annihilation Lifetime Spectroscopy (PALS) is a well-known technique for non-destructive testing of defect densities within various materials, which has been in use since the late 1960s [27]. Thus far, the technique has been studied extensively using a positron emitting source, such as  $^{22}\text{Na}$ , but due to the low penetration depth of these source positrons within materials, on the order of 1 nm to a few micrometers, this application of the technique can only be used for determining surface-defects of materials [6]. Destructive testing has been studied by means of photon activation of samples and then applying PALS techniques; however, as the name suggests, the sample then becomes radiation damaged and is often unable to be returned to its original condition for functional use [44]. Studies have been completed using linear accelerators to produce positron beams for deep-defect analysis of materials, but linear accelerators are often cumbersome, resource-demanding, and cannot easily be used in field studies of larger objects. This method typically requires a sample of the material to be removed from the original structure, brought to a laboratory, and tested [6]. In the case of bridges, aircraft, steel structural foundations, and other bulky objects, this is simply not feasible. With advancements in accelerator

technology, it may be possible to effectively use compact accelerators in such field testing.

Taking advantage of current technology, a continuous wave proton-accelerator of sufficient energy may be designed to be much more portable thus able to be used in field studies. Unlike pulsed-power accelerators, a continuous wave proton-accelerator has a high duty factor which allows for cleaner signal acquisition and a higher rate of beam flux. This higher rate is extremely beneficial due to the coincidence nature of the measurements. Since there have been no known studies of using a Van de Graaff or Pelletron accelerator in conjunction with PALS techniques, this will be an important first step in determining the feasibility of using such an accelerator in deep-defect analysis of materials.

### 1.3 Research Goals of Study

This study is to be considered an important first step towards determining the feasibility of using PALS techniques in conjunction with a continuous wave accelerator. The goal of this study is to construct a modern positron annihilation lifetime spectrometer and test its capabilities in extracting bulk and monovacancy positron lifetimes from a variety of materials. These extracted lifetimes are then compared to common literature values, thus verifying the ability of the apparatus to reproduce known positron lifetimes in materials. Using this study as a baseline, it will next be possible to determine if continuous wave accelerators, such as a Van de Graaff or Pelletron, can be used in conjunction with Positron Annihilation Lifetime Spectroscopy for the purposes of deep-defect assessments of metals by means of the analysis of positron lifetimes within microdefects within metals. In order to achieve this, a positron annihilation lifetime spectrometer is built through the consideration and optimization of various nuclear instrumentation analysis designs [17, 25, 32, 44]. Studies are conducted using a  $15 \mu\text{Ci}$   $^{22}\text{Na}$  source to reproduce known positron lifetimes within samples of aluminum, nickel, copper, and lead, each with a purity of at least 99.999%, using the experimental setup.

This paper is broken down into several sections for the reader. Chapter 2 discusses the theoretical standing of Positron Annihilation Lifetime Spectroscopy, beginning with a simple discussion of radioactive decay, moving into photon and positron interactions with matter and ending with a discussion of how each of these processes

are involved in PALS. A discussion of the features of low-energy gamma spectra is also included to familiarize the reader with relevant portions of gamma spectroscopy. Chapter 3 discusses the specific equipment used in this spectrometer and the calibration of said equipment, as well as information regarding the positron sources, materials tested and method of extracting positron lifetimes from the resultant timing coincidence spectrum. Chapter 4 presents the results of experiments performed using this spectrometer and finally Chapter 5 gives an overview of the information presented in this paper with an outline of future progress which may be able to be carried out based upon the results of this study.

---

CHAPTER  
**TWO**

---

**THEORY**

## 2.1 Radionuclide Decay

The three major processes by which radionuclides decay are through alpha-, beta-, and gamma-decay. From elementary nuclear physics, it is known that alpha decay involves emission of an alpha particle, a  ${}^4_2\text{He}^{2+}$  nucleus, from the parent nucleus. Beta decay involves an isobaric transition in the atom, resulting in the loss of either an electron ( $\beta^-$  decay) or a positron ( $\beta^+$  decay), and gamma decay involves the loss of excess excitation energy through the release of a gamma ray [12].

The decay scheme is a chart, as shown in Fig. 2.1, which depicts the emission of any alphas, betas, or gammas from a parent radionuclide to a daughter nucleus. Typically this results in a transition to the lowest energy state, known as the ground state, of the daughter nucleus. In the case of decay through gamma emissions, single transitions from the parent radionuclide to the ground state of the daughter nucleus do occur, but more frequent is multiple decay modes in which gamma rays are emitted to transition from higher to lower excited states until reaching the ground state of the daughter nucleus. An example of such decay process is seen with  ${}^{60}\text{Co}$ , depicted in Fig. 2.1c.

A decay scheme usually details the half-life of the parent radionuclide and the branching ratios, or probability of occurrence, for each decay mode [12]. The branching ratio is defined as

$$\Gamma_i = k_i / (k_1 + k_2 + \dots + k_i + \dots) = k_i / k \quad (2.1)$$

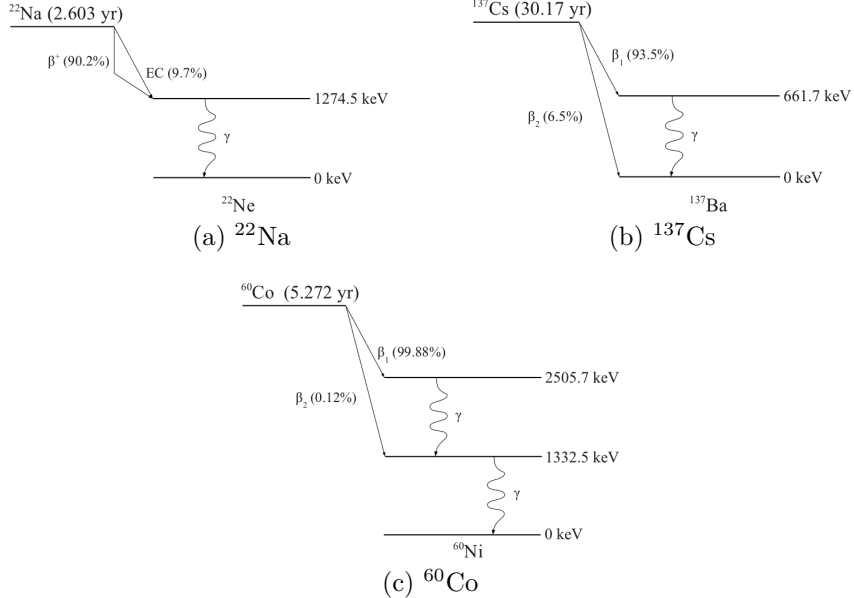


**Figure 2.1:** The decay schemes for the  $^{22}\text{Na}$ ,  $^{137}\text{Cs}$ , and  $^{60}\text{Co}$  radionuclides used in PALS experiments [12]

where  $\Gamma_i$  is the branching ratio for the  $i^{th}$  decay mode,  $k_i$  is the probability that the radionuclide decays by the  $i^{th}$  decay mode, and  $k$  is the total decay constant for the decay of the parent nuclide [13]. Figures 2.1a, 2.1b, and 2.1c depict the decay schemes for  $^{22}\text{Na}$ ,  $^{137}\text{Cs}$ , and  $^{60}\text{Co}$ , respectively. These decay schemes become important in Sec. 3.3 as a means to calibrate the various nuclear instrumentation modules (NIMs) and data acquisition systems used in PALS.

## 2.2 Proton Capture Reaction

Before beginning discussion on the proton capture reaction, a brief introduction to the nucleus is required in order to discuss the interactions of the proton with a nucleus.

A decent approximation of the proton-nucleon interaction in terms of the electric potential is seen in Fig. 2.2. Beginning from  $r = \infty$  and moving as  $r \rightarrow 0$ , an incoming proton first interacts with the Coulomb field of the nucleus. As the proton approaches the nucleus, the repulsive forces between the proton and nucleus increase,

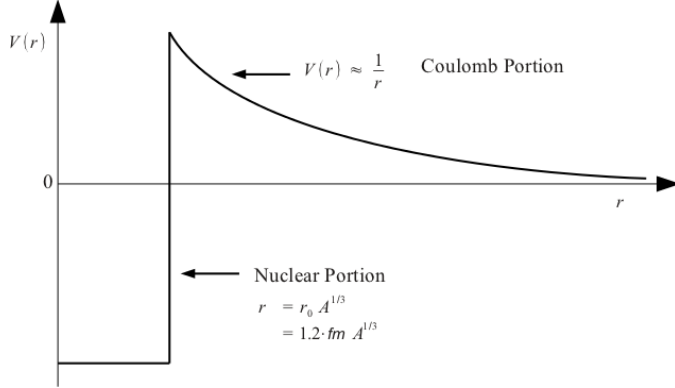


**Figure 2.2:** Using the Coulomb potential well as a model, a positron is electrically repelled by areas of positive potential and seeks less positive potentials. Eventually, the positron annihilates with a valence electron and emits a pair of 511 keV gammas.

as seen with the potential

$$U(r) = \frac{1}{4\pi\epsilon_0} \frac{Z_1 Z_2 e^2}{R} \quad (2.2)$$

where  $\epsilon_0$  is the permittivity of free space,  $Z_1$  and  $Z_2$  are the atomic numbers of the incident particle and the target nucleus, respectively,  $e$  is the charge of the proton, and  $R$  is the distance of the incident particle from the nucleus, approximated by

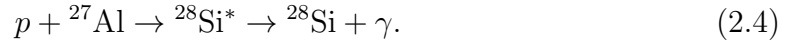
$$\begin{aligned} R &= R_0 A^{1/3} \\ &= 1.2 \text{ fm } A^{1/3}, \end{aligned} \quad (2.3)$$

with  $A$  being defined as the number of protons and neutrons in the target nucleus.

At a distance  $R = R_0 A^{1/3}$  from the nucleus, an incoming proton with enough energy to either overcome or quantum mechanically tunnel through the Coulomb field of the nucleus enters what is known as the potential well of the nucleus. Once the proton has entered this potential well, it is capable of interacting with the nucleus itself [24].

The Pelletron is capable of accelerating protons from a hydrogen source bottle up to an energy of 4 MeV. However, an energy of 1.5 MeV is used in this study due to radiation shielding considerations and a lack of cross-section gain between 1 MeV and 4 MeV as seen in Fig. 2.4. These energetic protons collide with an aluminum target, creating an excited state of silicon in a process known as proton-capture. The

excited silicon then gamma decays, in which it releases multiple gammas of energies above the pair-production minimum of 1.022 MeV. While any gamma of energy above  $2m_ec^2$  has the ability to pair produce within the sample material, the decay mode branches of interest produces multiple gammas of energies 1.78 MeV and higher. An example of this process is summarized in the reaction



Through the application of Eq. 2.2, it is seen that in order for a proton to be captured by an aluminum nucleus ( $Z = 13$ ,  $A = 27$ ), it must have a total energy of approximately 5.2 MeV. As the Pelletron accelerates the proton to an energy of 1.5 MeV, this indicates that in order for proton capture to occur within the aluminum target nuclei, the protons must quantum mechanically tunnel through the Coulomb barrier.

From Fig. 2.3, it is seen that there are many gammas produced in the  ${}^{27}\text{Al}(p, \gamma){}^{28}\text{Si}$  reaction which are capable of producing electron-positron pairs. To summarize, the purpose for using this reaction in PALS measurements is that some of these high energy gammas will enter the sample and create a positron within the sample by means of pair-production.

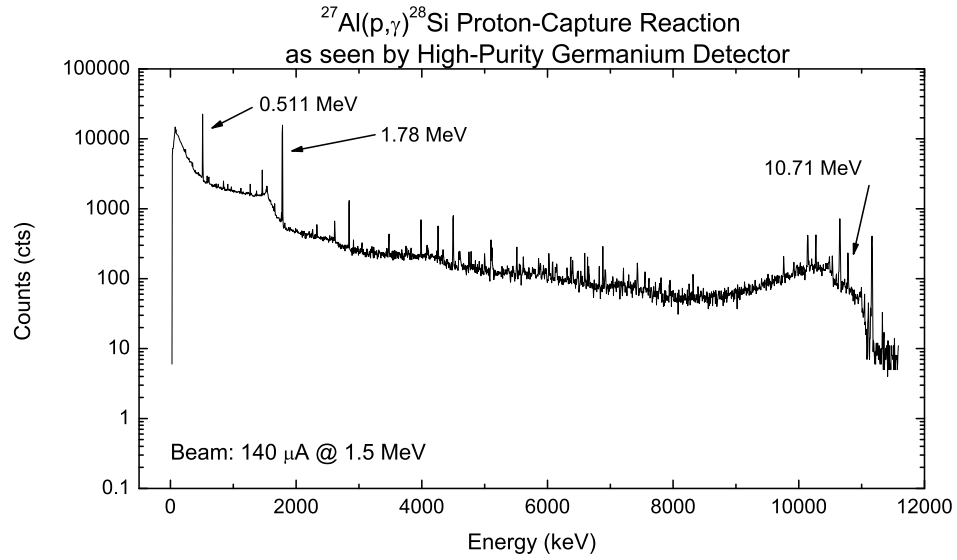


**Figure 2.3:** Photon energy spectrum of the  ${}^{27}\text{Al}(p, \gamma){}^{28}\text{Si}$  reaction as seen using a high-purity germanium detector.

It should be noted that the prominent 511 keV peak as seen in Fig. 2.3 is the result

of the high-purity germanium detector setup which incorporates heavy shielding. For the PALS measurements, the greatest contribution to the 511 keV signal will come from annihilation photons from within the material, rather than from background related to the experimental setup.

Using Fig. 2.4 as a reference, the protons exiting the Pelletron with an energy of 1.5 MeV have a capture cross-section of approximately 6  $\mu\text{b}$  with the  $^{27}\text{Al}$  target [31]. From this value, it is possible to determine the rate of gammas emitted from de-excitation of  $^{28}\text{Si}^*$ . Fig. 2.3 shows the distribution of photon energies resultant from the  $^{27}\text{Al}(p, \gamma)^{28}\text{Si}$  reaction.

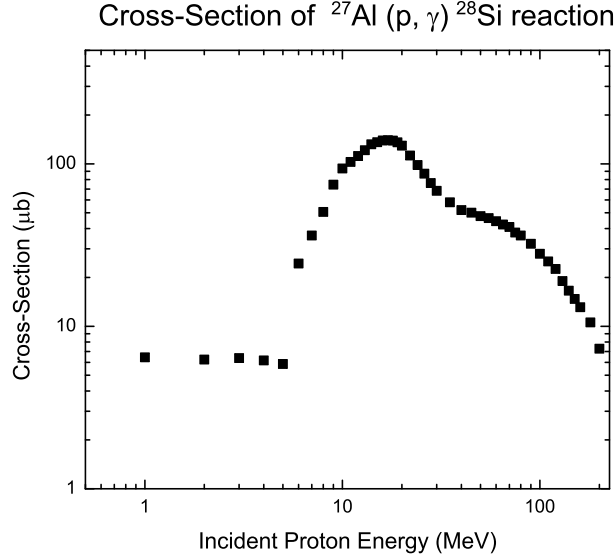


**Figure 2.4:** Interaction cross-sections of the  $^{27}\text{Al}(p, \gamma)^{28}\text{Si}$  reaction for various proton energies [23]

### 2.2.1 Accelerator Timing Coincidence Rate Estimates

Assuming all protons hit the aluminum target, the rate of excited silicon atoms created in the proton capture reaction is given by:

$$\text{Rate}_{\text{Si}^*} = \phi_p \cdot N_{\text{Al}} \cdot \sigma_{\text{capture}}, \quad (2.5)$$

where  $\phi_p$  is the incident proton flux,  $N_{\text{Al}}$  is the number of atoms per  $\text{cm}^2$  of the aluminum target, and  $\sigma_{\text{capture}}$  is the cross-section of the  $^{27}\text{Al}(p, \gamma)^{28}\text{Si}$  reaction at a

given incident proton energy. More specifically,  $\phi_p$  is given by

$$\phi_p = \frac{I_{\text{beam}}}{e}, \quad (2.6)$$

where  $I_{\text{beam}}$  is the current of the accelerator beam and  $e$  is the elementary charge of an electron. Given a beam current of  $200 \mu\text{A}$ ,  $\phi_p \sim 1.25 \cdot 10^{15}$  protons/s. The number of atoms per  $\text{cm}^2$  of the aluminum target,  $N_{\text{Al}}$ , is given by

$$N_{\text{Al}} = \rho_{\text{Al}} \cdot t_{\text{Al}} \cdot \frac{N_A}{A_{\text{Al}}}, \quad (2.7)$$

where  $\rho_{\text{Al}}$  is the density of aluminum in  $\text{g/cm}^3$ ,  $t_{\text{Al}}$  is the thickness of the aluminum target in cm,  $N_A$  is Avogadro's number, and  $A_{\text{Al}}$  is the atomic mass of aluminum. Given  $t_{\text{Al}} = 0.635 \text{ cm}$ ,  $N_{\text{Al}} = 3.83 \cdot 10^{22} \text{ atoms/cm}^2$ . Finally,  $\sigma_{\text{capture}}$  is given in Fig. 2.4 to be approximately  $6 \mu\text{b}$  for proton energies between 1 and 6 MeV. This gives an estimated rate of excited silicon production to be  $2.87 \cdot 10^8 \text{ atoms/s}$ .

The excited silicon then de-excites and emits gammas of various energies isotropically. The spectrum of these gammas is shown in Fig. 2.3. The rate of gammas produced in the  $^{27}\text{Al}(p, \gamma)^{28}\text{Si}$  reaction entering the sample is

$$\text{Rate}_{\gamma \text{ in sample}} = \text{Rate}_{\text{Si}^*} \cdot \Omega_{\text{sample}}, \quad (2.8)$$

where  $\Omega_{\text{sample}}$  is the solid angle of the sample. In general, solid angle is defined as

$$\Omega = 4\pi \int \frac{da}{4\pi R^2} = \frac{A}{R^2}, \quad (2.9)$$

with  $A$  representing the area of the detector and  $R$  representing the distance from the source to the detector [24]. The solid angle of a conical region of space is described by

$$\Omega = 2\pi(1 - \cos \theta), \quad (2.10)$$

where the angle  $\theta$  is described by

$$\theta = \tan^{-1} \left( \frac{r_a}{R_s} \right). \quad (2.11)$$

In Eq. 2.11,  $r_a$  represents the radius of the detector or sample and  $R_s$  is the distance to the center of the source. Assuming the sample material to be 2 cm away from the

aluminum target,  $\Omega_{\text{sample}}$  is approximated to be 0.29 sr. Thus, the rate of production of gammas entering the sample is  $8.44 \cdot 10^7$  atoms/s.

Once the resultant gammas from the  $^{27}\text{Al}(p, \gamma)^{28}\text{Si}$  reaction have entered the sample, the positron production rate within the sample is given by

$$\text{Rate}_{e^+} = \text{Rate}_{\gamma \text{ in sample}} \cdot N_{\text{sample}} \cdot \sigma_{e^+ e^-}, \quad (2.12)$$

where  $N_{\text{sample}}$  is the number of atoms per  $\text{cm}^2$  of the sample and  $\sigma_{e^+ e^-}$  is the pair-production cross-section within a material (See Sec. 2.3.3). Similar to Eq. 2.7,  $N_{\text{sample}}$  is given as

$$N_{\text{sample}} = \rho_{\text{sample}} \cdot t_{\text{sample}} \cdot \frac{N_A}{A_{\text{sample}}}, \quad (2.13)$$

where  $\rho_{\text{sample}}$  is the density of the sample in  $\text{g/cm}^3$ ,  $t_{\text{sample}}$  is the thickness of the sample material in cm,  $N_A$  is Avogadro's number, and  $A_{\text{sample}}$  is the atomic mass of the sample. Using a lead rod of length 12 cm as an example material,  $N_{\text{sample}} = 9.89 \cdot 10^{22}$  atoms/ $\text{cm}^2$ . The pair-production cross-section within a material,  $\sigma_{e^+ e^-}$ , can be approximated using the Unscreened Born Approximation [33]. This is given as

$$\sigma_{e^+ e^-} = \alpha Z^2 r_0^2 \frac{2\pi}{3} \left( \frac{k-2}{k} \right)^3 \left[ 1 + \frac{\epsilon}{2} + \frac{23\epsilon^2}{40} + \frac{11\epsilon^3}{60} + \frac{29\epsilon^4}{960} \right], \quad (2.14)$$

where

$$k = \frac{E_\gamma}{m_e c^2}, \quad (2.15)$$

and

$$\epsilon = \frac{2k-4}{2+k+2\sqrt{2k}}. \quad (2.16)$$

In Eq. 2.14,  $\alpha$  is the fine structure constant,  $Z$  is the atomic number of the material in which the pair production is occurring,  $r_0$  is the classical electron radius,  $k$  is given by Eq. 2.15 and  $\epsilon$  is given by Eq. 2.16. Substituting Eqs. 2.14 and 2.13 into Eq. 2.12 and using lead as our sample, the cross-section of pair-production within the example lead rod is calculated to be 6.47 b for incident photon energies of 4.0 MeV. Substituting the information gained from Eq. 2.14 and 2.13 into Eq. 2.12, the rate of positron production within the sample is estimated to be  $4.70 \cdot 10^7$  positrons/s.

Using the information in Eq. 2.12, the rate of 511 keV gamma detection as seen

by the START photomultiplier tube is given by:

$$\text{Rate}_{\text{START}} = \text{Rate}_{e^+} \cdot \Omega_{\text{START}} \cdot \epsilon_{\text{START}}, \quad (2.17)$$

where  $\Omega_{\text{START}}$  is the solid angle of the annihilation photons subtended by the scintillator and  $\epsilon_{\text{START}}$  is the efficiency of detection of the photons in the fast plastic scintillator. This calculation is completed with the assumption that all positrons created within the sample will annihilate. The value of  $\epsilon_{\text{START}}$  is estimated to be 0.05, or 5% [30]. Given that the active region of the photomultiplier tubes used in this experiment is 4.6 cm in diameter and assuming the START PMT to be 0.1 cm away from the sample,  $\Omega_{\text{START}}$  is estimated to be 3.07 sr. This gives a rate of 511 keV gamma detection of  $7.05 \cdot 10^6$  counts/s.

Given that the START PMT has detected a 511 keV gamma, the probability of detecting, for example, a 1.78 MeV gamma, in the STOP PMT is

$$\text{Prob}_{\text{STOP}} = (\eta_\gamma - 1) \cdot \Omega_{\text{STOP}} \cdot \epsilon_{\text{STOP}}, \quad (2.18)$$

where  $\Omega_{\text{STOP}}$  is the solid angle of the silicon decay photon subtended by the STOP PMT scintillator,  $\epsilon_{\text{STOP}}$  is the efficiency of detection of the photons in the fast plastic scintillator, and  $\eta_\gamma$  is the decay gamma emission multiplicity. This calculation is also completed with the assumption that all positrons created within the sample will annihilate. The value of  $\epsilon_{\text{STOP}}$  is estimated to be 0.001, or 0.1% [30]. Assuming the STOP PMT is located a distance 10 cm from the aluminum target,  $\Omega_{\text{STOP}}$  is calculated to be 0.16 sr and the gamma multiplicity factor,  $\eta_\gamma$ , is 2, gives a detection probability of  $1.66 \cdot 10^{-4}$ .

Therefore, the overall rate of timing coincidence events is given by

$$\text{Rate}_{\text{Coinc}} = \text{Rate}_{\text{START}} \cdot \text{Prob}_{\text{STOP}}, \quad (2.19)$$

where  $\text{Rate}_{\text{START}}$  is given by Eq. 2.17 and  $\text{Prob}_{\text{STOP}}$  by Eq. 2.18. Continuing with our 12 cm long lead sample placed directly against the aluminum target, Eq. 2.19 is used to estimate the timing coincidence rate to be 1.13 kHz. Note that these calculations assume no energy discrimination is used on the START or STOP channels. A summary of the data and results of this calculation is presented in Table 2.1.

Since the energy discrimination selects only  $\sim 10\text{-}20\%$  of the events within each

PMT spectra, this 1.13 kHz timing coincidence rate will be further reduced by a factor significantly smaller than 0.02, the product of 10 and 20%. Also, the above calculations include no consideration of accidental background coincidences. To arrive at a more precise coincidence rate, the effect of discrimination and accidentals needs to be quantified using detailed Monte Carlo simulation studies. In conclusion, this calculation shows that the overall coincidence rate using this configuration will be quite small; thus the AG-PAS measurements will require an order of magnitude greater data collection time than the source-based measurements conducted in this study.

## 2.3 Photon Interactions with Matter

There are three major processes by which photons interact with matter, namely the photoelectric effect, Compton scattering, and pair production. Each of these processes plays a role within PALS, with the photoelectric effect also being critical to the physics of the signals produced and processed by the BaF<sub>2</sub> crystalline scintillator and photocathode of the photomultiplier detector.

The three processes take effect over a wide range of energies, as seen in Fig. 2.5. The greater the mass interaction coefficient for an interaction process, the greater the probability of occurrence of that process. The photoelectric effect is the dominant mode of interaction for low-energy photons and pair production is the dominant mode for high-energy photons. Compton scattering is seen with intermediary energy incident photons.

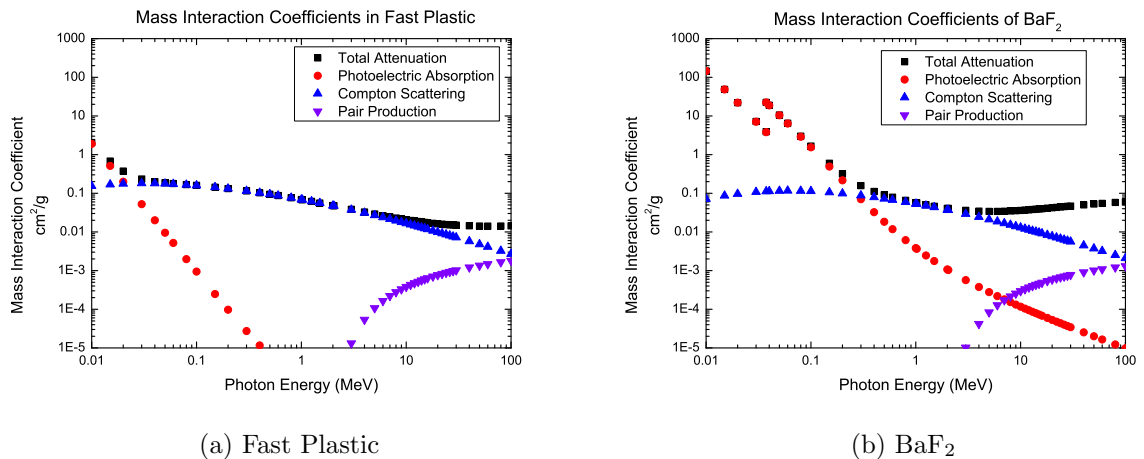


**Figure 2.5:** Mass interaction coefficients as a function of photon energy for (a) Polyvinyltoluene and (b) BaF<sub>2</sub> scintillators. These show the three major processes by which photons interact with matter [2].

The probability of a specific process occurring within a material depends upon the energy of the incident photon and the atomic composition of the material impinged upon by the incident photon. For example, in comparing the differences between the more dense BaF<sub>2</sub> scintillator and the less dense fast plastic scintillator, which uses Polyvinyltoluene as a base material [40], it is observed from Fig. 2.5a that the photoelectric effect is extremely weak at the expected energy regions of interest between 100 keV to 10 MeV in the fast plastic scintillator while having a much stronger probability of occurrence in the BaF<sub>2</sub> scintillator within the same energy

TABLE 2.1: Data used in coincident rate calculation.

Explanation	Symbol	Value	Units
Beam Current	$I_{\text{Beam}}$	200	$\mu\text{A}$
Incident Proton Flux	$\phi_p$	$1.25 \cdot 10^{15}$	protons/s
Target Thickness	$t_{\text{Al}}$	0.635	cm
Avogadro's number	$N_A$	$6.022 \cdot 10^{23}$	atoms / mol
Atoms in Target	$N_{\text{Al}}$	$3.83 \cdot 10^{22}$	atoms/cm <sup>2</sup>
$^{27}\text{Al}(p, \gamma)^{28}\text{Si}$ Cross-Section	$\sigma_{\text{capture}}$	6	$\mu\text{b}$
Si* Production Rate	Rate <sub>Si*</sub>	$2.87 \cdot 10^8$	atoms/s
Sample Effective Diameter	$\emptyset_{\text{sample}}$	1.27	cm
Sample Distance	$d_{\text{sample}}$	2	cm
Sample Solid Angle	$\Omega_{\text{sample}}$	0.294	sr
Gamma Production Rate	Rate <sub><math>\gamma</math> in sample</sub>	$8.44 \cdot 10^7$	atoms/s
Sample Thickness	$t_{\text{sample}}$	12	cm
Atoms in Sample	$N_{\text{sample}}$	$9.89 \cdot 10^{22}$	atoms/cm <sup>2</sup>
Fine Structure Constant	$\alpha$	$\sim 1/137$	
Classical Electron Radius	$r_0$	$2.82 \cdot 10^{-15}$	m
Incident Gamma Energy	$E_{\gamma}$	4000	keV
Electron Mass	$m_e$	$9.11 \cdot 10^{-31}$	kg
Speed of Light	c	$2.998 \cdot 10^8$	m/s
Pair-Production Cross-Section	$\sigma_{e^+e^-}$	5.50	barns
Positron Production Rate	Rate <sub>e<sup>+</sup></sub>	$4.60 \cdot 10^7$	positrons/s
PMT Active Diameter	$\emptyset_{\text{PMT}}$	4.6	cm
START Detector Distance	$d_{\text{START}}$	0.1	cm
START Detector Solid Angle	$\Omega_{\text{START}}$	3.07	sr
START Detector Efficiency	$\epsilon_{\text{START}}$	5	%
START 511 keV Detection Rate	Rate <sub>START</sub>	$7.05 \cdot 10^6$	counts/s
STOP Detector Distance	$d_{\text{STOP}}$	10	cm
STOP Detector Solid Angle	$\Omega_{\text{STOP}}$	0.16	sr
STOP Detector Efficiency	$\epsilon_{\text{STOP}}$	0.1	%
Gamma Decay Multiplicity	$\eta_{\gamma}$	2	
STOP Detection Probability	Prob <sub>STOP</sub>	$1.60 \cdot 10^{-4}$	
Timing Coincidence Rate	Rate <sub>Coinc</sub>	1.27	kHz

region, as seen in Fig. 2.5b. As a result, photopeaks, discussed in Sec. 2.6.2, are not present in the recorded energy spectra when using fast plastic scintillators.

### 2.3.1 Photoelectric Effect

The photoelectric effect shows that low-energy photons on the order of a few electronvolts (eV) to roughly 1 MeV can be absorbed by matter and re-emitted in the form of electrons under the right conditions. If the energy of the incident photon is greater than the work function of the material, then an electron of energy dependent upon the frequency of the incident photon is emitted by means of excitation and de-excitation of the atom. More specifically, the energy of the emitted electron, called the photoelectron, is given by:

$$E = h\nu + \phi \quad (2.20)$$

$$= h\nu + h\nu_0 \quad (2.21)$$

where  $E$  is the energy of the photoelectron,  $h$  is Planck's constant,  $\nu$  is the frequency of the incident photon,  $\phi$  is the work function of the material, and  $\nu_0$  is the threshold frequency of the material. It should be noted that only a single photoelectron is emitted per incident photon. Higher energy incident photons produce higher energy photoelectrons and a greater intensity of incident photons generate an equal intensity of photoelectrons.

The photoelectric effect is the underlying process responsible for the production of photopeaks in the gamma spectrum and the conversion of photons to electrons in the photocathode of the photomultiplier tube. These topics are further discussed in Sec. 2.6.2 and Sec. 3.2.2, respectively.

### 2.3.2 Compton Scattering

Compton electron scattering is a scattering process in which an incident photon interacts with an atomic electron, causing part of the energy of the incident photon to be transferred to the electron. The additional energy is absorbed and immediately emitted in the form of a recoil electron while the incident photon, having part of its energy lost due to the transference, is scattered at some angle away from its original path. Compton scattering is the dominant method of photon interaction with fast

plastic scintillators. The application of Compton scattering is discussed in detail in Sec. 3.3.7 and referenced in Fig. 2.5a.

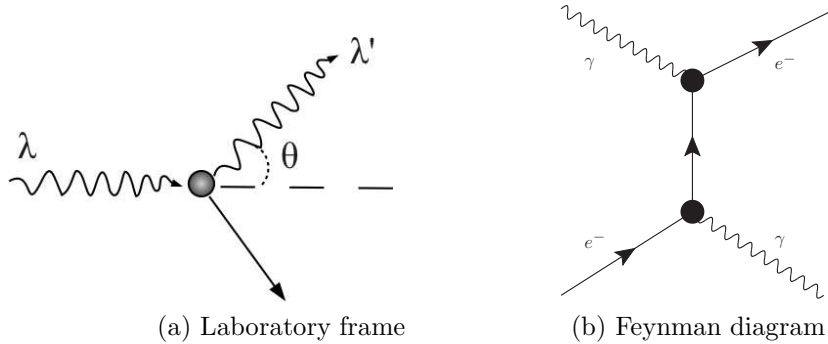


**Figure 2.6:** (a) Compton Scattering as seen from the laboratory frame. (b) The Feynman diagram depicts Compton Scattering as a quantum electrodynamical process

In Fig. 2.6a, it is shown how the incident photon scatters off of an electron, typically in the outermost valence electron shell, to produce an electron and a lower energy scattered photon. As seen in Fig. 2.5, Compton scattering is the dominant interaction process for intermediate energy ranges, as it typically is seen with incident photons between 100 keV and 10 MeV. Mathematically, purely elastic Compton scattering is described as

$$\lambda' - \lambda = \frac{h}{m_e c} (1 - \cos \theta) \quad (2.22)$$

where  $\lambda'$  is the wavelength of the scattered photon,  $\lambda$  is the wavelength of the incident photon,  $h$  is Planck's constant,  $m_e$  is the mass of the electron,  $c$  is the speed of light and  $\theta$  is the deflection angle of the scattered photon. Using the relation

$$E = \frac{hc}{\lambda}, \quad (2.23)$$

the equation is algebraically rearranged to give

$$E' = \frac{E}{1 + \frac{(1 - \cos \theta)E}{m_e c^2}} \quad (2.24)$$

where  $E$  is the energy of the incident photon and  $E'$  is the energy of the scattered photon.

### 2.3.3 Pair Production

Unlike the photoelectric effect and Compton scattering, the law of conservation of energy requires that in order for pair production to occur, an incoming photon must have an energy of at least 1.022 MeV. This is because in the presence of the Coulomb field of an atom, an incident photon of sufficient energy can produce a pair of particles, namely the electron and positron, each of mass 511 keV. The forward momentum and angle of separation between these two created particles depends upon the conservation of energy and momentum stemming from the energy and momentum of the incident photon.

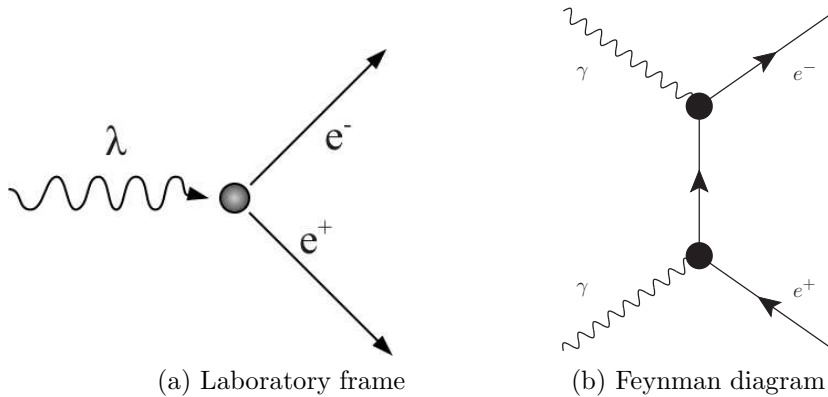


**Figure 2.7:** (a) Pair production as seen in the laboratory frame. (b) From the Feynman diagram, pair production is another example of a quantum electrodynamical interaction.

A fundamental theorem of particle physics, the CPT theorem, accurately predicts the physical properties of the positron and its relation to the electron. CPT stands for Charge conjugation, Parity, and Time reversal. Under this symmetry, physical laws are symmetric under transformations involving the simultaneous inversion of the properties of charge, parity and time with no currently known contradictions. This is referred to as the CPT theorem and has been used to demonstrate that the positron is the anti-particle of the electron, meaning that the two particles are symmetric in terms of particle mass, spin, and gyromagnetic ratio, but have the opposite charge [6, 13].

Pair production can and does occur in which the heavier cousins of the electron, the muon or tau and their respective anti-particles, are created, but these processes require energies much greater than the energies typically encountered in a positron

annihilation spectroscopy experiment.

## 2.4 Positron Interactions with Matter

Once a gamma of sufficient energy has interacted with the metallic atomic lattice and produced an electron - positron pair through pair production, a series of events occurs as part of the process of positron annihilation. Specifically, these processes are thermalization, diffusion, and annihilation. The period of time for this series of interactions to occur is quite short, on the order of  $10^{-10}$  s [29, 37]. The majority of positron penetration into a solid occurs during the stage of positron thermalization, with a minor contribution from the process of diffusion.

### 2.4.1 Thermalization

The positron first goes through a process of thermalization within the lattice in which the positron kinetic energy decreases to the level of thermal equilibrium by means of elastic and inelastic collisions with electrons. The exact process by which this occurs depends upon the initial kinetic energy of the positron. For positrons having kinetic energies less than 20 MeV, the initial energy loss is by means of ionization in which the kinetic energy of the positron is transferred to lattice electrons as it moves through the lattice. Once the kinetic energy of the positron has been reduced to energies on the order of 5 eV, plasmon excitation becomes prevalent and finally positron-phonon excitation and electron-hole pair creation below energies of 0.1 eV. This process of thermalization occurs on the order of  $10^{-12}$  s, which is quite short in comparison to the total lifetime of the positron [29, 37].

Prior to reaching thermal equilibrium with a material, the penetration of positrons emitted by a radionuclide into a solid can be described by an empirical law developed originally for electrons, but proven also valid for positrons. The positron intensity as a function of the distance traveled within the material is given empirically by

$$P_+ = e^{-\alpha_+ x}, \quad (2.25)$$

where  $x$  is the distance traveled within the material and  $\alpha_+$  is the positron absorption coefficient given by

$$\alpha_+ = \frac{C_+\rho}{(E_{max})^{\beta_+}} \text{ cm}^{-1}, \quad (2.26)$$

where  $\rho$  is the sample-mass density in  $g/cm^3$ ,  $E_{max}$  is the maximum positron energy in MeV,  $C_+$  and  $\beta+$  are empirically derived values of  $17.0\ cm^2/g$  and  $1.43$ , respectively [4, 37].

Using positron energies on the order of 100 keV, as is seen with positrons emitted by a radioactive source such as  $^{22}\text{Na}$ , the positron penetration depth is found to be on the order of only  $100\ \mu\text{m}$ , as seen in Fig. 2.8 [29]. As a result, source-based studies of PALS are only effective in revealing surface defects of materials. Techniques which employ higher energy positrons or create positrons directly within a material are necessary for deeper defect analysis.

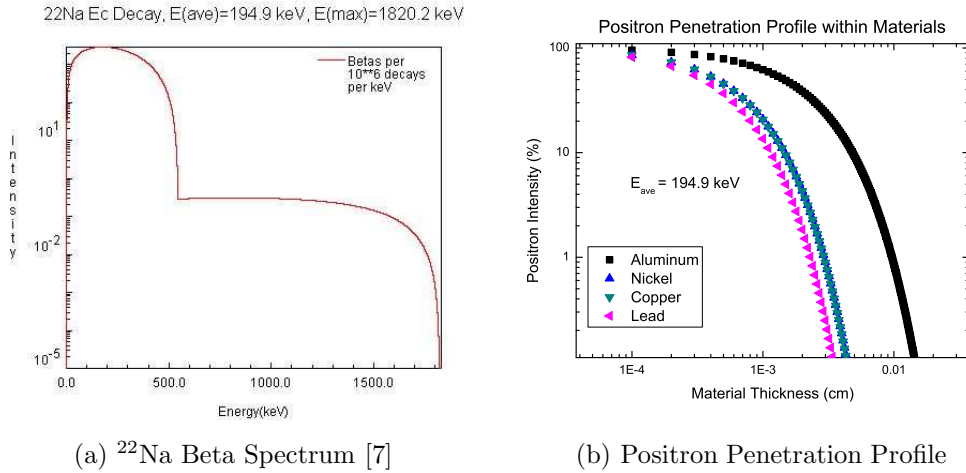


**Figure 2.8:** (a) The energy spectrum of positrons emitted from a  $^{22}\text{Na}$  as a function of intensity. Positrons are emitted with an average energy of 194.9 keV, which upon thermalization in a material is reduced to an energy of less than 0.1 eV. (b) These positrons typically only travel about 0.1 mm into a sample.

## 2.4.2 Diffusion

Upon reaching thermal equilibrium with the atomic lattice, the positron begins a process known as diffusion in which the positron undergoes three dimensional random walk through the lattice. As the positron is positively charged, it is repelled by nuclei within the lattice and moves towards areas with concentrations of defect densities, which are seen as having a more negative, or attractive, potential. The next section describes the process of positron trapping in which the positron resides for a period of time within the defect lattice vacancies. These processes of diffusion and trapping are the two greatest contributors to the positron lifetime.

The mean free path between two scattering events is given by

$$\langle l \rangle = \frac{3D_+}{v_{RMS}} \quad \text{with} \quad v_{RMS} = \sqrt{\frac{3kT}{m}}, \quad (2.27)$$

where  $\langle l \rangle$  is the average distance the positron travels between successive scattering events,  $D_+$  is the diffusion coefficient,  $v_{RMS}$  is the root mean square of the positron thermal velocity,  $k$  is the Boltzmann constant,  $T$  is the temperature of the system, and  $m$  is the positron mass. Applying the semiclassical random-walk theory, the diffusion coefficient is given by

$$D_+ = \frac{1}{3}v_{RMS} l = \frac{1}{3}v_{RMS}^2 \tau, \quad (2.28)$$

where  $\tau$  is the relaxation time. This approximation is valid so long as the thickness of the sample length is longer than the mean free path for scattering. Typically, the positron mean free path in metals at room temperature is on the order of  $10^2$  Å while the total diffusion length before annihilation is on the order of  $10^3$  Å [37]. As a result, the positron is able to search for the more attractive potential of a defect density region over a large number of atomic sites within the atomic lattice of the material, making PAS very effective at assessing defect densities within materials.

In general, the relationship between the annihilation rate,  $\lambda$ , and the positron lifetime,  $\tau$ , is given by

$$\lambda(\vec{r}) = 1/\tau(\vec{r}). \quad (2.29)$$

This equation is later modified in Sec. 2.4.3 to differentiate between positron lifetimes in annealed and damaged materials.

In all, the diffusion process is described by the diffusion-annihilation equation

$$\frac{\partial f(\vec{r}, t)}{\partial t} = D_+ \nabla^2 f(\vec{r}, t) - \lambda_{\text{eff}}(\vec{r}) f(\vec{r}, t) - \nabla \cdot [\mathbf{v}_d(\vec{r}) f(\vec{r}, t)] + f_i(\vec{r}, t), \quad (2.30)$$

where  $f(\vec{r}, t)$  is the positron density at position  $\vec{r}$  and time  $t$ ,  $f_i(\vec{r}, t)$  is the source term,  $D_+$  is the diffusion coefficient and  $\mathbf{v}_d$  is the positron drift velocity due to external fields. The source term is defined as the number of positrons entering the system per unit time [37]. The notation  $\lambda_{\text{eff}}$  is used to describe the summation of the annihilation rates in the bulk material and the trapping rate, discussed in Sec. 2.4.3.

### 2.4.3 Trapping

After the thermal motion of the positron has reached equilibrium and it has diffused within the atomic lattice of the metal, the positron having a positive charge undergoes Coulomb repulsion from the positive ions within the metal. Any regions with defects within the lattice, be they lattice vacancies, dislocation cores or any other types of voids or holes, will have an absence of positive ions in comparison to the atomic lattice and thus be electrically attractive to a positron while repulsive to an electron. The greater the defect density concentration, the longer the positron is capable of residing within the defect region [16, 19, 37, 43]. This process of the positron moving towards and residing within a region of less positive potential within the atomic lattice is known as positron trapping.

A variety of positron trapping models exist in order to accommodate the various types of defects which can occur in a material. Excluding impurities in materials, the most common types of material defects are monovacancies and dislocations, in which either an atom is completely removed from an atomic lattice site within the material or the atom has shifted position within the lattice. Each of these can be described using a two or three state trapping model [19, 37]. Treating the three state trapping model as a general form, the positron trapping and annihilation processes are described by the kinematic differential equations

$$\begin{aligned}\frac{dc_b}{dt} &= -c_b\lambda_f - c_b\kappa_1(\vec{r}) - c_b\kappa_2(\vec{r}) + \left[ \frac{\partial f(\vec{r}, t)}{\partial t} \right]_{\text{source}} \\ \frac{dc_1}{dt} &= -c_1\lambda_1 + c_b\kappa_1(\vec{r}) \\ \frac{dc_2}{dt} &= -c_2\lambda_2 + c_b\kappa_2(\vec{r})\end{aligned}\quad (2.31)$$

where  $\kappa_1(\vec{r})$  and  $\kappa_2(\vec{r})$  represent the trapping rates within each type of defect;  $\lambda_f$  represents the positron annihilation rates in the bulk or defect free regions;  $\lambda_1$  and  $\lambda_2$  represent the positron annihilation rates within each type of defect regions; and  $c_b$ ,  $c_1$ , and  $c_2$  represent the probabilities at time  $t$  of finding the positron in the bulk material, the first type of defect, and the second type of defect, respectively. The term  $\partial f(\vec{r}, t)/\partial t$  again represents the source term, which is the number of positrons entering the system per unit time [19, 37].

When using only a two state trapping model, Eq. 2.31 reduces by means of

$\kappa_2(\vec{r}) = 0$ , resulting in

$$\begin{aligned}\frac{dc_b}{dt} &= -c_b\lambda_b - c_b\kappa_D(\vec{r}) + \left[ \frac{\partial f(\vec{r}, t)}{\partial t} \right]_{\text{source}} \\ \frac{dc_D}{dt} &= -c_D\lambda_D + c_b\kappa_D(\vec{r}),\end{aligned}\quad (2.32)$$

where  $\kappa_D(\vec{r})$  represents the trapping rate within the defect regions and  $c_D$  represents the probability at time  $t$  of finding the positron in the defect region [19, 37].

For materials with defects, the effective positron annihilation rate,  $\lambda_{\text{eff}}$ , is given by

$$\lambda_{\text{eff}}(\vec{r}) = 1/\tau_{\text{eff}}(\vec{r}) = \lambda_b + \kappa(\vec{r}), \quad (2.33)$$

where  $\tau_{\text{eff}}(\vec{r})$  is the effective positron lifetime,  $\lambda_b$  is the positron annihilation rate in the bulk material and  $\kappa(\vec{r})$  is the trapping rate of the sample. This trapping rate depends on the type of defects in the material and is proportional to the defect concentration, which can vary throughout the material under study. In annealed materials with no defects,  $\kappa(\vec{r}) = 0$  and thus

$$\lambda_{\text{eff}}(\vec{r}) = \lambda_b = 1/\tau_{\text{eff}}(\vec{r}). \quad (2.34)$$

The effect of accounting for defects in the overall lifetime spectrum is discussed in Sec. 2.5.1.

#### 2.4.4 Positron Annihilation

A positron is created through either a  $\beta^+$  nuclear decay event or through pair production. In the event of creation through pair-production, the positron may have significant forward momentum remaining as a result of the process of its creation. This is unlike positrons created through nuclear decay, which typically have little momentum, as is the case for  $^{22}\text{Na}$ . After undergoing the processes of thermalization, diffusion, and trapping, the positron is in a state of very low kinetic energy and in close proximity to its anti-particle, the electron. Positron annihilation is a quantum electrodynamic process in which a positron and electron annihilate, that is, convert their mass entirely into energy.

At a minimum, if the positron and electron are at rest just before annihilation, the resultant photons each have energies of 511 keV through conservation of energy

and are emitted at  $180^\circ$  with respect to each other. In the more likely event, that for example, due to orbital angular momentum around a nucleus, the electron possesses some momentum beyond its rest mass, the resultant annihilation produces photons of energies slightly less than and greater than 511 keV [12]. The final emitted photon energies depend upon whether the atomic electron is moving towards or away from the direction of motion of the positron. This process is known as Doppler broadening and is a minor contribution to the statistical smearing of peaks discussed in Sec. 2.6.

In addition to *direct* annihilation in which the positron annihilates with a valence electron of an atom within the atomic lattice of a material, positron annihilation can occur when a positron interacts with a free electron, forming a bound atomic state known as positronium (Ps). This state can occur in both the ground and excited states, resulting in a singlet state, known as para-positronium (p-Ps), and a triplet state, known as ortho-positronium (o-Ps). As expected, the positronium state is short-lived. The para-positronium state has a characteristic lifetime in vacuum of 124 ps while the ortho-positronium state has a characteristic lifetime in vacuum of 142 ns [6]. The 124 ps lifetime of p-Ps is a characteristic lifetime from the time of the formation of p-Ps to its eventual self-annihilation, releasing two gammas with typical energies of 511 keV. In the case of o-Ps, three gammas of energies less than 511 keV are released. The two gamma decay process of o-Ps is forbidden by electromagnetic angular momentum selection rules, requiring interaction with an external electron to proceed [6, 13, 36]. The effect of these two states of positronium on the overall lifetime spectrum is further discussed in Sec. 4.3.

There are four major channels by which positron annihilation occurs, as given in Fig. 2.9. Although it is more probable for the positron annihilation to produce gammas, with the two-gamma process depicted in Fig. 2.9c being the most probable, it is possible for positron annihilation to occur without gamma emission. In the radiationless and single gamma annihilation channels, the positron annihilates with an inner shell electron, resulting in energy being transferred to another bound electron which is then emitted with a kinetic energy of  $E + mc^2 - 2E_b$  in the case of radiationless annihilation or  $E + mc^2 - E_b$  in the case of single gamma emission. Here,  $E$  is the total energy of the positron given by Eq. 1.1 and  $E_b$  is the binding energy of each of the two electrons involved [6].

Higher order processes which produce additional gammas exist, but are heavily

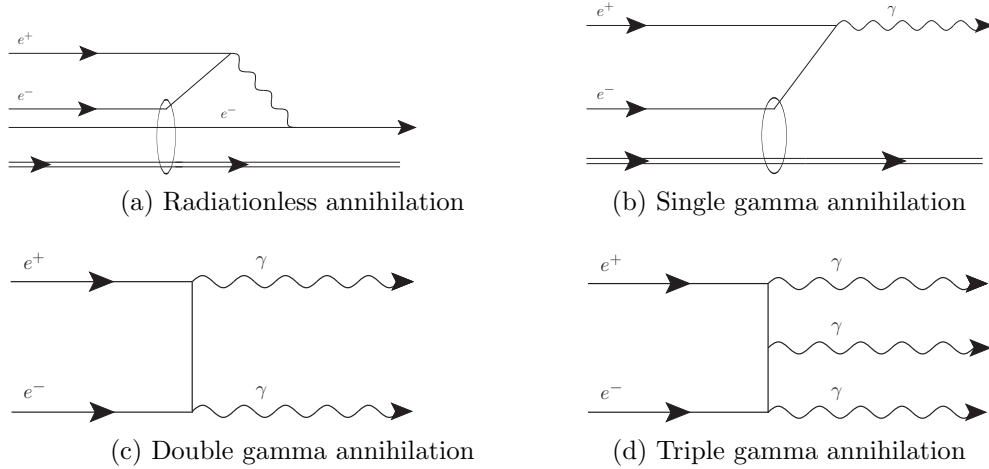


**Figure 2.9:** Feynmen diagrams of positron annihilation

suppressed due to extremely low branching ratios on the order of  $10^{-6}$  when comparing four-gamma modes with two-gamma modes [6].

The positron cross-section, or probability of interaction, for the two-gamma emission was first derived by Paul Dirac in 1930 [6, 13]. In its relativistic form, it is given by:

$$\sigma_{2\gamma} = \frac{4\pi r_0^2}{\gamma+1} \left[ \frac{\gamma^2 + 4\gamma + 1}{\gamma^2 - 1} \ln \left( \gamma + \sqrt{\gamma^2 - 1} \right) + \sqrt{\gamma^2 - 1} - \frac{\gamma + 3}{\sqrt{\gamma^2 - 1}} \right] \quad (2.35)$$

where  $r_0 = e^2/(4\pi\epsilon_0 m_e c^2)$  is the classical radius of the electron,  $\gamma = 1/\sqrt{1-\beta^2}$ ,  $\beta = v/c$  and  $v$  is the speed of the positron relative to the stationary electron. For low energies, specifically those used in positron annihilation spectroscopy studies, positrons annihilate at nonrelativistic velocities following thermalization and diffusion. Taking this into account,  $v \ll c$  and thus Eq. 2.35 reduces to

$$\sigma_{2\gamma} = 4\pi r_0^2 c/v. \quad (2.36)$$

## 2.5 Fundamentals of PALS

In a damaged sample, atoms within the sample are displaced from their original lattice positions, with greater displacement resulting in regions of higher defect density. These regions are seen as having a less positive potential relative to that of the

potential created by surrounding nuclei. As the positron thermalizes and diffuses through the sample, it is electrically attracted to the region of less positive potential. Even after thermalization, however, the positron retains some momentum and thus observes random motion within this region of more negative potential. With larger displacement between atoms, indicative of a greater defect density, the positron has a longer period of survival within the sample. Eventually, the positron annihilates with the electron shell of neighboring atoms, typically producing two coincident gammas. The energy of these two gammas is determined by the rest mass and momentum of both the incident positron and the atomic electron with which it annihilates. The resultant gammas have an average energy of approximately 511 keV [6, 44].

### 2.5.1 Positron Lifetimes in Materials

Once the detector resolution and lifetime spectra have been obtained using the procedures outlined in Secs. 3.3, 3.4, 3.5, and 3.6, the positron lifetimes are extracted from not just the material under study, but from any other contributions to the spectrum. These contributions may include the Kapton tape in which the radionuclide source is enclosed and the background, which consists of the air between the sample material and the scintillator, the tape and foil used to block external light from the photomultiplier tube, and any contributions from the non-local experimental environment. As is discussed in Sec. 4.3.1, the Kapton tape itself has two lifetime components, but only a single component may be detected. In order to extract these lifetime values, the detector and associated equipment should first be characterized and optimized to achieve the optimal timing resolution of the system.

The timing resolution of system is characterized using the procedure described in Sec. 3.5. The spectrometer produces a Gaussian distribution which describes the timing difference between the emission of the 1173 keV and 1332 keV gammas from a  $^{60}\text{Co}$  radionuclide source. Since the time difference between emission of these two gammas is on the order of picoseconds,  $^{60}\text{Co}$  provides a good reference to determine the minimum timing resolution of the system. This timing resolution, or prompt resolution, is generally given by a summation of Gaussian distributions, mathematically described as

$$R(t) = \sum_{i=1}^n \frac{1}{\sqrt{2\pi\sigma_i^2}} \exp\left[-\frac{(t - t_{0i})^2}{2\sigma_i^2}\right], \quad (2.37)$$

where  $\sigma_i$  is the standard deviation of the  $i^{th}$  Gaussian function and  $t_{0i}$  is the center

position of the  $i^{th}$  Gaussian function. In this study, as it is explained in Sec. 4.2, only a single Gaussian distribution is used to describe the prompt resolution of the spectrometer. From this prompt resolution function, a quantity known as the Full Width at Half-Maximum (FWHM) is obtained. It is given as

$$\text{FWHM} = 2\sqrt{2 \ln 2} \sigma. \quad (2.38)$$

The resolution of the spectrometer is given in terms of the FWHM. The better the resolution, the more capable the spectrometer is of discerning minute differences in positron lifetimes over varying degrees of damage in materials and different material contributions. Experimentally, the resolution of the system depends upon several factors: choice in scintillator material and geometry, the characteristics of the photomultiplier tubes, the NIMs used in the spectrometer, and the settings of the electronic modules. Typical modern PALS spectrometers have a resolution of 120 - 250 ps [1, 17, 34, 41]. The results of the timing resolution of the spectrometer constructed for this study are given in Sec. 4.2.

Once the prompt resolution function of the spectrometer is determined, deconvolution theorems are applied to extract the individual positron lifetime components from the overall obtained spectrum. Each positron lifetime function can be characterized by means of an exponential decay function. Thus for multiple lifetime components, the overall function may be described as the convolution of the prompt resolution function with the sum of the positron lifetime components. Mathematically, this is given by

$$C(t) = \int_0^{\infty} R(t - t_0) S(t_0) dt_0, \quad (2.39)$$

where  $R(t - t_0)$  is the resolution function given by Eq. 2.37 and  $S(t_0)$  is the series of exponential decay functions given by

$$S(t_0) = \sum_i \frac{I_i}{\tau_i} \exp \left[ -\frac{t}{\tau_i} \right] \quad (2.40)$$

where  $I_i$  is the intensity of the  $i^{th}$  exponential within the spectrum and  $\tau_i$  is the positron lifetime in the  $i^{th}$  component of the spectrum [19]. Within solids, positron lifetimes are typically on the order of 100 - 500 ps [6]. Each of these exponential functions must be extracted from the spectrum and analyzed in order to determine the effective positron lifetime within the material of interest. The lifetimes for the

materials in this study are analyzed using the methods described in Sec. 4.1 with the results reported in Sec. 4.3.

The positron lifetime function is modified when using the models discussed in Sec. 2.4.3 for defects with monovacancies and multiple vacancies within a region of the material. These models use a series of differential equations to describe the trapping of positrons and subsequent annihilation with atomic shell electrons of the bulk material, discussed in Sec. 2.4.3 [19]. In the case of the two and three state trapping models, the function  $S(t_0)$  is modified such that

$$S(t_0) = c_b \lambda_b + \sum_{i=1}^n c_i \lambda_i, \quad (2.41)$$

where  $\lambda_b$  and  $\lambda_i$  are the positron annihilation rates in the bulk and  $i^{th}$  defect regions of the material. The values  $c_b$  and  $c_i$  are given by

$$c_b = \exp(-\lambda_b t) \quad (2.42)$$

and

$$c_i = \frac{\kappa_i}{\lambda_b - \lambda_i} [\exp(-\lambda_i t) - \exp(-\lambda_b t)], \quad (2.43)$$

which represent the probability of finding the positron in the bulk material or in the  $i^{th}$  type of defect. As discussed in Sec. 2.4.3, the trapping rate is proportional to the intensity or amount of defects within the sample as illustrated in Eq. 2.41. The greater the trapping rate, the more defects present within the material.

## 2.6 Gamma Spectroscopy

Each and every radionuclide possesses its own unique signature by which it is identified. This signature, whose method of detection is dependent upon on the decay processes involved (see Sec. 2.1 and 3.2.1), contains information which can be of use to the experimenter [21]. In the case of gamma spectroscopy, several key elements are found to be useful, depending on the experimental setup and goals.

Within the gamma spectrum of a radionuclide, using Fig. 2.10 as an example, several useful features can be observed. From the left, the Compton continuum is seen as the slightly concave-shaped spectral range produced by Compton scattering. Depending on experimental setup, the double and single escape peaks may or may not

be visible, but with fast plastic,  $\text{BaF}_2$  and  $\text{NaI}(\text{Tl})$  scintillators with photomultiplier tubes, as well as with HPGe detectors, the Compton edge should always be visible [21]. Finally, each gamma energy emitted by a radionuclide has a characteristic photopeak which can be detected using a  $\text{BaF}_2$  crystalline scintillator in conjunction with a photomultiplier tube or with a  $\text{NaI}(\text{Tl})$  detector. Sections 3.3.7 and 3.5 discuss the usefulness of these photopeaks and the Compton continuum as energy calibration points and in determining the energy resolution of the photomultiplier tubes.

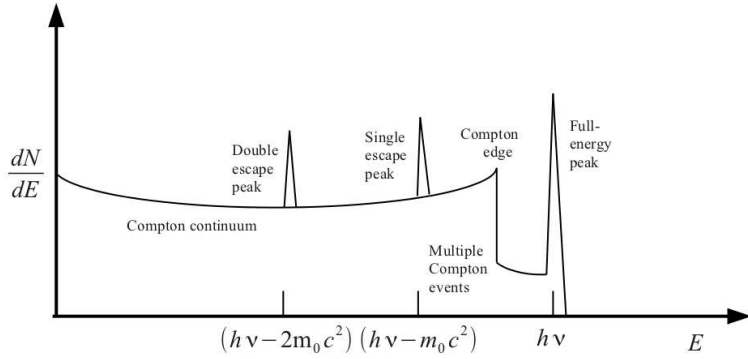


**Figure 2.10:** Theoretical spectrum produced in gamma spectroscopy experiments. As products of pair-production within the scintillator, the creation of the single and double escape peaks requires incident photons of energies greater than 1.022 MeV. More specifically for  $\text{BaF}_2$  and fast plastic scintillators, the incident photon energies must be greater than approximately 2.5 MeV, as seen in Fig. 2.5. Otherwise, only the Compton continuum and Compton edge will be visible, with the full-energy photopeak additionally visible with  $\text{BaF}_2$  scintillators.

### 2.6.1 Compton Spectrum

The Compton continuum is a gamma spectroscopy feature which is produced as a result of Compton scattering, detailed in Sec. 2.3.2. The Compton continuum depicts the energies of the scattered photon along the entire range of possible scattering angles, from  $\theta = 0$  to  $\theta = \pi$ , using Eq. 2.24. The energy at which the scattered photon deflects at the greatest angle of  $\theta = \pi$  is referred to as the Compton edge. This feature marks the energy where the maximum energy transfer from the scattered photon to an electron occurs. As is later described in Sec. 3.3.7, the Compton edge is an important feature in PALS as it allows for energy calibration to be completed when using a plastic scintillator.

Beyond the Compton edge, the rate of detected signals drops until reaching the

photopeaks, if existent. Due to the possibility of multiple Compton scattering events in the scintillator with the final scattered photon escaping from the scintillator, there is a degree of signal smearing which results in the energy appearing to not decrease entirely to zero in higher energy channels of the data acquisition system [21].

Two other features which may be present within the region of the Compton continuum are the single and double escape peaks. Although not useful for the purposes of PALS, they are important to note as they may be confused as being artificial peaks within the pulse height spectrum as a result of experimental misstep. The single escape peak is a feature produced by a multiple step process within the scintillator. When a high enough energy gamma creates an electron-positron pair within the scintillator, the positron eventually annihilates. The single escape peak is the result of one of these annihilation photons escaping from the scintillator while the other is photoelectrically absorbed and processed by the detector. The net result of this effect is a lower energy peak located at a distance  $m_e c^2$  from the photopeak. A second peak, called the double escape peak, is located at  $2m_e c^2$  from the photopeak and is the result of the detection of only the kinetic energies of both the electron and positron created through pair-production within the scintillator [21].

### 2.6.2 Full Energy Peaks

Each gamma emitted by a radionuclide produces an energy-proportionate full-energy peak, or photopeak, in the pulse height spectrum. A photopeak is the spectroscopic signal, located at  $E = h\nu$ , created by the full energy deposition of a photon into the scintillator. When an incident photon is absorbed by an atom in the scintillator, a photoelectron is emitted from one of the electron shells of the absorber atom. From Eq. 2.20, it is seen that the emitted photoelectron has a kinetic energy equal to the difference of the binding energy of the electron in its original electron shell from the incident photon energy [21]. Since the binding energy is usually small in comparison to the incident photon energy, the photopeak gives a good measurement of the energy of the original incident gamma ray and is used as a calibration point when using NaI(Tl) and BaF<sub>2</sub> scintillators in Sec. 3.4 and 3.5.

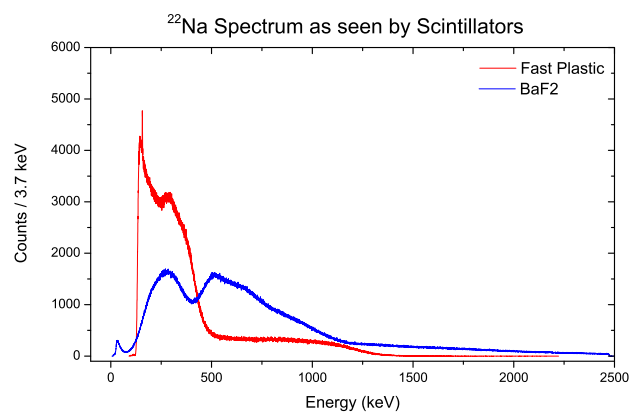


**Figure 2.11:** A comparison of the  $^{22}\text{Na}$  energy spectrum as seen by the fast plastic and  $\text{BaF}_2$  scintillators.

---

CHAPTER  
**THREE**

---

MATERIALS AND METHODS

### 3.1 Positron Sources

#### 3.1.1 $^{22}\text{Na}$ Source Positrons

Before the spectrometer can be used in a feasibility study using a continuous wave accelerator, the positron lifetimes in the high-purity samples must be experimentally determined to be in good agreement with currently accepted literature values. Traditionally, radionuclide sources used in gamma spectroscopy consist of a radionuclide source encased in a thick acrylic disk and sealed with an epoxy. As shown in Sec. 2.4.1, positrons emitted from  $^{22}\text{Na}$  typically only travel an order of 0.1 mm before annihilation. This necessitates the use of a  $^{22}\text{Na}$  solution situated between two thin films of Kapton tape to maintain structure. Even so, a non-negligible number of the positrons decay within the thin film of Kapton, contributing to the overall spectrum, discussed in Sec. 4.3.

In order to perform measurements of the positron lifetime in a material, the radionuclide source is sandwiched between two samples of the same material and thickness, as demonstrated in Fig. 3.1b. This is necessary due to the large drop in positron intensity after the positron travels less than a millimeter as a result of the exponential rate dependence.

In order to obtain a positron lifetime within a material, a positron birth and death signal must be detected, with the time difference between these two events giving the positron lifetime. Referring to Fig. 2.1a, the positron is first emitted by the  $^{22}\text{Na}$

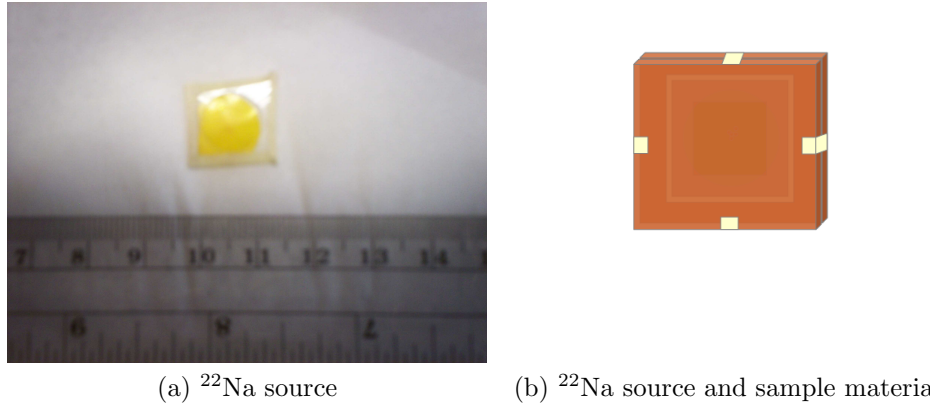


**Figure 3.1:** (a) The  $^{22}\text{Na}$  source and surrounding Kapton tape. (b) The  $^{22}\text{Na}$  source is sandwiched between the sample materials when completing source-based studies

radionuclide, followed by the 1274 keV gamma. However, as the positrons annihilate in air, the positrons themselves do not make it to the detector. Furthermore, the positrons take on the order of at least 500 ps to annihilate with an electron in the air to produce two coincident 511 keV gammas. Thus the 1274 keV gamma emitted from the  $^{22}\text{Na}$  radionuclide appears to reach the detector first and is used as the positron birth signal while the annihilation photons are used as the positron death signal. By taking the time difference between the detection of these two events, the positron lifetime in a material can be determined. In subsequent sections throughout this paper, the positron birth event is referred to as the TAC START and the positron death event is referred to as the TAC STOP.

### 3.1.2 Accelerator-Induced Positrons

Unlike source-based studies in which positrons are emitted from the nucleus of a radionuclide suspended on a thin film, positrons created using an accelerator are created within the sample itself by means of pair-production. Thus unlike the lifetime spectrum recorded when using source-based positrons, the accelerator-induced positron annihilation lifetime spectrum only needs to account for the lifetimes of the material under study and the background. This gives a cleaner signal as contributions from the positronium annihilation and the Kapton thin film are not present in

the resultant lifetime spectrum.

Using the reaction given by Eq. 2.4 to describe the gamma decay branch of the excited silicon, there are several resultant gammas that are above the  $2m_e c^2$  pair-production threshold and thus serve as positron sources. With proper discrimination settings as given in Sec. 3.6, the 511 keV annihilation gamma is used as the TAC START signal and any gamma of energy above the minimum signal amplitude discrimination of the 584 Constant Fraction Discriminator can serve as the TAC STOP signal. The roles of the TAC START and TAC STOP are reversed from the configuration used for source-based studies due to data acquisition deadtime considerations, as discussed in Sec. 3.6.2. Using a high-purity Germanium (HPGe) detector, photon energies produced by the  $^{27}\text{Al}(p, \gamma)^{28}\text{Si}$  reaction are more clearly discerned due to the much higher energy resolution of the HPGe detector. These energies are seen in Fig. 2.3.

In addition to the photon energies, the relative rates of the resultant photons are observed in Fig. 2.3. From this it is seen that the 1.78 MeV gamma is emitted more frequently than the other gammas and thus is useful as a guaranteed STOP signal for every annihilation event within the sample under study.

Experimentally, the material under study is placed directly in the path of the beam. The photomultiplier tube designated to collect the TAC START signal is placed as close as possible to the material while the second photomultiplier tube designated to collect the TAC STOP signal is positioned towards the aluminum beam target. The second photomultiplier tube is positioned a distance away from the target as to have a data collection rate equal to at least that of the photomultiplier tube collecting the TAC START signal from the 511 keV gammas created within the material. This is done so that for every 511 keV TAC START signal generated, there is a guaranteed TAC STOP signal in order to reduce deadtime of the system.

In addition, alternate experimental configurations which employ heavy shielding need to be carefully studied. Shielding thicknesses and geometries must be especially taken under consideration as high-energy gammas are emitted isotropically from the accelerator target, resulting in these high-energy gammas pair-producing within the shielding. This causes the shielding itself to become a bright source of 511 keV photons, interfering with the signal coming from the sample material under study.

## 3.2 Detection Equipment

### 3.2.1 Scintillators

A scintillator is a material which emits visible radiation following its excitation within the structure of the material by some means, typically through either the partial or total deposition of the kinetic energy of radiation or a particle within the material. This process is known as fluorescence. The exact mechanism of fluorescence depends on whether or not the scintillator is organic in nature.

Four of the major properties of scintillators are their emission wavelength, their scintillation efficiency, their decay time, and their light yield. Although scintillators fluoresce over a range of wavelengths, there is always a wavelength in which the emission is the most intense. This wavelength is known as the emission wavelength. The scintillator efficiency is the amount of energy incident upon the scintillator which is emitted as visible light. The decay time of the scintillator is the time necessary for the prompt fluorescence intensity to drop below  $1/e$  of its maximum. Finally, the light yield, or light output, is the percentage of light emitted in terms of anthracene, a fragile organic crystal possessing the highest scintillation efficiency of any known organic scintillator [21].

Scintillators are divided into two major categories, namely organic and inorganic scintillators. Organic scintillators typically have a hydrocarbon composition and can be found in both liquid and solid forms. Due to the low-Z value of the material composition, organic scintillators are most favored for beta spectroscopy and fast neutron detection. However, certain variations known as plastic scintillators are used extensively in gamma spectroscopy due to their low cost, ease of manufacturing, pliability of material and fast response times. Unfortunately, this lower Z value results in a lower density of the material, which results in the loss of the ability for incident photons to interact with organic scintillators by means of the photoelectric effect (see Sec. 2.3 and Sec. 2.6.2). This effect is observed in Fig. 2.5a, which shows the interaction of the photoelectric effect to be negligible above incident photon energies of 100 keV.

Inorganic scintillators are preferred for use in gamma spectroscopy due to their higher density and high Z-value, resulting in the observation of photopeaks in the energy spectrum as a result of a greater interaction profile of the photoelectric interaction (see Fig. 2.5b). As will be discussed in Sec. 3.3.7, this process is simpler and

a more accurate method of performing energy calibrations. Common examples of inorganic scintillators include NaI(Tl), Bismuth Germanate (BGO), CsI, and BaF<sub>2</sub>.

Gas scintillators, typically high-purity noble gases, are also used in spectroscopy applications. These scintillators are extremely fast in comparison to liquid and solid organic and inorganic scintillators, but as a trade-off, have very low light output, often on the order of a full order of magnitude lower than that of NaI(Tl) scintillators. Gas scintillators are used extensively in heavy-ion detection [21].

When either a gamma or a particle is incident on an organic scintillator, the energy absorption in the scintillator results in a transition in the energy level structure of individual molecules in the scintillator. Within a few picoseconds, the de-excitation of electrons in the energy level structures releases photons in order to return to the ground states in a process known as fluorescence [21]. In the usual scintillator-PMT detector setup, the scintillated photons have energies of only a few electronvolts.

The two plastic scintillators chosen for the PALS experiment are both BC-418, manufactured by Saint-Gobain. Materially speaking, BC-418 scintillators offer a short rise time of 0.5 ns, a fast decay time of 1.4 ns and have a maximum emission wavelength of 391 nm [40]. Thus the light emitted is in the near ultraviolet to visible region of the electromagnetic spectrum and must be properly interfaced with a photomultiplier sensitive to this wavelength in order for the signal received to be converted into an electrical pulse.

The plastic scintillator used in this study is a truncated cone of dimensions 1.25" large diameter x 0.95" small diameter x 1" thick. This truncated cone shape was designed in the 1970s and offers an improvement of 10-15% in the overall timing FWHM using a <sup>60</sup>Co source when compared with a cylindrical scintillator of similar volume and the same composition [28, 32].

Unlike organic scintillators, which rely on excitation within the molecular structure of the organic material, a gamma or particle incident upon an inorganic scintillator results in the excitation of energy states within the crystalline lattice structure of the inorganic material. From solid state physics, it is known that the excitation of a ground state electron can result in the electron transiting from the valence band to the conduction band. This forms a hole in the valence band and after a period of time, an electron loses its energy and returns to the valence band while emitting a photon to remove the excess energy between energy levels from the system. In order for the energy of the emitted photon to be within the visible spectrum, impurities

known as activators must be added into the crystalline material to allow for energy states to be created within the band gap between the valence and conduction bands, known as the forbidden band [21].

The BaF<sub>2</sub> crystalline scintillator used in this study offers two major emission bands. The “fast” scintillation light component, consisting of 15% of the total light output, is emitted in wavelength bands of 220 and 195 nm with a decay time varying between 600 and 800 ps. Due to this short wavelength, a quartz window photomultiplier tube with optical grease having good ultraviolet transparency is required in order to permit transmission of the ultraviolet wavelengths from the BaF<sub>2</sub> scintillator to the photocathode of the photomultiplier tube. Otherwise, the much slower scintillation light component, consisting of the remaining 85% of the total light output, emitted by the BaF<sub>2</sub> scintillator centered at 310 nm with a decay time of 630 ns will be detected. This slower decay time results in a much worse timing and energy resolution of the detector package [40]. The BaF<sub>2</sub> crystalline scintillator used in this study has cylindrical dimensions of 1” diameter x 1” thick.

### 3.2.2 Photomultiplier Tubes

The photomultiplier tube is the detector of choice for positron annihilation lifetime spectroscopy due to its fast timing response and good timing resolution in comparison to other gamma detectors. Following the incident gamma through to the photomultiplier tube (PMT) output pulse, the incident gamma first must pass through the input window. This photocathode window serves two purposes. First, since the various components related to photomultiplication are located within a vacuum, the input window serves to separate the internal components from the exterior environment. Secondly, the photocathode window acts as a filter to allow for the transmission of a certain range of wavelengths into the interior structure of the photomultiplier tube. This range is selected by the optical transmission properties of the photocathode window and varies depending on the specific use for the photomultiplier tube. Some materials, such as borosilicate glass, have a transmission range most useful in the visible region. Others such as MgF<sub>2</sub>, sapphire and quartz are used to allow for the transmission of wavelengths in the ultraviolet region, with MgF<sub>2</sub> allowing for the transmission of wavelengths as low as 115 nanometers [14].

Once passing through the photocathode window, the incident gamma strikes the photocathode itself. The photocathode relies on the principle of the photoelectric

effect, discussed in Sec. 2.3.1, to create a single electron from the energy of the incident gamma. This is a probabilistic process, with the ratio of output electrons to incident photons referred to as the quantum efficiency. Most photomultiplier tubes have a quantum efficient of approximately 25%. In order to emit photoelectrons in a practical manner, the photocathode material is typically a compound semiconductor, mostly comprised of an alkali metal with a low work function. Similar to the processes detailed in Sec. 3.2.1 for inorganic scintillators, the energy of the incident gamma is absorbed by an electron in the valence band, resulting in the excitation of the valence band electron. Provided the electron is provided with enough energy to overcome the vacuum level barrier, it is diffused and emitted as a photoelectron towards the dynode stages of the PMT. Like the photocathode window, the photocathode material has a specific range of wavelengths to which it is sensitive [14, 21, 25].

Once emitted from the photocathode, the photoelectron undergoes a cascading multiplication effect by means of the various stages of dynodes within the body of the photomultiplier tube. The dynodes are semi-curved secondary emissive materials which are coated on a substrate electrode which serve to produce multiple secondary electrons from a single primary electron. The dynodes are positioned within the photomultiplier tube as to minimize electron transit time spread through the dynode stages and detector rise time while maximizing the photoelectron multiplication factor. Typical photoelectron amplification ranges from 10 to  $10^8$  [14]. The amplified signals are collected near the base of the PMT and output through the dynode (positive signal) and anode (negative signal). For this PALS experiment, the dynode signal is used for energy information while the anode signal is used for timing information.

The photomultiplier tubes chosen for this experiment are the Hamamatsu R3377, which is a 51 mm diameter head-on photomultiplier with a quartz window, allowing for the acceptance of photons ranging from 160 nm to 650 nm. This permits the fast component of the BaF<sub>2</sub> scintillation emission band to be detected by the PMT, as mentioned in Sec. 3.2.1. The R3377 also offers excellent timing resolution, as evident by its manufacturer specified 0.7 ns rise time and 0.37 ns transit time spread [15]. The PMTs were custom modified by Hamamatsu to include a separate dynode output from the last dynode stage for the purpose of collecting energy information separate from the timing information given by the anode output. For source-based studies, the photomultiplier tubes are positioned 180° from each other as seen in Fig. 3.2.



**Figure 3.2:** Experimental configuration of photomultiplier tubes when completing source-based studies

### 3.3 Calibration of Equipment

In order to use the spectrometer to distinguish between undamaged samples and samples of varying damage, it is critical to determine the minimum timing resolution of the photomultiplier tube and associated data acquisition electronics. There are several parameters which can affect the final measured optimal timing resolution of the system, such as the voltage settings on the detectors, the length of the constant fraction delay cable, the geometry and type of scintillator, walk and timing jitter within the electronics and impedance mismatches between electronic modules. The proceeding sections describe how each piece of equipment along this circuit is calibrated and set to produce the lifetime of positrons within materials.

#### 3.3.1 Photomultiplier Tubes

The first major component, aside from the choice in scintillating material, is the photomultiplier tube (PMT). After properly interfacing the chosen scintillator and photocathode window together with the correct type of optical grease and wrapping the detector to protect from light leaks, each PMT is connected to a high voltage power supply (HVPS). Using RG-223/U coaxial cables, each PMT anode output is connected to a Tektronix TDS 2024 oscilloscope using a  $50\text{-}\Omega$  through-line terminator. After placing a  $^{137}\text{Cs}$  source between the two photomultiplier tubes, the voltage is initially set to -2000 V. Using the oscilloscope, the voltages of each photomultiplier detector is adjusted until the signal amplitudes are within at least 1.5x of each other in order to gain match the PMT signal response [32]. A useful starting point is to set

the oscilloscope to trigger at approximately 250 mV and adjust the bias on each PMT until they each have a rate of approximately 1kHz as measured on an oscilloscope. Once the PALS system is more fully assembled, the detector bias is further adjusted through matching either the channel numbers of the  $^{137}\text{Cs}$  photopeak centroid or the  $^{137}\text{Cs}$  Compton edge on both the START and STOP channels, as discussed in Sec. 3.5.

Two distinct categories of experiments are conducted with the spectrometer. These are experiments conducted with the fast plastic scintillator and those conducted with the  $\text{BaF}_2$  scintillator. Given considerations to the functional range of input voltages of the discriminators, for reasons discussed in Sec. 3.3.2, Fig. 3.3 depicts the effect of different detector biases on the overall timing resolution of the spectrometer. As the choice in scintillator effects the optimal timing resolution, tests were conducted to given an initial estimate of the best possible timing resolution of the spectrometer for each scintillator used in this study. When using the conical fast plastic scintillators, the TAC START PMT is biased to -1703 V while the TAC STOP PMT is biased to -1572 V. When using the  $\text{BaF}_2$  scintillators, the TAC START PMT is biased to -2705 V and the TAC STOP PMT is biased to -3001 V. Further optimization is completed in Sec. 3.3.2.

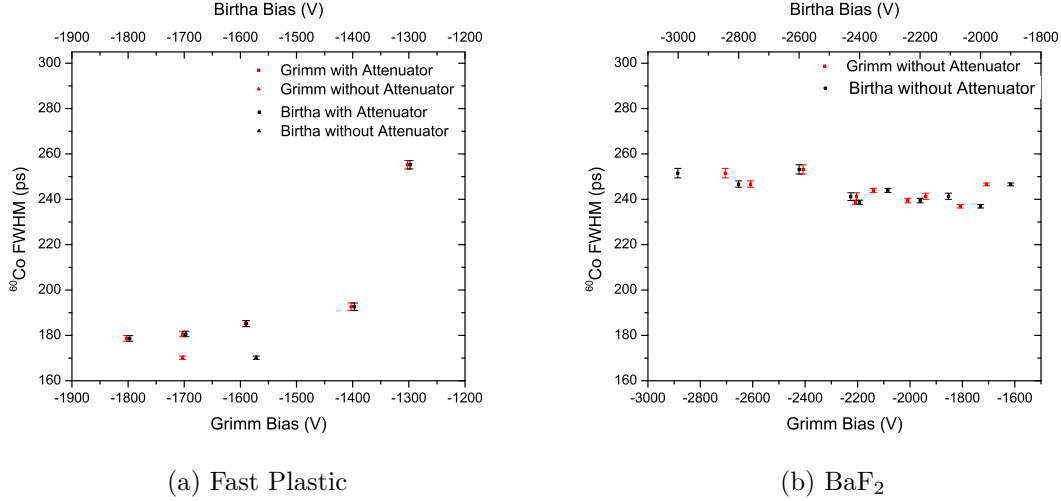


**Figure 3.3:** Determination of spectrometer timing resolution as a function of the detector bias for the (a) fast plastic and (b)  $\text{BaF}_2$  scintillators using Hamamatsu R3377 photomultiplier tubes. This plot is used to determine the optimal settings of the bias on each detector. The FWHM refers to the FWHM of the timing peak created by the START 1173.2 keV and STOP 1332.5 keV decay gammas of  $^{60}\text{Co}$ .

The time resolution of the photomultiplier tubes is experimentally determined by means of a pulse generator, a blue wavelength LED, an opaque cylinder and a Tektronix DPO 4104B oscilloscope. The pulse generator is set to drive the LED at a frequency of 500 Hz with an amplitude of 3.00 V with a pulse width of 10 ns. The LED is placed in the center of the opaque cylinder with the two photomultiplier tubes inserted into each end of the cylinder. The cylinder is sealed at the edges to create an internal environment which is light-tight. At a bias of -1572 V, the rise time of the START PMT is found to be  $2.2 \pm 0.10$  ns while at a bias of -1703 V, the rise time of the STOP PMT is found to be  $2.3 \pm 0.16$  ns. The two PMTs were then tested without the LED to measure the rise time of the dark current of each PMT. At a bias of -1572 V, the rise time of the START PMT is found to be  $1.0 \pm 0.05$  ns while at a bias of -1703 V, the rise time of the STOP PMT is found to be  $1.1 \pm 0.04$  ns.

### 3.3.2 Constant Fraction Discriminator

The second major set of components in the spectrometer are the Constant Fraction Discriminator (CFD) and Constant Fraction Differential Discriminator (CFDD). These devices serve as the gatekeepers for incoming signals from the anode output of each photomultiplier tube. To prevent damage to the discriminators, the photomultiplier tube bias settings should be such that the maximum dynode signal output amplitudes are less than -5 V for signals entering the 584 Constant Fraction Discriminator and less than -10 V for signals entering the 583B Constant Fraction Differential Discriminator. Additionally, it should be noted that the functional signal amplitude discrimination thresholds for the 584 Constant Fraction Discriminator range from -5 mV to -1 V. The threshold range for signals entering the 583B Constant Fraction Differential Discriminator is -30 mV to -5V [32]. Input signal amplitudes greater than these thresholds will be passed through the discriminator to the Time to Amplitude Converter and included as candidates for coincident timing events.

Say for example the PMT is detecting signals from a  $^{22}\text{Na}$  source. As seen in Fig. 2.1a, the radionuclide emits a positron and a 1274 keV gamma. As the positron must then annihilate with an electron somewhere between its point of creation and the detector, it is assumed that the 1274 keV gamma is detected first by the photomultiplier tube. A resultant 511 keV annihilation gamma is later detected by the photomultiplier tube. As these two signals have unique energies, they are recorded by

the photomultiplier tube as having different voltage amplitudes. By setting voltage thresholds on the discriminators, it is possible to limit the accepted input signals to be above or within a window of a specific energy. In this example, the CFD would be used for the START signal and setup to trigger on voltages corresponding to gamma energies of 1274 keV or higher. The CFDD would be used for the STOP signal and set to build a window around the 511 keV signal, discarding any signals with energies corresponding to voltages above or below the set thresholds. It is by this means that it is possible to differentiate between the two photomultiplier tubes as START and STOP signals based upon the desired photon energies. In order to achieve this with some degree of accuracy, it is necessary to calibrate the following three features of the discriminators.

### **Blocking Width**

Suppose for example a signal is detected by a photomultiplier tube and it begins being processed by the various NIM electronics. As this signal travels along the various circuitry pathways within the electronics, the signal requires a minimum amount of time to be processed. If while this signal is being processed, a second signal is detected and begins to also be processed by the electronics, the final signal may exhibit features known as pulse pile-up. In this effect, there exists a slight time difference between two incoming signals, yet the difference is small enough to permit the signal amplitudes to be treated as a single pulse by the electronics with a convolution of the original signal amplitudes and pulse widths. This results in a false representation of the recorded spectrum [21].

In order to prevent this from occurring, a feature known as the blocking width is set such that if a signal is detected and has begun being processed by the electronics, the constant fraction discriminator prohibits any new signals from being accepted for the timing width of the window designated by the blocking width [32]. For the PALS experiment, this blocking width is set to 500 ns, providing ample processing time with room for error.

### **Walk**

The walk effect is the result of variations in the amplitude and rise time of incoming signals to the discriminator. While these variations in the input signals may be merely the result of statistical fluctuations or signal noise, they are important to correct for as

they affect the triggering used by the discriminator used to send a START or STOP pulse to the Time to Amplitude Converter (TAC). Careful selection of the time-pickoff method used by the discriminator based upon the experimental parameters helps to reduce this effect. For the purposes of the positron lifetime system, the Constant-Fraction Triggering method gives the best possible timing resolution as it greatly reduces the effect of walk on the discriminator triggering. The walk is carefully adjusted according to manufacturer guidelines each time the detector bias or length of the constant fraction delay cable is changed [25, 32].

### Constant Fraction Delay Cable

The constant fraction delay cable is a critical component of the Constant Fraction Discriminator as it completes the circuitry within the module. The length of the Constant Fraction Delay cable is solely dependent upon the rise-time of the anode output of each PMT and since each individual PMT has its own internal characteristics, it is expected that each PMT would have its own custom length Constant Fraction Delay cable. From the ORTEC manual on the Constant Fraction Discriminator, a starting point in determining the length of the cable is given by:

$$t_{cable} = 1.1 t_{rise} - 0.8 \text{ ns} \quad (3.1)$$

where  $t_{rise}$  is the rise-time of the anode pulse and the subtraction of 0.8 ns refers to the internal delay of the CFD module circuitry [32]. However, this formula does not take into account the signal propagation through the RG-223/U cable used for the Constant Fraction Delay Cable. Modifying Eq. 3.1, a better starting point to determine the length of the cable is:

$$l_{cable} = (1.1 t_{rise} - 0.8 \text{ ns})(0.66c) \quad (3.2)$$

where 0.66c refers to the signal propagation velocity through the RG-223 cable. As this is only a starting point, a more in-depth study is required to determine the correct cable lengths to use for the CF Delay Cable with the PMTs in question.

A lengthy set of trials are conducted using the cylindrical BaF<sub>2</sub> crystalline and the BC-418 truncated cone fast plastic scintillators, each wrapped in white Teflon tape and properly interfaced with the Hamamatsu R3377 PMTs using either BaF<sub>2</sub> grease or BC-630 silicone optical grease from Saint-Gobain. Using the voltages as

determined in Sec. 3.3.1 and the setup described in Sec. 3.4, the lengths of the CF Delay Cables are varied in increments of 10% to determine the optimal cable length which provides the minimum timing resolution.

Using the near coincident gammas of  $^{60}\text{Co}$  as depicted in Fig. 2.1c, the results of the cable length trials are demonstrated in Fig. 3.4.

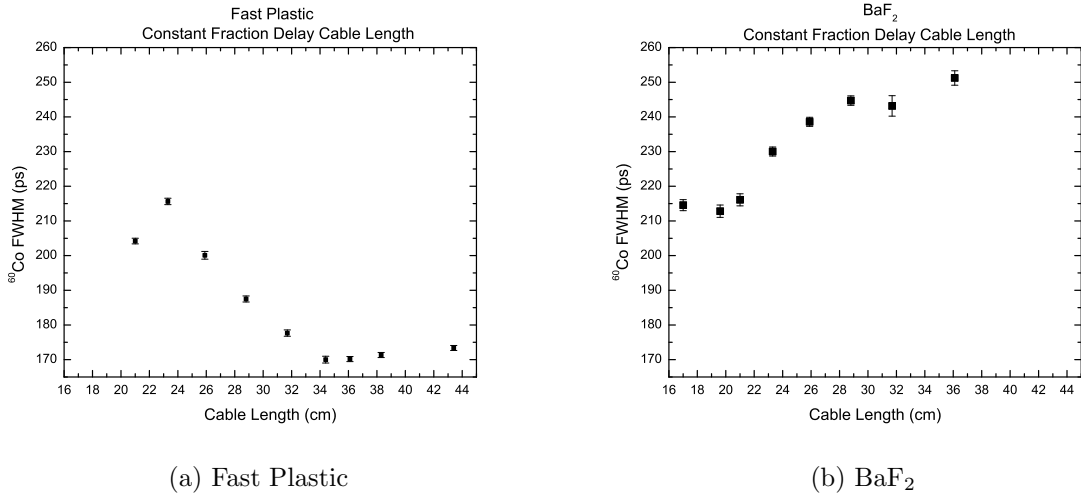


**Figure 3.4:** The optimization of the timing resolution as a function of CF Delay Cable lengths for the (a) fast plastic and (b)  $\text{BaF}_2$  scintillators using Hamamatsu R3377 photomultiplier tubes

As seen in Fig. 3.4a, the 36.1 cm long cables provided the best timing resolution of  $170.172 \pm 0.73$  ps when using the conical fast plastic scintillators and are thus used as the CF Delay Cables. When using the  $\text{BaF}_2$  scintillators using the bias settings from Sec. 3.3.1, the 19.6 cm cables provided the best timing resolution of  $213.342 \pm 1.79$  ps.

### 3.3.3 Analog to Digital Converter

The Analog to Digital Converter, or ADC, makes up part of the Multi-Channel Analyzer Data Acquisition System, namely the hardware component. The ADC used in this experiment is the FAST Comtec 7070, a 13-bit ADC. The software component, also made by FAST Comtec, is version 1.67 of the MPA-NT software package. The timing and energy calibrations within the software are discussed in Section 3.3.7.

In order to calibrate the ADC, a variety of equipment not used elsewhere in this

experiment are required, namely a NaI(Tl) detector, an ORTEC 113 PreAmplifier, and either an ORTEC 671 Spectroscopy Amplifier or ORTEC 672 Spectroscopy Amplifier. The sodium iodide doped with thallium detector, or NaI(Tl) detector, features much greater energy resolution than a photomultiplier tube at the expense of timing resolution. The Spectroscopy Amplifier accepts signals from a preamplifier and shapes the signal to become a useful energy spectroscopy input to a Multi-Channel Analyzer [32].

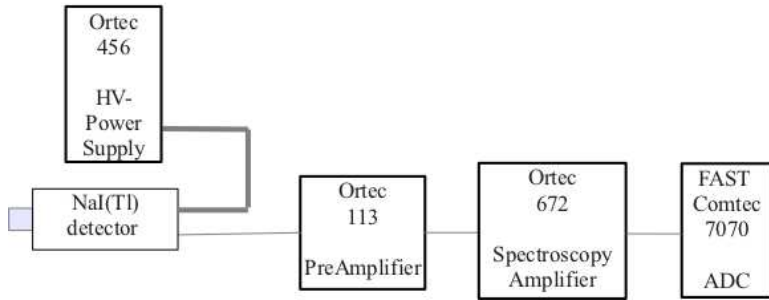


**Figure 3.5:** Flow chart of PALS system setup to perform calibration of ADC

Placing a  $^{22}\text{Na}$  source in front of the NaI(Tl) detector, the dynode output of the detector is connected to the ORTEC 113 PreAmplifier via a RG-223/U coaxial cable, set to  $100\text{ pF}$ , and then connected to the NORM input of the Spectroscopy Amplifier using an RG-62 coaxial cable as seen in Fig. 3.5. The Input Polarity is set according to the polarity of the signal from the NaI(Tl) detector, the Pole Zero adjustment is selected to *AUTO* and the UNI SHAPING is set to *Gaussian*. The settings of the Shaping Time, Course and Fine Gains are dependent upon the characteristics of the NaI(Tl) detector used. The UNIPOLAR output should be connected to the ADC input of both the START and STOP Energy ADCs using an RG-223/U coaxial cable. Finally, the ADC should be set such that the Conversion Gain is set to  $8k$  channels, Pulse Height Analysis (PHA) Mode is set and the Gate toggle switch is set to *Anti-Coinc*. Within the MPA-NT software, the ADC software settings should be set to reflect the 8192 channels selected on the ADC hardware.

After biasing the NaI(Tl) detector according to the manufacturer's specifications, the MPA-NT software is used to identify the 511 keV and 1274.5 keV photopeaks from the  $^{22}\text{Na}$  and the linear calibration tool is used to create a calibration line from the channel values of the centroids of the two photopeaks. The factory settings should be verified and if necessary, a small screwdriver is used to adjust the “zero” level of the ADC until the x-axis crossing of the linear calibration reads 0.0. This

process should be completed for all ADCs intended for use in the PALS experiment.

### 3.3.4 Time to Amplitude Converter

Once the signal passes through the START and STOP Constant Fraction Discriminators, the timing information is passed to the Time to Amplitude Converter (TAC), which converts the signal time between the START and STOP input pulses into an amplitude which is then passed on to the ADC. In order to determine the timing resolution of the system and positron lifetimes within samples, it is important to know the statistical binning by which the TAC and ADC accept data.

Using the system setup shown in Fig. 3.6, the TAC Range is set to  $50\text{ ns}$  and Multiplier to  $1$ . The ADC is then set such that the Conversion Gain is  $8k$ , PHA Mode is set and Gate toggle switch is set to *Anti-Coinc*. Finally, the delay module should give a total delay of  $1\text{ ns}$ . After running the MPA-NT software for a preset 5 seconds, the delay is increased by  $4\text{ ns}$  and the data collection continued. Repeating this for nine successive trials and determining the locations of the peak centroids, a calibration can be completed to determine the data binning in picoseconds per channel.

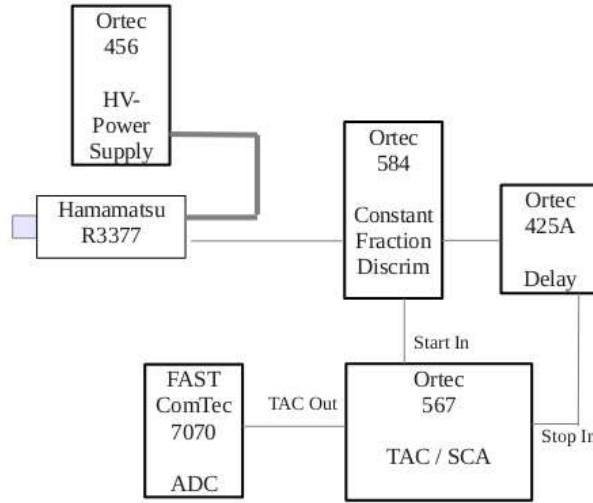


**Figure 3.6:** Flow chart of PALS system setup to perform calibration of Time to Amplitude Converter

Fig. 3.7 depicts the data for a typical TAC calibration using fast plastic scintillators. The calibration is determined by calculating the difference in peak centroids as

reported by MPA-NT, averaging the difference in peak centroid values for the nine data trials, and then dividing the time difference of four nanoseconds by the average of the channels to obtain the number of picoseconds per channel [32]. The calibration should be completed for each occurrence of a change in the high voltage settings and the calibration settings of the discriminator.

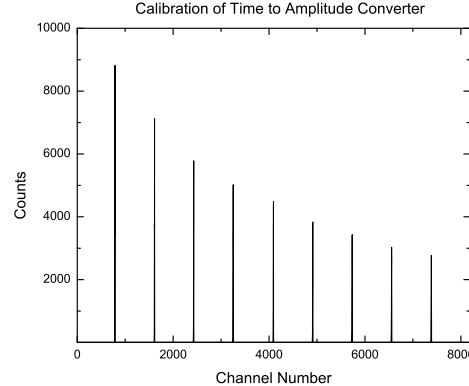


**Figure 3.7:** MPA-NT output from PALS with fast plastic scintillators to perform calibration of Time to Amplitude Converter

Using the data from Fig. 3.7, the PALS system is found to have a timing calibration of 4.851 ps/channel when using the conical fast plastic scintillators and a timing calibration of 4.851 ps/channel when using the BaF<sub>2</sub> scintillators.

The data obtained from the calibration of the TAC also provides a convenient method of determining the timing jitter of the system. Timing jitter results from noise and statistical fluctuations in the detector signal which are caused by factors such as variations in the yield of photons created in the scintillator, variations in the transit time of photons and electrons through the scintillator and photomultiplier tube, and gain variations in the dynode stages of the photomultiplier tube. The timing jitter is given by

$$\sigma_{\text{time}} = \frac{\sigma_n}{|\frac{dV}{dt}|}, \quad (3.3)$$

where  $\sigma_{\text{time}}$  is the timing jitter of the system,  $\sigma_n$  is the variance in voltage due to signal noise and statistical fluctuations, and  $dV/dt$  is the change in voltage over time of the signal [25, 32]. By averaging the FWHM of each of the peaks produced by the TAC calibration, it is possible to know the timing jitter of the system for each PMT

and associated electronic signal pathways. Using the signal from the STOP PMT, the PALS spectrometer is measured to have a timing jitter of  $25.54 \pm 0.32$  ps.

### 3.3.5 Amplifiers

Once the dynode signal leaves the photomultiplier tube, it immediately passes into an amplifier. The output signal of the amplifier is passed to the ADC, which records the dynode pulse height amplitudes and reports them as an associated channel number to create an energy spectrum. Thus it is important to insure that the same event is reported as having the same amplitude, regardless of whether it is detected in the START or STOP photomultiplier tube. Adjusting the amplifier course and fine gain settings allows for the individualized adjustment of the output of each photomultiplier tube so that the dynode signal pulse heights for gammas of equal energy are equal in amplitude and thus will fall into the same bin of the START and STOP channels of the MPA-NT software.

From Fig. 3.8, the dynode signal of each PMT is input into an amplifier. The amplifier UNIPOLAR output is then input into an oscilloscope. While any radionuclie source can be used, it is best to use a source which produces a monoenergetic pulse, such as  $^{137}\text{Cs}$  or  $^{54}\text{Mn}$ . This is done so that only a single primary amplitude pulse is observed on the oscilloscope, making it easier for the experimenter to discern the gamma energy from that of background in each oscilloscope channel.

Assuming the gain of the photomultiplier tubes to be equalized as done in Sec. 3.3.1, the amplifier signals are also equalized by adjusting the individual fine gains until the amplitudes of the UNIPOLAR output signals from each amplifier are equal on an oscilloscope. As the amplifier outputs will later go directly into the ADCs, it is important to ensure that the amplifier signals do not exceed the 8 V maximum allowance of the ADCs. Otherwise, damage to the ADC circuitry may occur.

### 3.3.6 Gate and Delay Generators

Once the discriminators and amplifiers have been calibrated and adjusted, the Gate and Delay Generator can be adjusted, as it is used to visually determine the corresponding energies of the anode signals passed through the discriminator to the

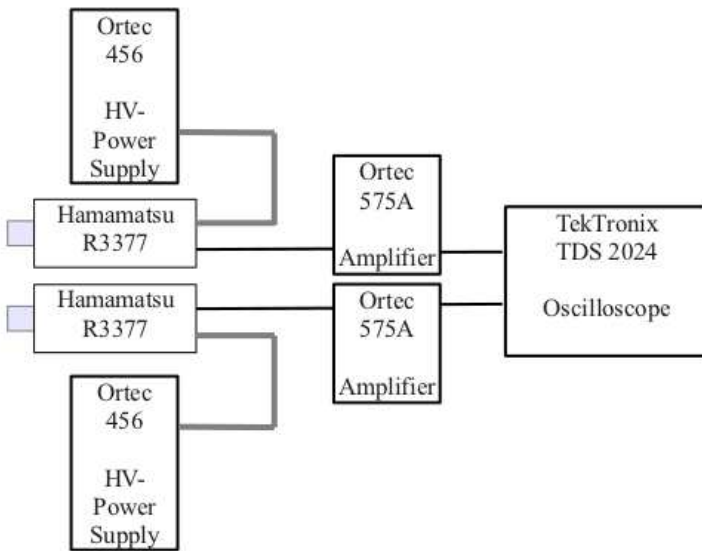


**Figure 3.8:** Flow chart of PALS system setup to perform calibration of Amplifiers

remainder of the timing circuitry. As its name implies, the Gate and Delay Generator creates a logical pulse which can be used as a gate input for the ADC.

Following the diagram in Fig. 3.9, both the anode and dynode signals from the photomultiplier tubes are employed to adjust the Gate and Delay Generators. The dynode signal is first amplified and then input directly into Channel 1 of the oscilloscope using a  $50\text{-}\Omega$  through-line terminator. The anode signal is first passed through the discriminator, where a logic pulse from the discriminator is then passed to the Gate and Delay Generator. The width, amplitude, and time delay of this logic pulse are adjusted by the Gate and Delay Generator and then passed to Channel 2 of the oscilloscope using a  $50\text{-}\Omega$  through-line terminator. While triggering the oscilloscope off of Channel 2, the delay dial on the Gate and Delay Generator is adjusted until the gate envelops the positive portion of the input signal on Channel 1 as shown in Fig. 3.10. This is done because the ADC Gate input requires a positive pulse and thus ignores any incoming negative signals.

Additionally, the amplitude of the logic pulse should be at least +2 V to ensure that it is recognized by the FAST Comtec 7070 ADC. This complete process should be completed twice, once for each photomultiplier tube used in the standard coincidence setup.

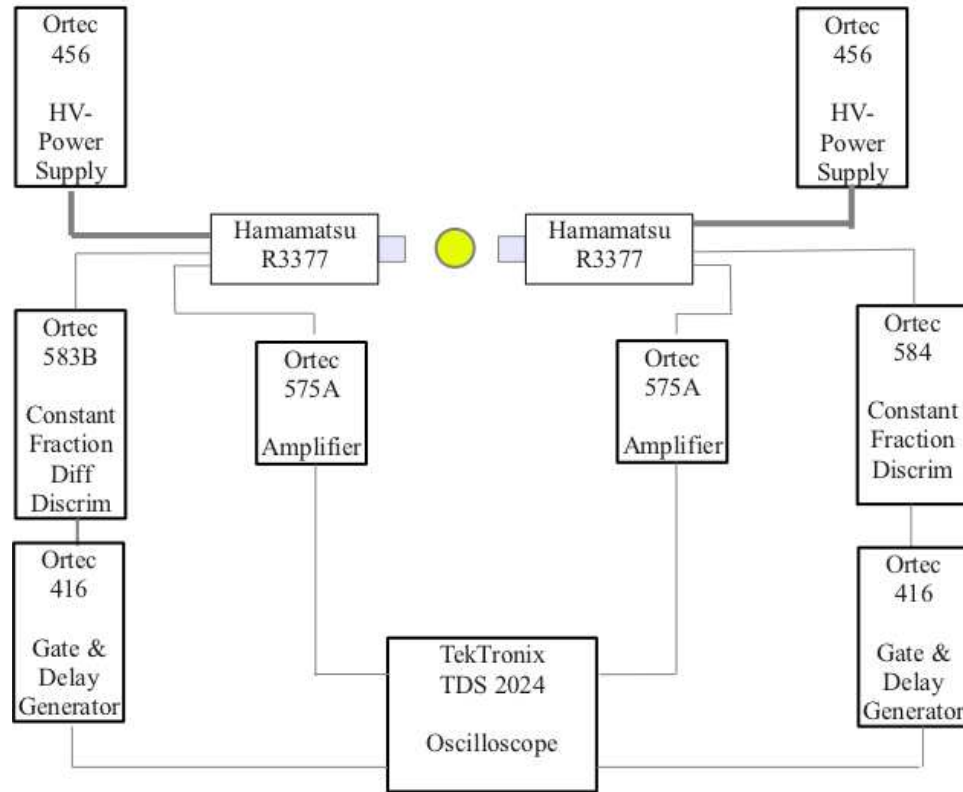


**Figure 3.9:** Flow chart of PALS system set up to perform calibration of Gate and Delay Generators

### 3.3.7 ADC Timing and Energy Calibrations

#### ADC Energy Calibration

The calibration of the MPA-NT software in the energy channels is extremely useful in that it allows for the determination of the energies of any Compton edge or photopeak features which may be visible within the recorded energy spectrum. To do so requires a careful selection of radionuclide sources as well as a complicated setup of NIMs (See Fig. 3.11). While the setup is the same regardless of the choice in scintillator, the method by which the calibration is calculated is dependent upon the choice of scintillator material. If a BaF<sub>2</sub> scintillator is chosen, then it is possible to perform the energy calibrations from the photopeaks produced by each radionuclide. Otherwise, the Compton edges are used in the case of fast plastic scintillators.

The setup for the energy calibrations is shown in Figure 3.11. In this setup, the ADC is set such that the Conversion Gain is  $8k$ , PHA Mode is set and the energy

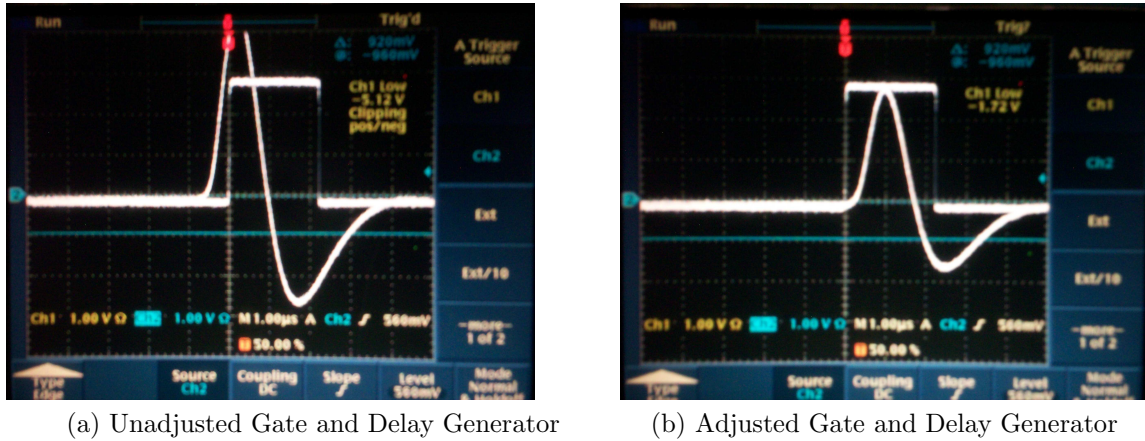


**Figure 3.10:** Images of the (a) unadjusted and (b) adjusted Gate and Delay Generator as seen on Tektronix TDS 2024 oscilloscope

ADC Gate toggle switches are set to *Coinc* while the timing ADC Gate toggle switch is set to *Anti-Coinc*. The MPA-NT software is set such that all three ADCs are using the full bit range of 8192 channels.

If using the BaF<sub>2</sub> scintillator, the <sup>22</sup>Na, <sup>137</sup>Cs, and <sup>54</sup>Mn sources should be used in separate data runs in order to identify the 1274.5 keV photopeak of <sup>22</sup>Na, the 661.7 keV photopeak of <sup>137</sup>Cs, and the 834.9 keV photopeak of <sup>54</sup>Mn. After running each trial, allowing for the collection of sufficient statistics for the photopeaks of each source to develop, the MPA-NT software calibration feature is used to calibrate the energy per channel using a linear fit of the centroids of the Gaussian fits of each photopeak.

If using a fast plastic scintillator, the task becomes slightly more complicated as there are no photopeaks present due to the smaller photoabsorption cross-section of the scintillating material resulting from the lower density of the material, as discussed in Sec. 2.3. Using the same sources as with the BaF<sub>2</sub> scintillator, the Compton edges must be identified for the 1274.5 keV gamma emitted by <sup>22</sup>Na, the 661.7 keV Compton edge of <sup>137</sup>Cs, and the 834.9 keV Compton edge of <sup>54</sup>Mn. In order to calibrate from the Compton edges, the Compton scattering formula, Eq. 2.24, must be modified to obtain the energy of the recoil electron at the Compton edge. This calibration is

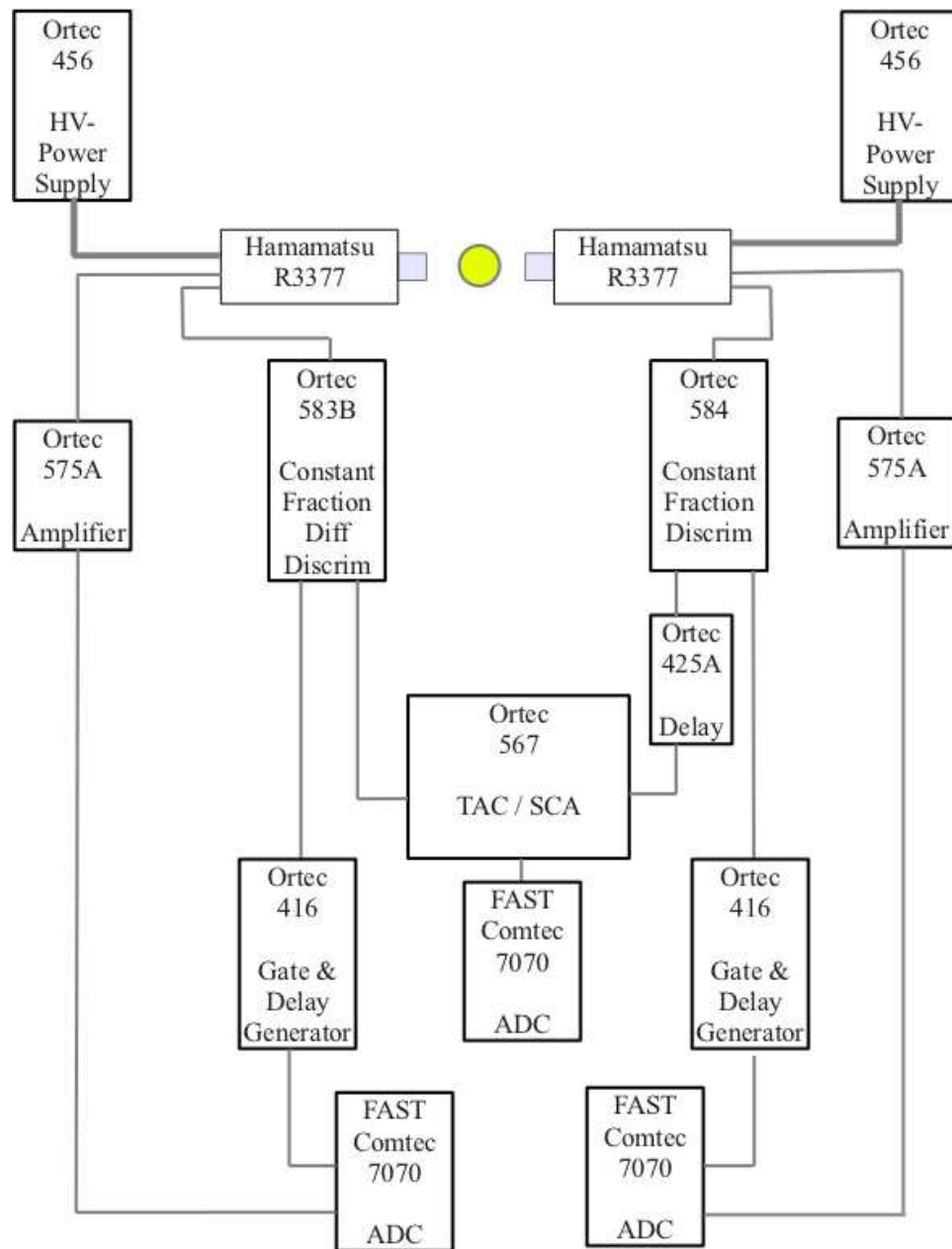


**Figure 3.11:** Flow chart of PALS system set up to perform energy calibration of MPA-NT software and perform positron lifetime measurements

done by using the formula

$$E - E' = E - \frac{E}{1 + \frac{(1 - \cos(\pi))E}{m_e c^2}} = \frac{2E^2}{2E + m_e c^2}, \quad (3.4)$$

where  $E$  is the full energy of the gamma emitted by the radionuclide and  $m_e$  is the mass of the electron. The angle of deflection  $\theta$  is set to  $\pi$  as this represents the angle at which the maximum amount of energy is transferred by the photon to the electron, as detailed in Sec. 2.6.1. From Eq. 3.4, the energies to use in the calibration for each Compton edge are 1061.7 keV for  $^{22}\text{Na}$ , 477.3 keV for  $^{137}\text{Cs}$ , and 639.2 keV for  $^{54}\text{Mn}$ . The energy channels are calibrated using a linear fit and verified with a  $^{60}\text{Co}$  source.

### ADC Timing Calibration

Once the energy calibrations have been completed, the timing calibrations can be done. Although this can be achieved by running the PALS experiment to obtain a timing peak and then multiplying the FWHM in channels by the value obtained in Sec. 3.3.4, it is also possible to calibrate the MPA-NT software to display the FWHM in terms of nanoseconds rather than in channels.

Using the setup in Fig. 3.11 and a  $^{60}\text{Co}$  source, the MPA-NT software and a delay is initially used to center the generated peak in the timing ADC channel such that the centroid of the peak appears around channel number 4000 in order to prevent a loss in data due to signals registering as being above or below the range of the ADC. After running the software to generate sufficient statistics to produce a good Gaussian peak, the delay is shifted by 8 ns and the data collection is continued. This process is repeated in equal intervals producing peaks located at -16 ns, -8 ns, 0 ns, 8 ns and 16 ns. The MPA-NT calibration tool can then be used to calibrate the timing ADC channel within the software. For experiments conducted with both the fast plastic and  $\text{BaF}_2$  scintillators, the timing calibration for this spectrometer was found to be approximately 4.85 ps per channel.

## 3.4 Determination of Optimal Timing Resolution

For the purposes of defect density assessment, it is important to be able to discern between various positron lifetime signals. As the timing signals within metals are

on the order of only a few hundred picoseconds, it is easy for electronic jitter, in addition to the contribution of the transit time across the various NIM electronics, to overwhelm the signal of the material under study. Therefore, it is absolutely critical to reach the optimal timing resolution of the entire system.

In order to test this value, the setup depicted in Fig. 3.11 is used with a  $^{60}\text{Co}$  source. Following the procedures in Sec. 3.3.7, the START and STOP Constant Fraction Discriminators are set such that the 1173.2 keV and 1332.5 keV gamma photopeaks (or Compton edges in the case of the plastic scintillators) are isolated in the energy spectrum. Using Fig. 2.1c as a guide, the photopeak or Compton edge associated with the 1173.2 keV gamma is isolated as the TAC START signal using the CFDD while the CFD is set to discriminate the signal to only allow the region resulting from the photopeak or Compton edge associated with the 1332.5 keV gamma for the TAC STOP signal. Since the emission of the second gamma from  $^{60}\text{Co}$  occurs in less than 5 picoseconds from the emission of the 1173.2 keV gamma, which is significantly less than the positron lifetime spectrometer is capable of resolving, the resultant timing peak is a very good indication of the overall resolution of the spectrometer.

The MPA-NT software fits this peak as a single Gaussian with a linear background. The FWHM of this peak in picoseconds is defined as the timing resolution of the system.

### 3.5 Determination of Detector Energy Resolution

As the output of the photomultiplier tubes provide the signals which generate the energy spectra used to place thresholds on the START and STOP CFDs, it is important to determine the minimum energy resolution of the photomultiplier tubes. This allows for the determination of the uncertainty in the energy calibration completed in Section 3.3.7. In order to make this determination, the  $\text{BaF}_2$  scintillators and appropriate ultraviolet transparent optical grease should be used in order to permit the detection of the  $^{137}\text{Cs}$  photopeak with the best possible energy resolution. Using the same setup as shown in Fig. 3.11, the PALS system is run without any thresholds set on either of the discriminators and allowed to collect enough data to ensure a good statistical sampling. After appropriate data collection, the values of the peak centroids in both the START and STOP energy spectra, as well as the energy resolution

of the detectors, are determined.

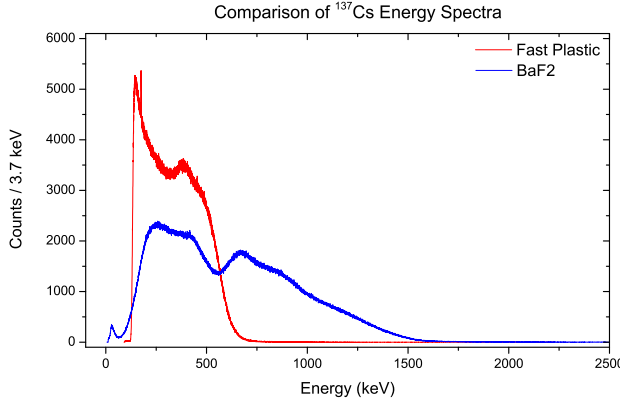


**Figure 3.12:** The resultant energy spectrum of  $^{137}\text{Cs}$  as seen by the fast plastic and  $\text{BaF}_2$  scintillators.

Since the gammas from the  $^{137}\text{Cs}$  source detected by the START and STOP PMTs have the same energy, the resultant photopeaks should be recorded in the same range of ADC channels. The adjustment of the bias on the PMTs and the fine gain of the amplifiers, resulting in the signals collected being placed into a higher or lower channel bin in the software, makes it possible to place the 661.7 keV photopeak centroid in the same, or nearly the same, channel in both the START and STOP energy spectra. As mentioned in Sec. 3.3.1, this allows the photomultiplier tubes to be more finely calibrated.

The pulse height amplitude is a useful quantity which imparts the energy resolution of the detector. It is found as:

$$\text{P.H.A.} = \frac{\text{FWHM of Full Energy Photopeak}}{\text{Peak Centroid Channel Number}}. \quad (3.5)$$

Applying this, the Hamamatsu R3377 photomultiplier tube used as the START PMT has an energy resolution of  $17.89 \pm 0.96\%$  at -2705 V while the photomultiplier tube used as the STOP PMT has an energy resolution of  $16.54 \pm 1.20\%$  at -3001 V [21].

## 3.6 Discrimination Window Settings

### 3.6.1 Source-Based Experiments

Once each hardware component is calibrated and the MPA-NT timing and energy channels have been calibrated, the spectrometer is ready to begin collecting positron lifetime data using the configuration given in Fig. 3.11. For the purposes of this thesis, the two main functions of the spectrometer are to verify experimentally known positron lifetimes in high-purity sample materials using a  $^{22}\text{Na}$  source and to eventually determine the feasibility of using the PALS technique in conjunction with a continuous wave accelerator. The spectrometer system setup is easier when using the  $^{22}\text{Na}$  source, as the PMT bias and amplifier settings have a greater range of options without the energy spectrum being above the binning range of 8192 channels created by the ADC. This becomes a greater challenge with accelerator-based, gamma-induced positron annihilation spectroscopy (AG-PAS), discussed in Sec. 3.6.2.

In order to set the spectrometer to perform source-based measurements of positron lifetimes in materials, the setup depicted in Fig. 3.11 is used with a  $^{22}\text{Na}$  source. Following the procedures in Sec. 3.3.7, the START and STOP Constant Fraction Discriminators are set such that the 511 keV and 1274.5 keV gamma photopeaks (or Compton edges in the case of the plastic scintillators) are selected, respectively. Using Fig. 2.1a and the discussion in Sec. 3.1.1 as a guide, the photopeak or Compton edge associated with the 1274.5 keV gamma is used as the TAC START signal using the CFD while the CFDD is set to discriminate the signal to only allow the region resulting from the photopeak or Compton edge associated with the 511 keV gamma for the TAC STOP signal.

When using the fast plastic scintillators, the discriminator windows are set such as to accept a reasonable amount of the Compton spectrum leading up to the Compton edge, described in Sec. 2.6.1. Using the energy resolution of the system as described in Sec. 3.5 as a guide, the CFDD windows are set to include gamma energies ranging from 30% below the 340 keV Compton edge to 10% above the Compton edge. The lower level discriminator of the CFD is set to include signals from gammas with energies above 30% below the 1062 keV Compton edge. The application of the discriminator windows when using fast plastic scintillators is shown in Fig. 3.13.

When using the  $\text{BaF}_2$  scintillators, the discriminator windows are set such as to accept only the respective TAC START and TAC STOP photopeaks. Again, using

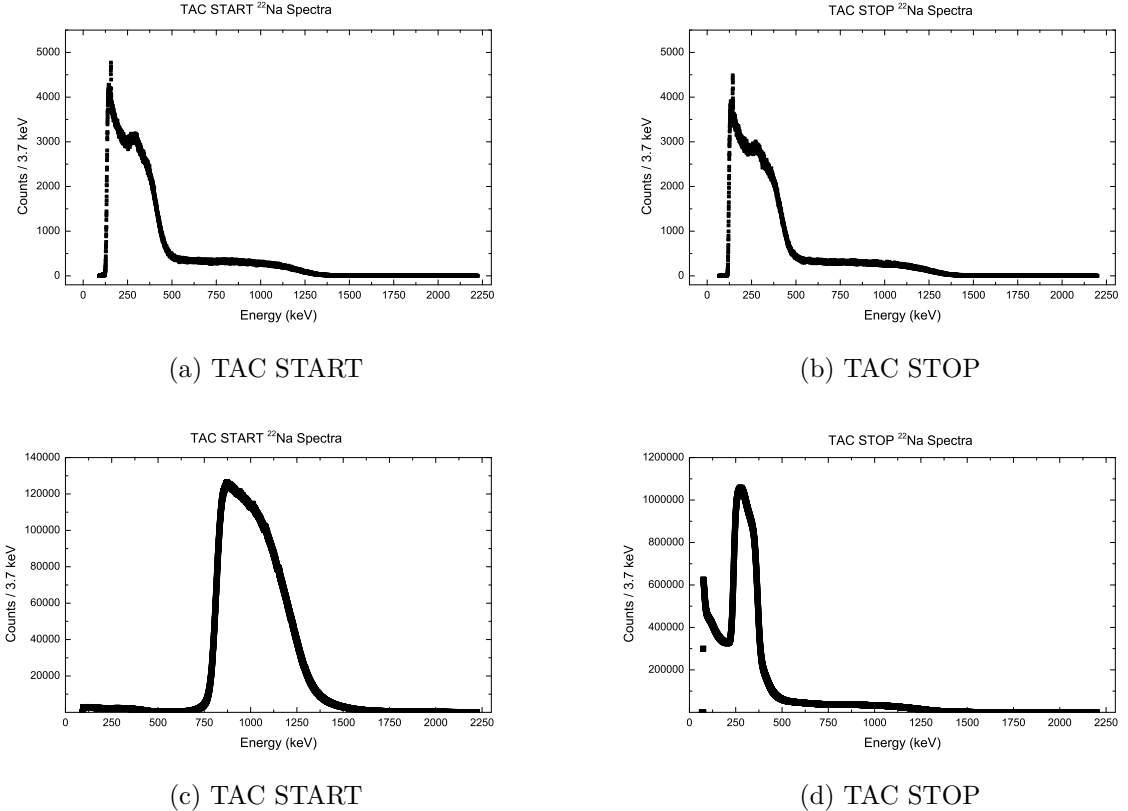


**Figure 3.13:** The energy spectrum of  $^{22}\text{Na}$  before and after setting discrimination windows when using the fast plastic scintillators. Fig. 3.13a and 3.13b depict the energy spectrum of  $^{22}\text{Na}$  before setting discrimination windows while Fig. 3.13c and 3.13d depict the energy spectrum with the proper discrimination windows applied.

the energy resolution of the system as described in Sec. 3.5 as a guide, CFDD windows are set to include gamma energies between  $\pm 20\%$  of the 511 keV photopeak centroid. The lower level discriminator of the CFD is set to include signals from gammas with energies above 20% below the 1274.5 keV photopeak centroid.

### 3.6.2 Accelerator-Based Experiments

Unlike source-based experiments in which there are only two photon energies, the accelerator produces a wide range of photon energies to choose as the TAC START or TAC STOP signals. As given by the branching ratios of the products of the reaction given in Fig. 2.3 and Eq. 2.4, the 1.78 MeV gamma is created more frequently than higher energy gammas. The 1.78 MeV gamma, or any other gamma of energy

greater than this, is experimentally time delayed for the purpose of being used as a guaranteed TAC STOP signal in timing coincidence measurements. From Fig. 2.3, it is seen that while there are many gammas produced in the  $^{27}\text{Al}(p, \gamma)^{28}\text{Si}$  reaction which are capable of producing a 511 keV TAC START signal by means of pair production within the material, the use of 1.78 keV gamma as a STOP signal is advantageous as it occurs much more frequently than any other gammas produced in this proton capture reaction. If the START and STOP roles were reversed, as one might naturally expect, the spectrometer could potentially wait the full discriminator blocking width of 500 ns before registering a STOP signal or dropping the original START signal altogether without recording a coincidence event. This would significantly reduce the count rate and severely increase the spectrometer deadtime. The 511 keV annihilation gamma produced within the sample is then used as the TAC START signal.

The photomultiplier tube bias and amplifier settings pose a greater challenge when using the continuous wave accelerator to deposit positrons in the material by means of pair production. In using the 1.78 MeV gamma, or any gammas of greater energy, as the TAC STOP signal, the dynode signal amplitude as seen by the STOP discriminator is already greater than the 1.33 MeV gamma produced by the  $^{60}\text{Co}$  source used in calibrations. As a result, careful considerations to detector bias and amplifier settings must be taken to avoid damage to the equipment. If the detector bias and amplifier settings are calibrated using common sources with energies in the hundreds of keV, then signals with voltages in excess of -5 V are frequently produced due to the large range of incident photon energies from the  $^{27}\text{Al}(p, \gamma)^{28}\text{Si}$  reaction. As is discussed in Sec. 3.3.2, the CFD will automatically pass any signal above -1 V to the TAC while the CFDD will automatically pass any signal above -5 V to the TAC. Signals passing to the CFD above -5 V and to the CFDD above -10 V can severely damage the discriminator units.

Additionally, if the detector bias is too low, then the necessary upper and lower level discrimination windows necessary for the 511 keV signal may be much smaller than the ability of the CFDD to differentiate. The minimum threshold of the CFDD is 10 mV, meaning that if the input signal amplitude representing the photon energies of a photopeak is less than 10 mV, then a window cannot be made small enough to completely exclude any photon energies outside of the region of the photopeak.

## 3.7 Metallic Samples

Thin metallic foils of aluminum, copper, nickel and lead were obtained from various sources for source-based experiments in order to obtain lifetime data. Additionally, two cylindrical metallic rods of varying dimensions and material were obtained from Alfa-Aesar for use in this experiment and cut into approximately 1 mm thick disks. Two disk sets of each sample and configuration are created for testing. The first set is annealed according to the specifications given in Sec. 3.8 and tested to provide a reference positron lifetime bulk, or defect-free, parameter. The second set is tested and compared against the reference parameter to determine the positron lifetime within the defects of each material. These defects are imparted to the material through either the manufacturing process or through cutting the disks from the rods.

The four materials of aluminum, copper, nickel, and lead were chosen as they have been thoroughly studied and have well documented literature values of positron lifetimes, allowing for the lifetimes in the annealed samples to be considered a benchmark. This is a useful feature in determining whether the spectrometer can be used to discern positron lifetimes in annealed and unannealed metals and if each of those lifetimes agree with current literature values.

The positron lifetime within each material depends on several factors. Primarily, the positron lifetime is given as a function of the defect density within the material under study for reasons explained in Sec. 2.4 and 2.5. Other factors which affect the positron lifetime in materials, such as temperature [11, 26], were not considered in this study.

In terms of theoretical calculations, two main simulation models exist to determine the bulk and defect positron lifetimes of materials. The atomic superposition (AT-SUP) approximation method uses non self-consistent unrelaxed electronic densities while the linear-muffin-tin-orbital (LMTO) approximation method with the atomic sphere approximation (ASA) uses self-consistent electronic densities. Each method is alleged to give good values of positron lifetimes in metals and semiconductors [39, 43].

### 3.7.1 Aluminum

Two aluminum samples are used in this experiment. The first is an aluminum foil of thickness 0.5 mm with a purity of 99.9%. The second sample is an aluminum rod with diameter 22 mm. For source-based experiments, sections of this rod are cut to thicknesses of  $\sim$ 1 mm. The purity of the sample from the aluminum rod is given as 99.9997%.

Theoretical calculations show positron lifetimes in the aluminum being found to have values of 168 ps and 160 ps using the AT-SUP method and 165 ps and 153 ps with the LMTO-ASA method in bulk materials. Additional theoretical calculations were done assuming monovacancies in the material, with the AT-SUP method reporting values of 244 ps and 231 ps in aluminum while the LMTO-ASA method calculates values of 250 ps and 237 ps [39]. Experimentally, values for positron lifetimes in bulk aluminum are reported as 165 ps [39] and 163 ps [42], while values in monovacancies are reported as 244 ps [39, 42].

### 3.7.2 Nickel

Samples of nickel foil, having thicknesses of 0.1 mm and a purity of 99.994%, were obtained for source-based experiments. The theoretical calculations report positron lifetimes in nickel of 96 ps and 108 ps using the AT-SUP method and 96 ps and 108 ps with the LMTO-ASA method in bulk materials. Additional theoretical calculations were done assuming monovacancies in the material, with the AT-SUP method reporting values of 166 ps and 177 ps in nickel while the LMTO-ASA method calculates values of 169 ps and 182 ps [39]. Experimental values for positron lifetimes in bulk nickel are cited as 109 ps [39] and 110 ps [42], while values in monovacancies are reported as 180 ps [39].

### 3.7.3 Copper

Two separate copper samples are tested in the PALS experiments. The first being a simple 0.4 mm thick industrial copper foil of unknown purity. The second copper sample used in source-based PALS experiments consist of disks of diameter 19 mm and thickness  $\sim$ 1 mm cut from a rod of length 250 mm. The purity of this copper sample is given as 99.999%.

Theoretical calculations exist which vary from simulation model to model, with positron lifetimes in the metal being found to have values of 108 ps and 130 ps using the AT-SUP method and 105 ps and 118 ps with the LMTO-ASA method in bulk materials. Additional theoretical calculations were done assuming monovacancies in the material, with the AT-SUP method reporting values of 169 ps and 200 ps in copper while the LMTO-ASA method calculates values of 178 ps and 194 ps [39].

Experimental values vary from experiment to experiment, each depending on spectrometer resolution and the degree of severity of defects within the material. Values for positron lifetimes in bulk copper are reported as 120 ps [39] and 100 ps [42], while values in monovacancies are reported as 180 ps [39] and 173 ps [42].

### 3.7.4 Lead

The lead sample used in this experiment is a 0.55 mm thick, 99.9999% pure lead foil used in source-based experiments. Theoretical calculations exist which vary from simulation model to model, with positron lifetimes in lead being found to have values of 190 ps and 214 ps using the AT-SUP method and 188 ps and 197 ps with the LMTO-ASA method in bulk materials. Additional theoretical calculations were done assuming monovacancies in the material, with the AT-SUP method reporting values of 277 ps and 329 ps in lead while the LMTO-ASA method calculates values of 293 ps and 324 ps [39]. Experimental values vary from experiment to experiment, each depending on spectrometer resolution and the degree of severity of defects within the material. Values for positron lifetimes in bulk lead are reported as 204 ps [39] and 194 ps [42], while values in monovacancies are reported as 294 ps [39]. It should be noted that lead is a self-annealing material, meaning that the atomic lattice structures automatically anneal themselves over time. Thus the bulk positron lifetime values are used for this PALS study.

### 3.7.5 Summary of Positron Lifetimes in Materials

The experimental and theoretically derived literature values for the bulk and defect positron lifetimes within materials are given in each section above and are summarized in Table 3.1.

TABLE 3.1: Theoretical and experimental positron lifetimes in picoseconds of materials under study.

Metal	Z	Theoretical								Experimental			
		Bulk				Defect				Bulk		Defect	
		AT-SUP		LMTO-ASA		AT-SUP		LMTO-ASA					
Al	13	168	160	165	153	244	231	250	237	165	163	244	244
Ni	28	96	108	96	108	166	177	169	182	109	110	180	
Cu	29	108	130	105	118	169	200	178	194	120	100	180	173
Pb	82	190	214	188	197	277	329	293	324	204	194	294	

### 3.8 Annealing of Materials

Each of the materials, except for lead, are annealed at a temperature of 75% of their melting point in degrees Celsius in order to remove vacancy and dislocation sites within the atomic lattices of each sample. Lead is exempted from this procedure as lead is self-annealing, meaning that it can recrystallize into its original lattice structure at room temperature. The melting point and chosen annealing temperature of each material is given in Table 3.2.

TABLE 3.2: Melting and annealing points of materials under study

Material	Melting Point (°C)	Annealing Temp (°C)
Al	660.32	495
Ni	1453	1090
Cu	1084.62	813

Starting from an ambient temperature of 25°C, each material is individually placed into an open ceramic vessel which is in turn placed into a furnace. The interior temperature of the furnace is raised at a rate of 100°C per hour until the desired annealing point is reached. The temperature is then held constant for two hours until the unit is turned off and the material allowed to naturally cool. The annealing profile of each material is given in Fig. 3.14.

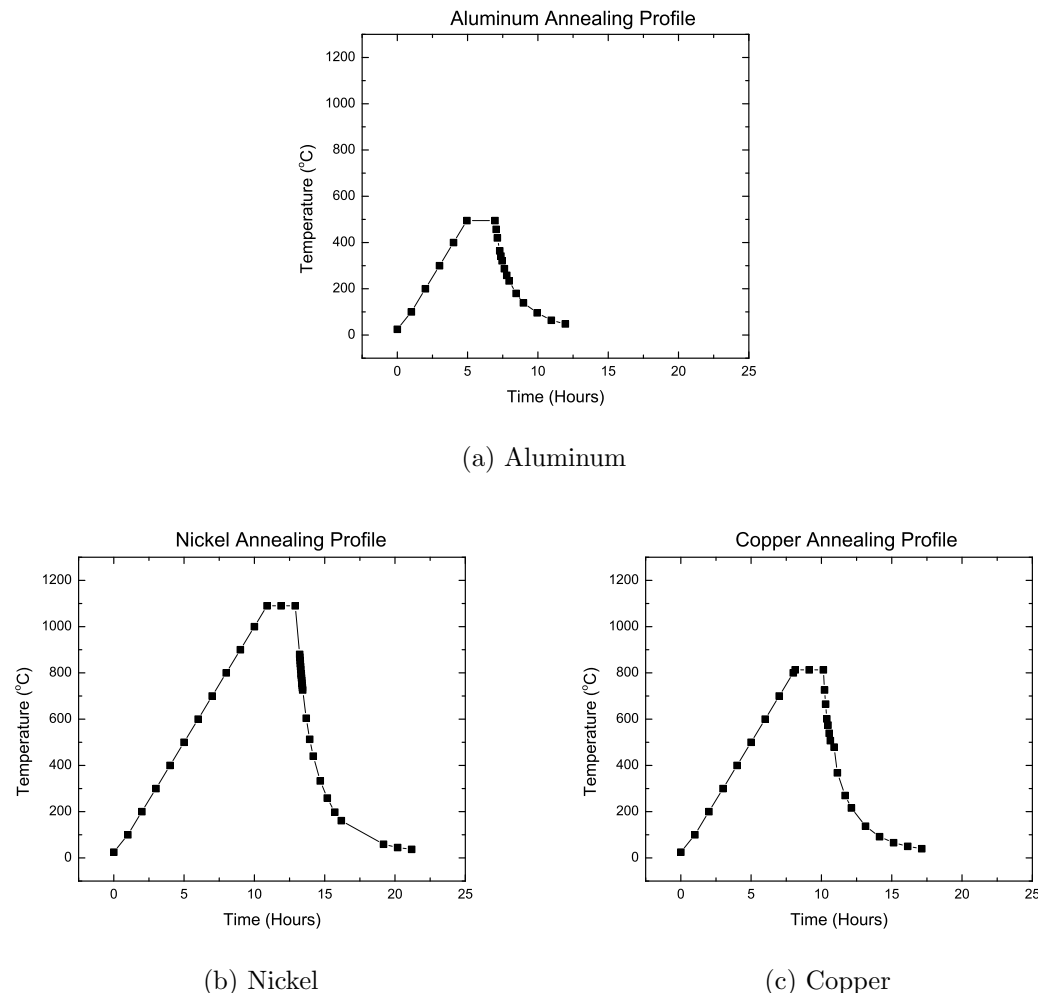


**Figure 3.14:** The annealing profile for (a) aluminum, (b) nickel, and (c) copper materials used in PALS experiments

---

CHAPTER  
**FOUR**

---

## DATA ANALYSIS AND RESULTS

### 4.1 The LT10 Software Package

Data analysis is completed using the Kansy LT10 software. The software is considered to be a mature software package and has been used in a variety of studies. The LT10 software is used to determine the FWHM of the timing response function, or “prompt” resolution function, of the spectrometer when using a  $^{22}\text{Na}$  source, to determine the positron lifetimes in annealed and unannealed materials, and to determine the trapping rate of positrons within unannealed materials.

The LT10 software is capable of performing positron lifetime data analysis with multiple spectra. For the purposes of this study, the project file refers to the overall collection of documents in a single file. Each document has a single fitting routine, such as multiexponential or various trapping states (see Secs. 2.4.3 and 2.5.1), and can contain a single or multiple spectra of either the same or differing materials. Within each document, the spectra are assigned a number of user-defined parameters to represent the different exponential curves convoluted within the overall lifetime spectra. In this study, for example, three parameters are used to describe the contributions to the lifetime spectra from para-positronium, the Kapton tape, and the experimental background. As the materials were tested using the same  $^{22}\text{Na}$  positron emitter and the experimental setup was unchanged from trial to trial, these three parameters can be considered *common* among the various spectra collected for each material under study. However, since this study tests a variety of materials, the parameter describing the positron lifetime within each material is considered a *local* parameter. The

terms *free* and *fixed* denote whether the LT10 software is capable of freely determining the best value for the parameter during the fitting routines or if to accept the user-defined parameter as a fixed parameter and use the user-defined parameter as is during the fitting routine. The software also has the ability to set a parameter as *partially common*, in which multiple, but not all, spectra within a document share a parameter together. An example of usage would be if the same material were tested twice and it was desired to find a common parameter to describe both materials. As a final note, the software requires initial values in units of nanoseconds in order to perform lifetime fits. More on this aspect is given in Sec. 4.3.

Initially, the spectrum of the  $^{22}\text{Na}$  source is loaded as a multiexponential fit into a new document within the project file. Three sample components are used to represent the positron lifetime contributions from para-positronium, the Kapton tape, and the background. Initial values are given as a *local fixed* value of 0.124 ns, a *local free* value of 0.37 ns, and a *local free* value of 1.4 ns, respectively. The FWHM of the prompt resolution function is set as a single Gaussian with an initial *local free* parameter of the optimal timing resolution found using the procedures outlined in Sec. 3.4.

After fitting this document, a second document is created within the project file using a multiexponential fit to represent the reference materials. These reference materials are the timing spectra collected from the annealed materials. Within this document, a single *local free* parameter is attributed to each sample to represent the bulk parameter of the positron lifetime within each material. The three values representing the lifetime contributions from positronium, the Kapton tape, and the background are copied from the  $^{22}\text{Na}$  document and are set as *common fixed* parameters within the source contribution for each reference material. Again, the prompt resolution function is set as a single Gaussian, but now uses the value obtained from the results of the fit to the  $^{22}\text{Na}$  data and is set as *common fixed*. The source parameter intensities are copied from the  $^{22}\text{Na}$  document and are set as *common free* for each reference material. The fit is performed, giving the positron lifetimes in the bulk materials and the intensities of the para-positronium, Kapton tape, and background lifetime parameters.

A third document is created within the project file, now using a two-state trapping model, to determine the positron lifetime within the unannealed materials, as well as giving an indication of the trapping rate within each material (see Sec. 2.4.3). Each of the spectra of the unannealed or damaged samples are loaded into the document.

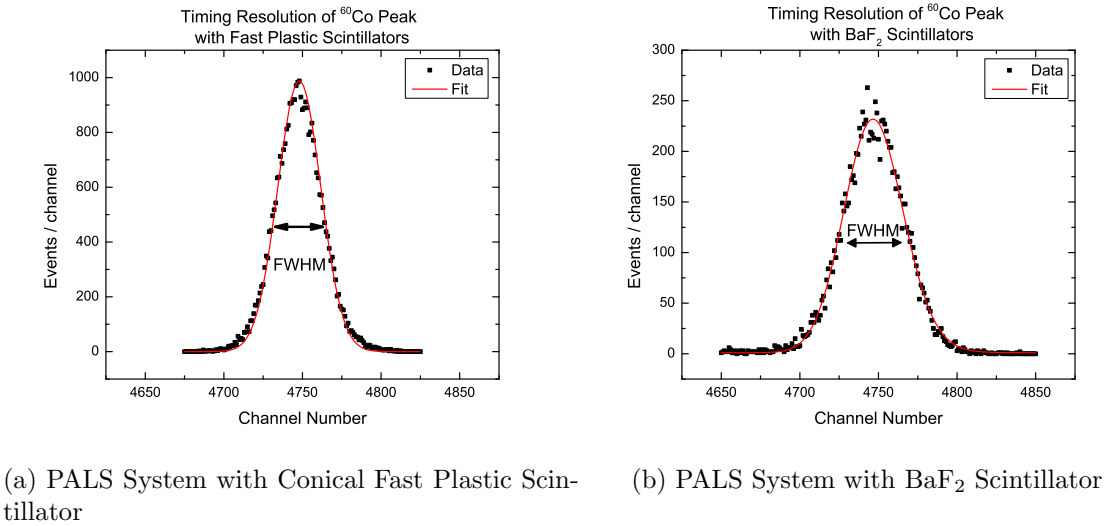
Any trials which have a common base material, such as two copper samples run to different total counts, or two nickel samples with varying degrees or types of damage, are set as *partially common* values in regards to  $\tau_{free}$ , the positron lifetime within the bulk material. The remainder of the bulk values are set as *local fixed* values copied from the previous document for the respective materials. Since lead is a self-annealing material, the positron lifetime of the defect,  $\tau_D$ , is fixed at the literature value of 0.294 ns and the trapping rate,  $\kappa_D$ , is fixed at zero. The initial parameter values for  $\tau_D$  of each material are set as *local free* and specified as the literature experimental value provided in Table 3.1. The trapping rate is arbitrarily set to an initial value of 10 and set as a *local free* parameter. The source contribution lifetimes and their intensities are copied in the same fashion as before from the document containing the spectra of the annealed materials, with the source contribution lifetimes set as *common fixed* and their respective intensities set as *common free*. The FWHM is again set as a single Gaussian, copied from the  $^{22}\text{Na}$  source document, and is set as *common fixed*. The fit of the third document is then performed, providing the monovacancy lifetimes and trapping rates of each material.

These parametrization features of the software can be exploited as the experiments are conducted by only changing the material under study, thus leaving any other contributions to the lifetime spectrum constant from trial to trial. For the experiments performed in this study, it is found to be best to fit the foils and the disks as projects as they are samples from different manufacturing processes with slightly different properties.

## 4.2 Prompt $^{60}\text{Co}$ Gamma Distribution

Using the procedures in Sec. 3.4, the photomultiplier tubes and electronic analysis circuitry are tested with both the  $\text{BaF}_2$  and fast plastic scintillators with their respective appropriate optical grease. The optimal timing resolution of the system is found using a two hour data run with a  $10\ \mu\text{Ci}$   $^{60}\text{Co}$  source.

Using the Gaussian fitting routines within the MPA-NT software, the FWHM of the peak using the  $\text{BaF}_2$  scintillator is  $43.98 \pm 0.37$  channels, corresponding to a prompt timing resolution of  $213.34 \pm 1.79$  ps using the calibration of 4.85 ps/channel found using the procedures described in Sec. 3.3.4. Using the fast plastic scintillator, the FWHM of the peak is  $35.09 \pm 0.15$  channels, corresponding to a prompt timing



(a) PALS System with Conical Fast Plastic Scintillator      (b) PALS System with  $\text{BaF}_2$  Scintillator

**Figure 4.1:** Prompt  $^{60}\text{Co}$  resolution curves for the PALS system with (a) conical fast plastic and (b)  $\text{BaF}_2$  scintillators. The timing resolution with the conical fast plastic scintillator is found to be  $170.17 \pm 0.73$  ps and the timing resolution with the  $\text{BaF}_2$  scintillator is found to be  $213.34 \pm 1.79$  ps. These were fit as a single Gaussian with the background fit provided by the MPA-NT software.

resolution of  $170.17 \pm 0.73$  ps using the calibration of 4.85 ps/channel.

## 4.3 Radionuclide Source

### 4.3.1 Fast Plastic Scintillator

#### $^{22}\text{Na}$ Background

The proper analysis of the spectra taken with only  $^{22}\text{Na}$  is important as it gives information regarding the positron lifetime in Kapton, the background, and the prompt resolution of the system. As mentioned in Sec. 4.1, initial values must be given to the LT10 software in order to perform fits.

Recalling from Sec. 2.4.4, the para- and ortho-positronium states contribute to the overall positron energy spectrum recorded by the multichannel analyzer. Given that the two-gamma decay is forbidden from occurrence for the ortho-positronium state and assuming positron annihilation occurs at or near rest, the o-Ps state decays into three gammas of energies less than 511 keV. In terms of detection by either the

fast plastic or BaF<sub>2</sub> scintillators, the energy signatures from these three gammas are smeared across the lower end of the energy spectra as a result of the poor resolution of PMTs in comparison to HPGe detectors, having neither well-defined Compton edges nor photopeaks. For the purposes of this study, the o-Ps state is ignored in data analysis. Instead, attention is turned towards the para-positronium state. With its 124 ps characteristic lifetime, the p-Ps annihilation lifetime is within the detection capabilities of the spectrometer and included as a fixed parameter within data analysis software.

The Kapton tape used to support the <sup>22</sup>Na source has been cited as having a single positron lifetime, but recent studies have indicated it may have multiple positron lifetime components. Multiple studies have been conducted into the determination of the positron lifetime and respective intensities within Kapton tape. It has been reported as having two lifetime components of  $\tau_1 = 152 \pm 1$  ps and  $\tau_2 = 371 \pm 1$  ps by one group[19], while having lifetimes of  $\tau_1 = 229$  ps ( $I_1 = 12.0\%$ ) and  $\tau_2 = 378$  ps ( $I_2 = 87.4\%$ ) [9], as well as  $\tau_1 = 127$  ps ( $I_1 = 31.0\%$ ) and  $\tau_2 = 335$  ps ( $I_2 = 64.5\%$ ) [10]. From this, it is seen that the lifetime components of Kapton are still in dispute. Attempts were made by this study to separate the two Kapton lifetimes, but better results were found when treating the positron lifetime in Kapton as a single entity. Additional studies into the positron lifetime in Kapton may be made with this spectrometer in the future.

The positron lifetime fits are performed using an initial prompt resolution of 170 ps, taken from Sec. 4.2. The contribution from para-positronium is taken to be 124 ps. Using the information above, it is noted that each of the previous studies into the positron lifetime in Kapton, there exists a lifetime component of approximately 370 ps with a much greater intensity than those of a faster lifetime component. Thus the contribution of the Kapton tape to the total lifetime spectrum is described with a single value, initially set to 370 ps, rather than two separate lifetimes. Finally, an initial value of 1.4 ns is used to describe contributions to the lifetime spectrum from background sources such as positron annihilation in air, as well as within the aluminum foil and electrical tape used to cover the detector package.

Two background data collections were completed with the <sup>22</sup>Na source without the presence of a sample. In the first trial, in which the data collected is used with the foil samples, the prompt resolution is found to have a value of  $223.7 \pm 0.3$  ps. This value is  $\sim 25\%$  greater than the  $170.172 \pm 0.73$  ps prompt resolution reported with the <sup>60</sup>Co

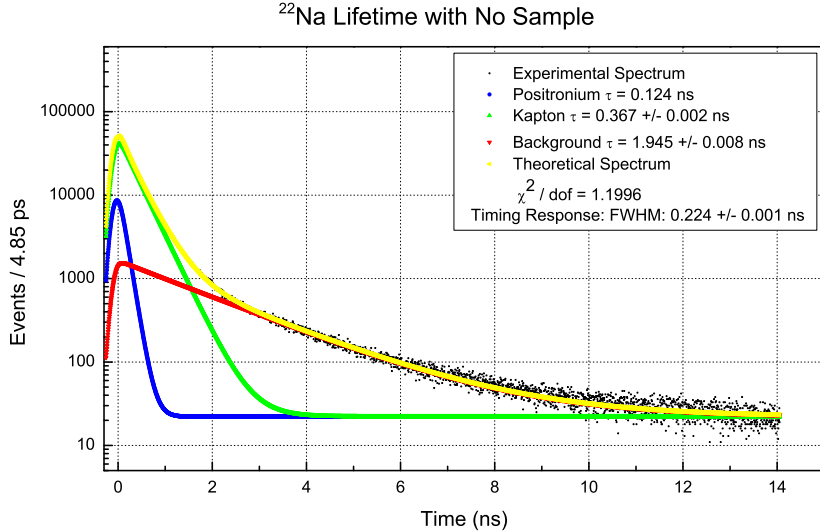


**Figure 4.2:** Experimental  $^{22}\text{Na}$  lifetime data with no sample used with thin foil experiments.

source, likely due to the larger difference between triggering energies within the  $^{22}\text{Na}$  positron emitter as opposed to the  $^{60}\text{Co}$ , which releases near-coincidence gammas with energies very close to one another. It is however consistent with previous studies [1, 41, 45]. The lifetime component of the p-Ps state is fixed at 124 ps and found to have an intensity of 9.38%, the lifetime component of the Kapton tape is found to be  $367.6 \pm 2.2$  ps with an intensity of  $79.63 \pm 1.28\%$ , and the lifetime component of the background is found to be  $1.95 \pm 0.01$  ns with an intensity of  $10.99 \pm 1.10\%$ . The reduced  $\chi^2$ , or  $\chi^2$  per degree of freedom (DOF) is found to be 1.20 with statistics of 6.36 million coincidence events over a data collection period of 12 hours.

In the second trial, in which the data collected is used with the disk samples, the prompt resolution is found to have a value of  $229.5 \pm 0.5$  ps. The lifetime component of the p-Ps state is fixed at 124 ps and found to have an intensity of 9.09%. The lifetime component of the Kapton tape is found to be  $373.3 \pm 0.7$  ps and to have an intensity of  $79.88 \pm 0.64\%$ . The lifetime component of the background is found to be  $2.04 \pm 0.001$  ns with an intensity of  $11.03 \pm 0.39\%$ . The  $\chi^2/\text{DOF}$  is found to be 1.32 with statistics of 9.83 million coincidence events over a collection period of 24 hours.

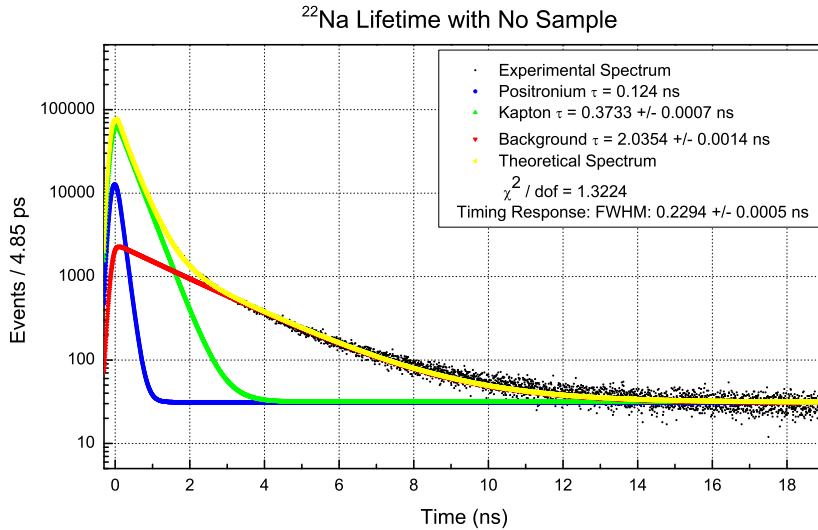


**Figure 4.3:** Experimental  $^{22}\text{Na}$  lifetime data with no sample used with  $\sim 1$  mm thick disk experiments.

## Aluminum

Using the same settings as with the  $^{22}\text{Na}$  background trial, the source contributions from para-positronium, Kapton tape, the background and the prompt resolution are kept as common fixed parameters with the background trial and other materials, leaving the positron lifetimes in the annealed and unannealed aluminum foil samples to be freely determined by the LT10 software.

The bulk parameter of the positron lifetime of the 0.5 mm thick, 99.9% pure aluminum foil is found to be  $164.9 \pm 0.1$  ps with 4.39 million coincidence events over a period of 12 hours. The  $\chi^2/\text{DOF}$  for this data trial is found to be 1.53. The defect parameter of the positron lifetime is found to be  $234.1 \pm 0.8$  ps with a trapping rate of  $5.75 \pm 0.07 \text{ ns}^{-1}$ , having a  $\chi^2/\text{DOF}$  of 1.45 with statistics of 5.51 million coincidence events over a data collection period of 12 hours.

An additional trial was run with an aluminum disk with a thickness of  $\sim 1$  mm and a purity of 99.9997%. The bulk parameter of the positron lifetime in this aluminum disk is found to be  $160.3 \pm 0.1$  ps with a  $\chi^2/\text{DOF}$  of 1.97 with statistics of 8.98 million coincidence events. The defect parameter of the positron lifetime is found to be  $216.7 \pm 0.5$  ps with a trapping rate of  $4.88 \pm 0.05 \text{ ns}^{-1}$ , having a  $\chi^2/\text{DOF}$  of 1.69 with statistics of 9.40 million coincidence events over a data collection period of 24

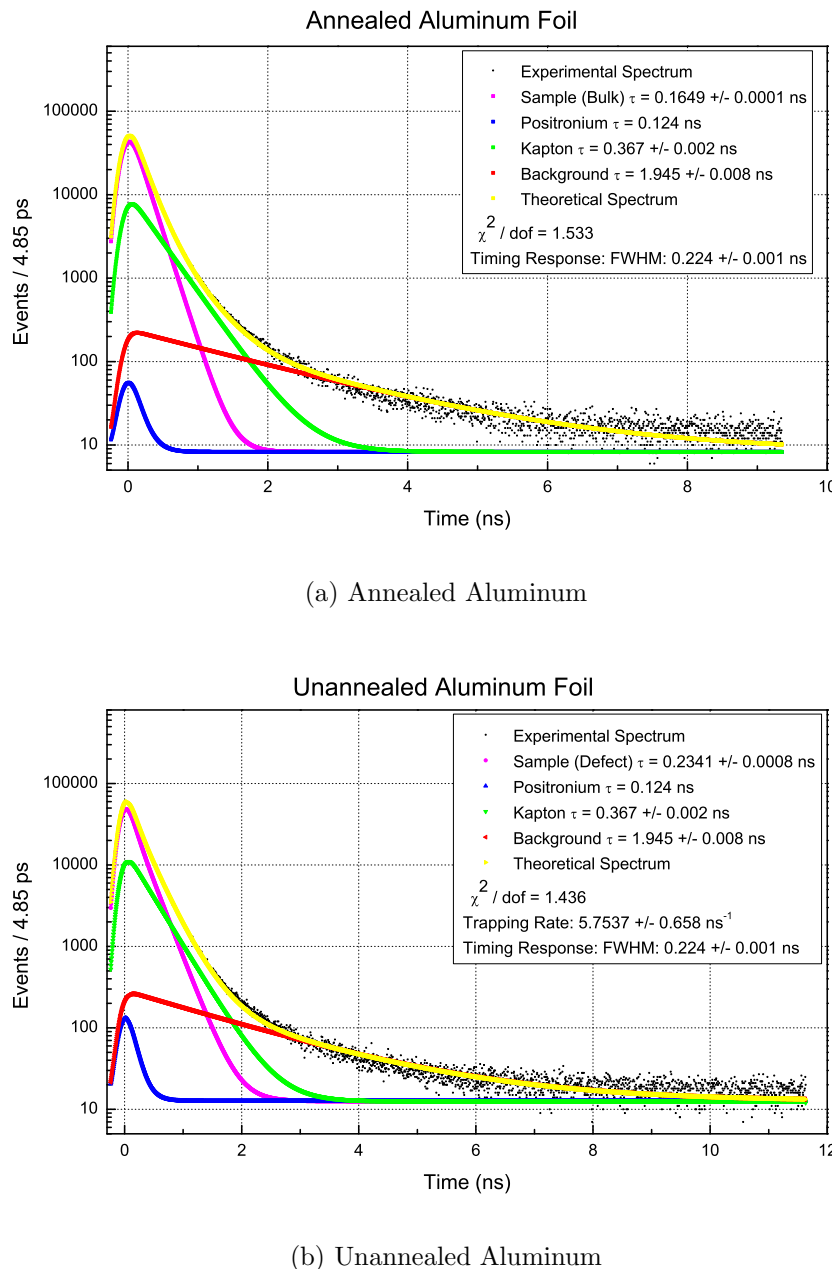


**Figure 4.4:** Experimental results of (a) annealed and (b) unannealed aluminum foils using  $^{22}\text{Na}$  source.

hours.

### Nickel

The source contribution lifetimes from para-positronium, Kapton tape, and the background, as well as the prompt resolution, as determined by the  $^{22}\text{Na}$  background trial are copied and kept as *common fixed* parameters. The positron lifetimes in the annealed and unannealed nickel foil samples are freely determined by the LT10 software.

The bulk parameter of the positron lifetime of the 0.1 mm thick, 99.9994% pure nickel foil is found to be  $106.8 \pm 0.2$  ps with 5.46 million coincidence events over a data collection period of 12 hours. The  $\chi^2/\text{DOF}$  for this data run is found to be 1.80. Two separate measurements were taken with the nickel foil. The first measurement was taken with a previously unannealed sample. A second sample of nickel was accidentally oxidized during its annealing process. Out of curiosity, data was collected using this oxidized annealed sample. Using the bulk parameter of the annealed nickel, the defect parameter of the positron lifetime in the oxidized nickel foil is found to be  $125.4 \pm 0.5$  ps with a trapping rate of  $22.27 \pm 1.86 \text{ ns}^{-1}$ , having a  $\chi^2/\text{DOF}$  of 1.33 with statistics of 5.50 million coincidence events over a data collection period of 12 hours. The sample was then re-annealed to remove the oxidation and again tested. The defect parameter of the positron lifetime is found to be  $154.3 \pm 0.3$  ps with a trapping rate of  $46.13 \pm 2.26 \text{ ns}^{-1}$ , having a  $\chi^2/\text{DOF}$  of 1.45 with statistics of 6.13 million coincidence events in a period of 12 hours.

### Copper

The source contributions from para-positronium, Kapton tape, the background, as well as FWHM of the prompt resolution, are kept as *common fixed* parameters from the background trial in Fig. 4.2. This allowed for the positron lifetime in the copper foil sample to be freely determined by the LT10 software as a *local free* parameter.

As mentioned in Sec. 3.7.3, the copper foils were cut from a roll of stock copper foil with an unknown purity. Two data collection periods were conducted with the 0.4 mm thick copper foil, one having 5.71 million coincidence events over a period of 12 hours and the other having 10.44 million coincident events over a period of 22 hours. The experimental setup was undisturbed between data collection runs. The bulk parameters were set as *partially common* since the material and experimental configuration were unchanged and found to have positron lifetimes of  $121.8 \pm 14.0$

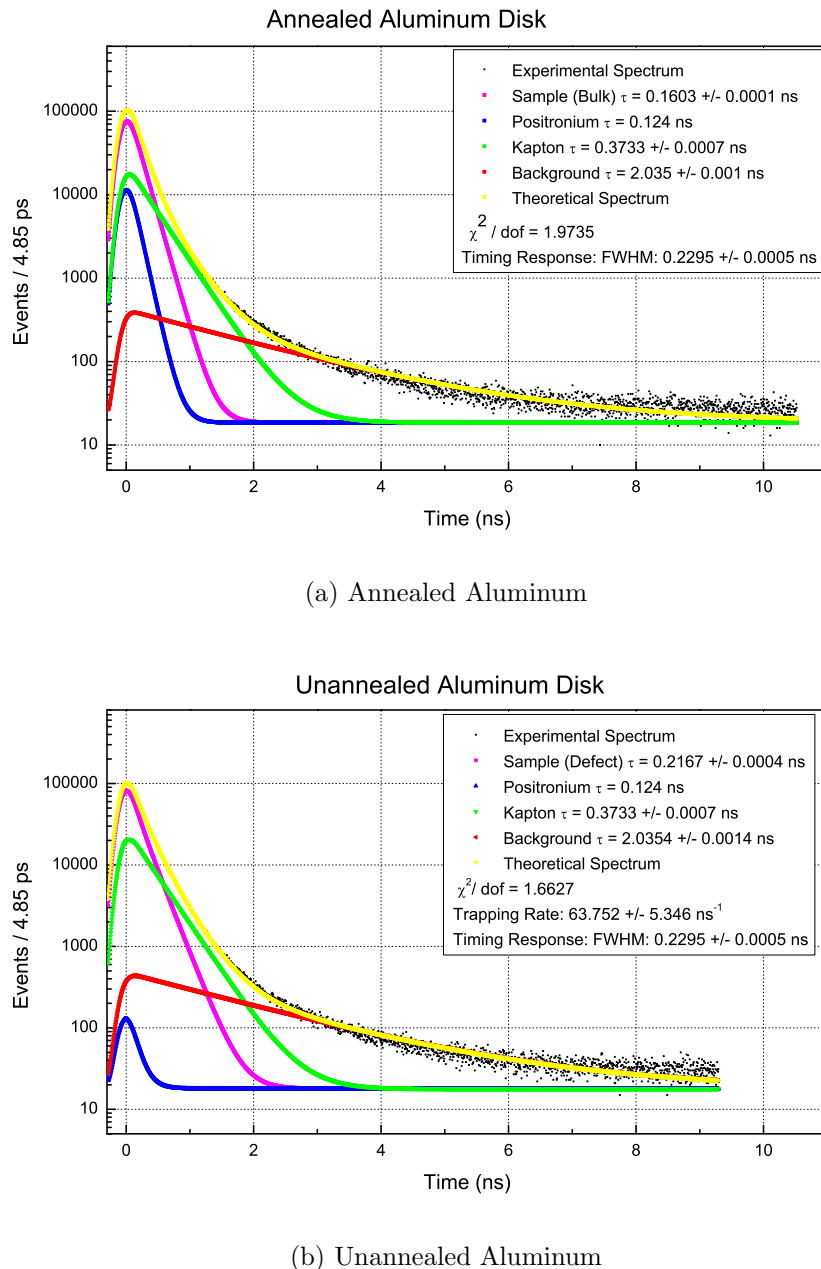


**Figure 4.5:** Experimental results of (a) annealed and (b) unannealed aluminum disks using  $^{22}\text{Na}$  source.

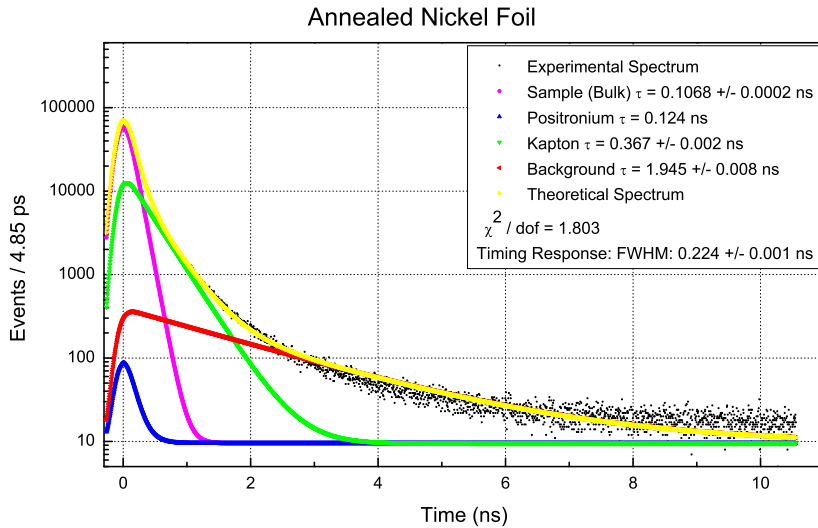


**Figure 4.6:** Experimental results of annealed nickel foils using  $^{22}\text{Na}$  source. This material is the same sample that was accidentally oxidized in Fig. 4.7b, tested, and annealed again to remove the oxidation.

ps with a  $\chi^2/\text{DOF}$  of 2.59 for the first data run and 2.81 for the second data run. The defect parameter of the positron lifetime is found to be  $179.1 \pm 0.2 \text{ ps}$  with a trapping rate of  $6.67 \pm 4.1 \text{ ns}^{-1}$ , having a  $\chi^2/\text{DOF}$  of 1.49 for the first data run and 1.96 for the second, with statistics of 5.67 over a 12 hours period and 10.39 million coincidence events over a period of 22 hours, respectively.

An additional trial was run with a copper disk of thickness  $\sim 1 \text{ mm}$  and a purity of 99.9997%. The bulk parameter of the positron lifetime of this copper disk is found to be  $120.6 \pm 0.1 \text{ ps}$  with 8.39 million coincidence events over a data collection period of 24 hours. The  $\chi^2/\text{DOF}$  for this data run is 1.97. The defect parameter of the positron lifetime is found to be  $167.6 \pm 0.2 \text{ ps}$  with a trapping rate of  $63.75 \pm 5.36 \text{ ns}^{-1}$ , having a  $\chi^2/\text{DOF}$  of 1.66 with statistics of 8.86 million coincidence events over a period of 24 hours.

## Lead

Using the same settings as with the  $^{22}\text{Na}$  background trial, the source contributions from para-positronium, Kapton tape, the background, as well as the FWHM of the prompt resolution, are kept as common parameters from the  $^{22}\text{Na}$  background trial,

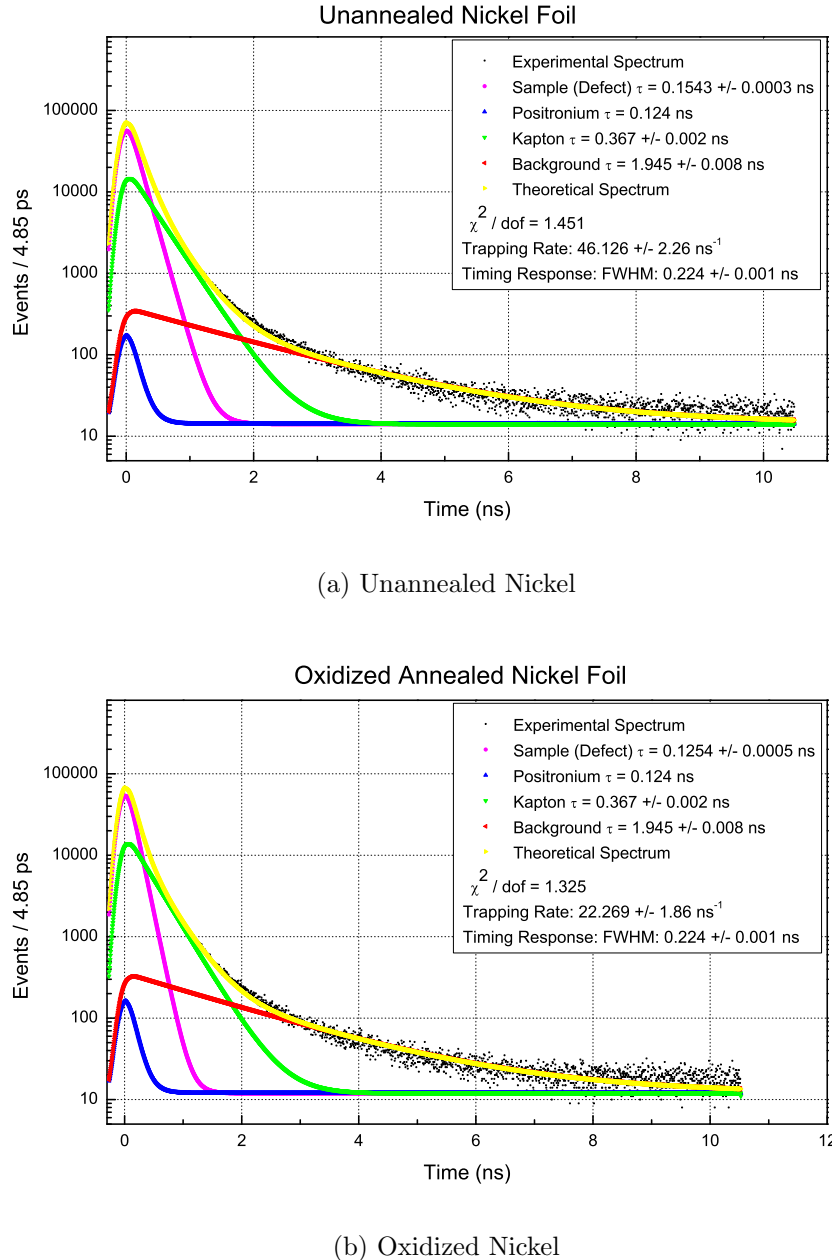


**Figure 4.7:** Experimental results of (a) unannealed, and (b) oxidized nickel foils using  $^{22}\text{Na}$  source. Both samples of nickel are reported to have a purity of 99.9994%. However, the material history is unknown. The second sample shown in Fig. 4.7b was accidentally oxidized during the annealing process.

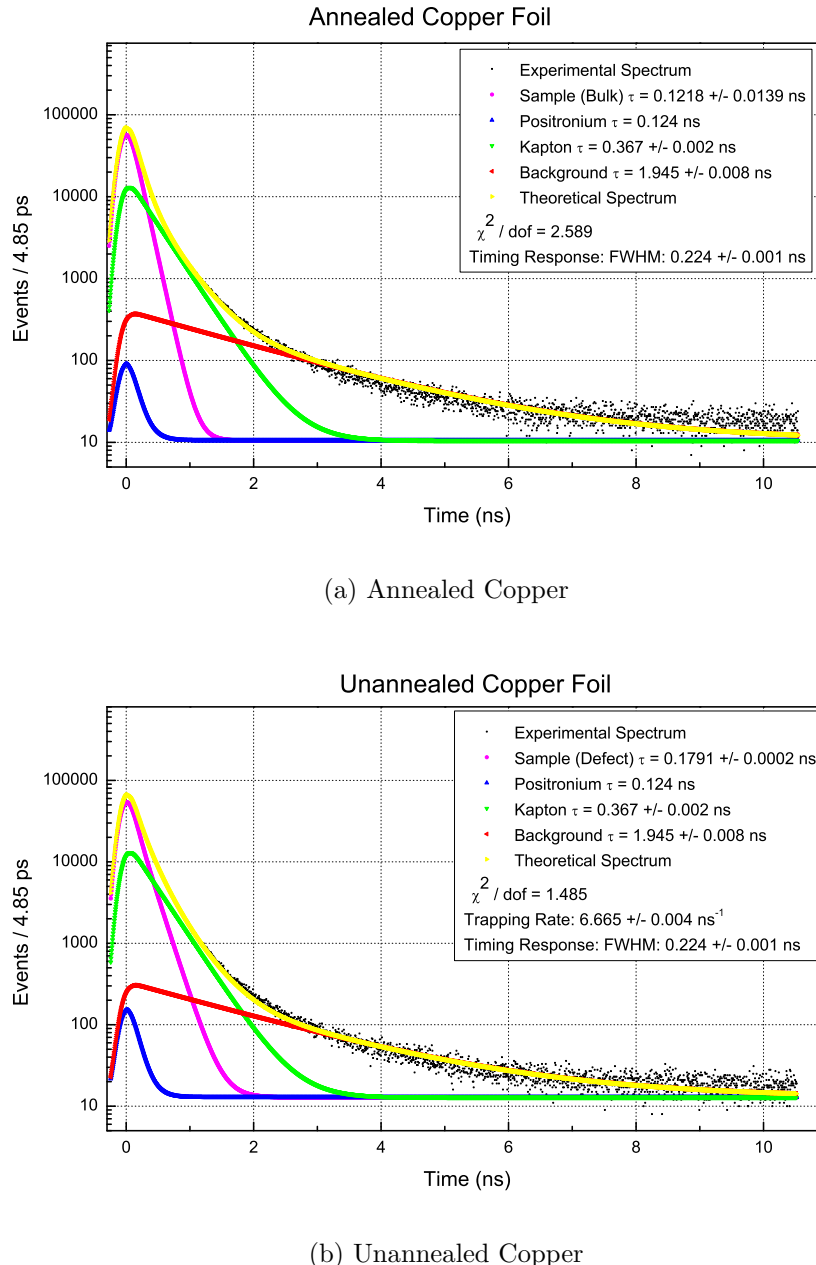


**Figure 4.8:** Experimental results of (a) annealed and (b) unannealed copper foils using  $^{22}\text{Na}$  source. The copper foils used in this study have an unknown material purity. The discrepancy in the theoretical to experimental data fits of the annealed copper may be the result of an additional lifetime component not accounted for in the data analysis. The disagreement is very slight and likely does not affect the reduced  $\chi^2$ .

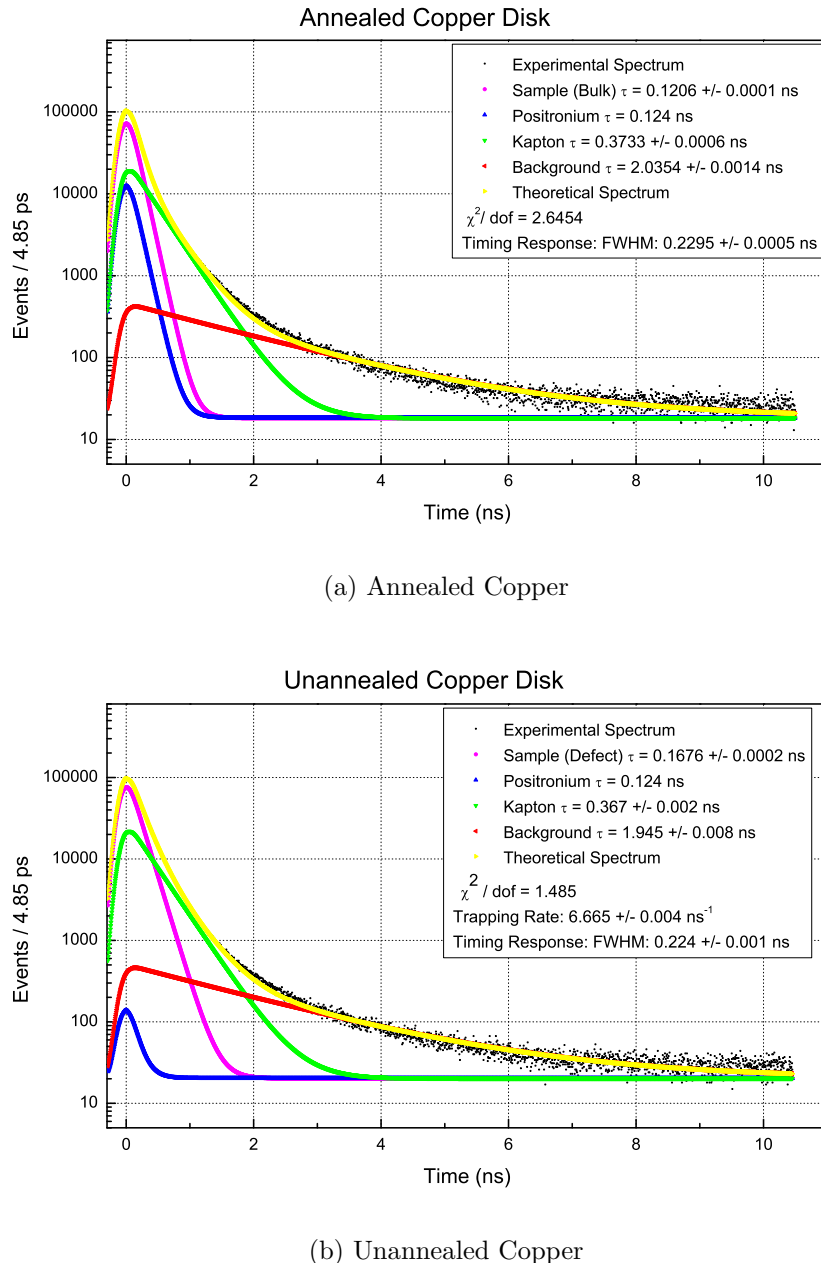


**Figure 4.9:** Experimental results of (a) annealed and (b) unannealed copper disks using  $^{22}\text{Na}$  source.

leaving the positron lifetime in the lead sample to be freely determined by the LT10 software.

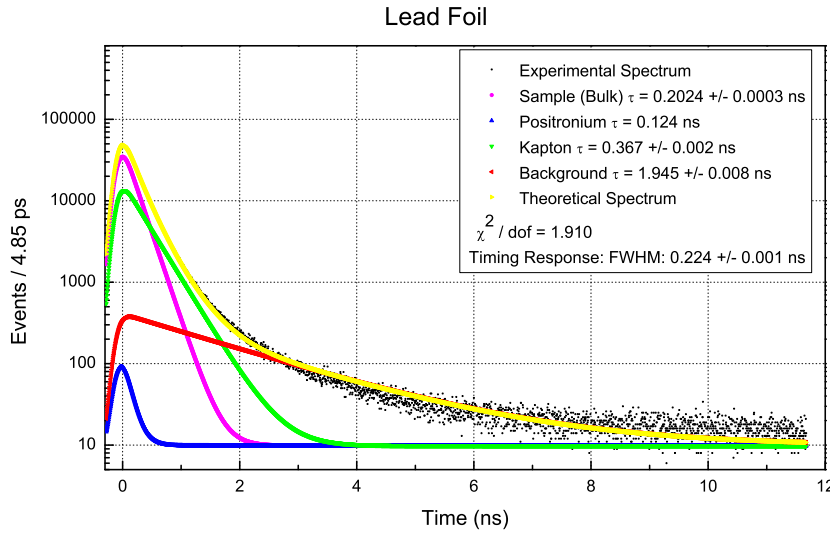


**Figure 4.10:** Source-based lifetime data with lead foil sample

The bulk parameter of the positron lifetime of the 0.55 mm thick, 99.9999% pure lead foil is found to be  $202.5 \pm 0.4$  ps with 4.76 million coincidence events and a  $\chi^2/\text{DOF}$  of 1.91. The data was collected over a period of 12 hours.

## 4.4 Summary of Results

The tables in this section include a summary of the positron lifetimes within materials as determined by this study. Table 4.1 gives a summary of the positron lifetimes and their respective intensities of the Kapton tape and the background as recorded by the spectrometer. Table 4.2 and 4.3 give the positron lifetimes in the various foils and disks used in the study, respectively. Finally, Table 4.4 gives information regarding data collection rates for each experiment conducted in this study.

TABLE 4.1: Positron lifetimes and intensities of Kapton tape and background as determined by this study.

Source	Usage	$^{22}\text{Na}$ Characteristics					Statistics	
		$\tau_{\text{p-Ps}}$ ps	$\tau_{\text{Kapton}}$ ps	Int <sub>Kapton</sub> %	$\tau_{\text{Bkgd}}$ ns	Int <sub>Bkgd</sub> %	$\chi^2$ /dof	Events millions
$^{22}\text{Na}$	Foils	124	$367.6 \pm 2.2$	$79.63 \pm 1.28$	$1.95 \pm 0.01$	$10.99 \pm 1.10$	1.20	6.36
$^{22}\text{Na}$	Disks	124	$373.3 \pm 0.7$	$79.88 \pm 0.64$	$2.04 \pm 0.001$	$11.03 \pm 0.39$	1.32	9.83

TABLE 4.2: Bulk and defect positron lifetimes in foils as determined by this study. The bulk positron lifetimes refer to the positron lifetimes as found in the annealed materials while the defect positron lifetimes refer to the positron lifetimes as found in the unannealed materials. As the lead is a self-annealing material, no data was collected to find the defect positron lifetimes. The oxidized nickel was oxidized during the process of annealing, resulting in a defect positron lifetime near the bulk lifetime literature value. No history of either nickel materials is known.

Metal	Z	Bulk (ps)	Defect (ps)	Trapping Rate (ns <sup>-1</sup> )	$\chi^2$ /dof	Statistics (millions)
Aluminum	13	$164.9 \pm 0.1$	$234.1 \pm 0.8$	$5.57 \pm 0.07$	1.44	5.51
Nickel	28	$106.8 \pm 0.2$	$154.3 \pm 0.3$	$46.13 \pm 2.26$	1.45	6.13
Oxidized Nickel	28	$106.8 \pm 0.2$	$125.4 \pm 0.5$	$22.27 \pm 1.86$	1.33	5.50
Copper	29	$121.8 \pm 14.0$	$179.1 \pm 0.2$	$6.67 \pm 4.10$	1.48	5.67
Lead	82	$202.5 \pm 0.4$	-	-	1.91	4.76

TABLE 4.3: Bulk and defect positron lifetimes in disks as determined by this study. The bulk positron lifetimes are in excellent agreement with accepted literature values.

Metal	Z	Bulk (ps)	Defect (ps)	Trapping Rate (ns <sup>-1</sup> )	$\chi^2$ /dof	Statistics (millions)
Aluminum	13	$160.3 \pm 0.1$	$216.7 \pm 0.5$	$4.88 \pm 0.46$	1.69	9.40
Copper	29	$120.6 \pm 0.1$	$167.6 \pm 0.2$	$63.75 \pm 5.36$	1.66	8.86

TABLE 4.4: Statistical and rate information for data collection

Material	Z	Properties	Type	Statistics (millions)	Duration (hours)	Average Coinc Rate (Hz)
$^{22}\text{Na}$		Source	Foil	6.36	12	149.23
Aluminum	13	Annealed	Foil	4.47	12	103.43
Nickel	28	Annealed	Foil	5.55	12	128.37
Copper	29	Annealed	Foil	5.71	12	132.22
Copper	29	Annealed	Foil	10.45	22	131.92
Lead	82		Foil	4.83	12	111.88
Aluminum	13	Unannealed	Foil	5.60	12	129.52
Nickel	28	Unannealed	Foil	6.22	12	144.01
Nickel	28	Oxidized	Foil	5.58	12	129.17
Copper	29	Unannealed	Foil	5.76	12	133.41
Copper	29	Unannealed	Foil	10.54	22	133.15
$^{22}\text{Na}$		Source	Disk	9.83	24	114.90
Aluminum	13	Annealed	Disk	9.12	24	105.51
Copper	29	Annealed	Disk	8.53	24	98.67
Aluminum	13	Unannealed	Disk	9.55	24	110.49
Copper	29	Unannealed	Disk	9.00	24	104.17

---

CHAPTER  
**FIVE**

---

## DISCUSSION AND CONCLUSION

### 5.1 Discussion of Results

#### 5.1.1 Fast Plastic Scintillators

The bulk positron lifetimes as found in the source-based trials of the thin foils and disks using fast plastic scintillators are in very good agreement with previously published literature values as shown in Table 5.1. This is a good indication that the spectrometer is capable of determining the difference between positron lifetimes in annealed and unannealed materials.

TABLE 5.1: Comparison of current literature positron lifetimes to experimentally determined values in picoseconds of materials under study.

Metal	Z	Type	Exp. Literature		Experimental	
			Bulk	Defect	Bulk	Defect
			(ps)	(ps)	(ps)	(ps)
Aluminum	13	Foil	165	244	$164.9 \pm 0.1$	$234.1 \pm 0.8$
Nickel	28	Foil	109	180	$106.8 \pm 0.2$	$154.3 \pm 0.3$
Nickel Oxide	28	Foil	-	-	$106.8 \pm 0.2$	$125.4 \pm 0.5$
Copper	29	Foil	120	180	$121.8 \pm 13.9$	$179.2 \pm 0.2$
Lead	82	Foil	204	294	$202.4 \pm 0.3$	-
Aluminum	13	Disk	165	244	$160.3 \pm 0.1$	$216.7 \pm 0.4$
Copper	29	Disk	120	180	$120.6 \pm 0.1$	$167.6 \pm 0.2$

The bulk lifetimes of the aluminum, nickel, and lead foils, in addition to the aluminum and copper disks, are in excellent agreement with current literature values. Any discrepancies of the bulk lifetimes may be the result of imperfect annealing

techniques which were not taking into consideration in the data analysis. The bulk lifetime of the copper foil likely has a large error due to the fact that the copper foils were not high purity, thus any impurities in the material may be contributing to the lifetime spectra unaccounted. The nickel and nickel oxide are reported to have the same bulk lifetime as the oxidation of the nickel foil is treated as a defect with the material, even though the oxidation of the nickel foil occurred during the process of annealing. Within the data analysis, the unannealed and oxidized nickel foils are treated as having the same bulk lifetime, namely that of the annealed nickel foil. This is due to the unannealed and oxidized annealed nickel foils having the same base material of nickel. The defect lifetimes of all of the foils and disks agree with the general trend of current literature values for monovacancy defect positron lifetimes. As lead is a self-annealing material, the lead foil was not tested for positron lifetimes within the material defects.

The results from the nickel foils indicate that the PALS technique can be used to spectroscopically measure surface damage to a material as a result of oxidation while the results from the trials with the copper foils indicate that the PALS technique may be used with materials which are not of high-purity atomic composition.

The higher values of  $\chi^2/\text{dof}$  as reported in Sec. 4.3 are likely the result of an additional lifetime component with a very long lifetime not taken into consideration in the data analysis. Additional studies would need to be completed to determine if this lifetime is caused by the annihilation of the o-Ps state within the electrical tape coverings of the detectors, or if the additional lifetime component is due to a different, unforeseen mechanism.

Another possible reason for the higher values of  $\chi^2/\text{dof}$  is that due to imperfect annealing techniques, there may be some remaining defect regions within the bulk materials. Following the conclusion of this study, conversations with the lead author of the LT10 software, Dr. Jerzy Kansy, suggest that in order to account for imperfections in the annealing process in the data analysis, the lifetime spectra of the annealed and unannealed materials should be loaded together using the two-state trapping model within the LT10 software. Each material may be initially given *partially common free* parameters of the accepted literature values for  $\tau_D$  and  $\tau_{\text{free}}$ ; these parameters are then simultaneously calculated while allowing for the trapping rate,  $\kappa_D$ , to locally vary. This new method of using the LT10 software may produce better data fits while providing additional information about the intensity of defects

remaining in a sample after it has been annealed to a high percentage of its melting point.

### 5.1.2 BaF<sub>2</sub> Scintillators

Initial studies using the BaF<sub>2</sub> scintillators indicate that despite the decrease in spectrometer resolution using the <sup>60</sup>Co from  $170.17 \pm 0.73$  ps using the fast plastic scintillator to  $213.34 \pm 1.79$  ps using the BaF<sub>2</sub> scintillator, the spectrometer is capable of generating a precision positron lifetime spectrum. Additional studies should be completed to determine the effect of using optical grease capable of the transmission of the “fast” and “slow” components of the BaF<sub>2</sub> scintillation process. Although the “fast” component makes up only 15% of the total light output from the BaF<sub>2</sub> scintillator, this component may prove critical to achieve improved spectrometer timing resolution. The usage of the BaF<sub>2</sub> scintillator is preferable to the usage of fast plastic scintillators as it allows for the benefit of photopeak calibrations and discrimination while retaining the resolution required to discern between bulk and monovacancy positron lifetimes. This study did not include positron lifetime data using the BaF<sub>2</sub> scintillators as although the timing spectra did look reasonable in comparison to the fast plastic timing spectra, the energy spectra observed using the BaF<sub>2</sub> scintillators did not appear as expected when comparing to known energy spectra. As observed in Fig. 4.1b, the timing response function appears to give an expected result in comparison to the timing response function generated with the fast plastic scintillator. However, Fig. 3.3b and 3.4b seems to suggest that more studies need to be completed to find an optimal operating voltage and constant fraction delay cable length for the detectors when using the BaF<sub>2</sub> scintillators. Additionally, Fig. 2.11, and 3.12 indicate that the expected photopeaks are heavily smeared as a result of an unexplained large background in the signal.

## 5.2 Recommendations Based Upon Results

The spectrometer has proven itself capable of discerning positron lifetimes in the annealed and unannealed materials. The positron lifetimes for the annealed, or bulk, high-purity materials are found to be in very good agreement with literature values when using the fast plastic scintillators. The positron lifetimes within the unannealed, or defect, high-purity materials seemed to be in reasonable agreement with

current literature values. The next step would be to determine if the spectrometer is capable of discerning differences in measured degrees of damage to a material. Studies would need to be completed to determine a method of inducing or engineering varying and measurable degrees of damage to the surface of a material. It would then be possible to determine the defect damage resolution, if any, that the spectrometer is capable of discerning by means of detecting differences in defect intensity within the materials. This would make the spectrometer extremely effective in quantitative assessment of atomic-scale defects within materials.

The eventual application of this system is to use the system in conjunction with continuous wave (CW) accelerators, such as a Van de Graaff or Pelletron, to determine if it can be used to perform deep-defect scanning of damaged materials. As mentioned in Sec. 2.4.1, positrons emitted from  $^{22}\text{Na}$  sources are only capable of penetrating within the first  $100\ \mu\text{m}$  of the surface of a material. From the experiments performed with this system, it initially appears that the use of the fast plastic scintillator is favored over the  $\text{BaF}_2$  scintillator for CW accelerators. Preliminary tests were conducted with the  $\text{BaF}_2$  scintillators and the Pelletron which indicated that due to the energy of the resultant gammas from the  $^{27}\text{Al}(p, \gamma)^{28}\text{Si}$  reaction, the anode output voltages were observed to be in excess of -5 V, potentially damaging the discriminators while allowing undesired signals to pass through to the TAC. Additionally, the gammas produced in the  $^{27}\text{Al}(p, \gamma)^{28}\text{Si}$  reaction are above the minimum thresholds for pair production within the  $\text{BaF}_2$  scintillators set forth in Fig. 2.5b, indicating a small potential for the presence of single and double escape peaks in the spectrum as expected from Sec. 2.6.1. As the detector resolution with the  $\text{BaF}_2$  scintillators is on the order of 15% with the ultraviolet transmission optical grease and nearly 30% without, these escape peaks, in addition to the resultant photopeaks from the range of gammas produced in the  $^{27}\text{Al}(p, \gamma)^{28}\text{Si}$  reaction, would be significantly smeared across the resultant spectrum. This spectrum smearing may make calibrations and signal processing difficult using traditional methods. These issues will need to be resolved in future studies involving the  $\text{BaF}_2$  scintillators and continuous wave accelerator.

## 5.3 Future Work

The construction of the positron annihilation lifetime spectrometer is an important first step in the measurement of positron lifetimes within materials. With recent advances in nuclear instrumentation and radiation detection technologies and techniques, improvements can be made to the spectrometer timing and energy resolution. The spectrometer software and hardware can be improved to reduce false coincidence rates and reduce spectrometer deadtime. This in turn creates cleaner positron lifetime spectra, making the extraction of positron lifetimes and defect densities in materials more accurate.

Further investigations into the MPA-NT and LT10 software should be completed. Although not used in this study, it is possible to capture the event timestamps of the two energy channels from within the MPA-NT software. Through sophisticated software algorithms, it should be possible to evaluate the energy channel timestamps and compare them with the timing coincidence event timestamps, allowing for the rejection and correction of false timing coincidence events. While this will reduce the count rate, it will produce a cleaner spectra with which to perform data analysis.

Theoretical Monte Carlo simulations may be completed using either MCNPX or GEANT to determine the positron production rates within the samples, the gamma production yields of the  $^{27}\text{Al}(\text{p},\gamma)^{28}\text{Si}$  reaction based upon available beam energies, and the effect of shielding on improving the signal to noise ratio. Simulations may be completed which demonstrate a more advantageous proton-capture reaction beyond the  $^{27}\text{Al}(\text{p},\gamma)^{28}\text{Si}$  reaction for use with accelerator experiments. The use of such simulations would be an aid to develop better experimental designs for both source-based and AG-PAS experiments, as well as potentially reducing the time necessary to generate enough statistics in the positron lifetime spectra for data analysis.

Several groups of recent years have found success with the Hamamatsu R3377 photomultiplier tubes, while other research groups have begun using micro-channel plate photomultipliers (MCP), which offer a much faster rise time and a smaller transit time spread than traditional photomultiplier tubes while being sensitive to position. This allows for greater spatial resolution for the purposes of imaging [15, 17, 18]. In using traditional photomultiplier tubes, studies have been completed which utilize custom built voltage dividers to optimize timing resolution with promising results [1].

It is recommended by various groups to use two CFDD modules instead of a CFD

/ CFDD module setup to reduce the inclusion of higher energy gammas which may be detected by the photomultiplier tube [17, 20, 36, 32]. While this study has shown the second CFDD module to not be absolutely critical for source-based experiments, it is necessary in order to complete accelerator-based studies using the  $^{27}\text{Al}(p,\gamma)^{28}\text{Si}$  reaction. The discriminator window is necessary to isolate the 511 keV and 1.78 MeV TAC START and STOP signals for inclusion into the resultant positron annihilation lifetime spectra. Otherwise, with only a single CFDD module, the TAC STOP will trigger on any signal resultant from a gamma of energy equal to or greater than 1.78 MeV, increasing the number of background coincidences. For the source-based experiments, the additional CFDD module should help to eliminate any false TAC START signals from cosmic-rays, background gammas, or pulse pile-up by allowing a window to be set on the TAC START signal rather than only a lower discrimination level.

While many research groups continue to use NIMs in positron annihilation lifetime spectrometers, other groups have begun using CAMAC or VME systems [1]. Another group removed most of the electronics and replaced them with a single high-quality digital oscilloscope to perform discrimination and coincidence measurements, providing cited timing resolutions of 144 ps and 119 ps FWHM using single and double stop detector setups [41]. This has the benefit of increasing spectrometer resolution while decreasing deadtime through analysis of pulse-pileup events.

As per the original intentions of this study, additional studies should be completed to study the usage of the BaF<sub>2</sub> scintillators for both source-based and continuous wave accelerator experiments. Cautions should be taken as advised in Sec. 3.3.2 and Sec. 3.6.2 when using the BaF<sub>2</sub> scintillators to prevent damage to the spectrometer electronics. Once a viable method for the use of the BaF<sub>2</sub> scintillators has been established, it will be possible to trigger the TAC START and TAC STOP signals using the more precise photopeaks. It is the hope for future studies that once the technical issues regarding the usage of the BaF<sub>2</sub> scintillators have been overcome, the spectrometer will be capable of matching or exceeding the capabilities found with fast plastic scintillators.

## REFERENCES

- [1] F. Bečvář, J. Čížek, L. Lešták, I. Novotný, I. Procházka, F. Šebesta, “A High-Resolution BaF<sub>2</sub> Positron-Lifetime Spectrometer and Experience with its Long-Term Exploitation” Nuclear Instruments and Methods A 443, 2000, 557-577.
- [2] Berger, M.J., Hubbell, J.H., Seltzer, S.M., Chang, J., Coursey, J.S., Sukumar, R., Zucker, D.S., and Olsen, K. (2010), *XCOM: Photon Cross Section Database*. Version 1.5. [Online] Available: <http://physics.nist.gov/xcom>. National Institute of Standards and Technology, Gaithersburg, MD.
- [3] A. Bisi, G. Faini, E. Gaitti, and L. Zappa. Phys. Rev. **5**, 2 (1960).
- [4] W. Brandt and R. Paulin. Phys. Rev. B. **15**, 5 (1977).
- [5] L. Brown and L. Hoddeson. *The Birth of Particle Physics*. Cambridge University Press, 1983.
- [6] M. Charlton and J.W. Humbertson. *Positron Physics*. Cambridge University Press, 2001.
- [7] S.Y.F. Chu, L.P. Ekström, and R.B. Firestone. The Lund / LBNL Nuclear Data Search. Version 2.0, February 1999. <http://nucleardata.nuclear.lu.se/NuclearData/toi/>
- [8] Das, A. and T. Ferbel. *Introduction to Nuclear and Particle Physics*. 2nd ed. New Jersey: World Scientific, 2003. Print.
- [9] C. Dauwe, J. De Baerdemaeker, N. Djourelov, N. Laforest and B. Van Waeyenberge. “Is Kapton\* Really That Simple?” Acta Phys Polon A 2008; **113**: 1315-9.

- [10] G. Dlubek, R. Buchhold, CH. Hübner, A. Nakladal, K. Share. "Local Free Volumes in Boron-Bombarded Kapton Polyimide: A Positron Lifetime Study." *J. Polym. Sci. Part B: Polym. Phys.* **37**, 2539 (1999).
- [11] M. J. Fluss, L. C. Smedskjaer, M. K. Chason, D. G. Legnini, and R. W. Siegel, *Phys. Rev. B* **17**, 3444 (1978).
- [12] Gilmore, Gordon and John Hemingway. *Practical Gamma Ray Spectroscopy*. New York: John Wiley & Sons, 1995. Print.
- [13] Griffiths, David. *Introduction to Elementary Particles*. 2nd rev. ed. Weinheim, Germany: Wiley-VCH, 2008. Print.
- [14] Hamamatsu Photonics K.K. *Photomultiplier Tubes: Basics and Applications*. 3rd ed. 2006. Print.
- [15] Hamamatsu Photonics K.K., <http://www.hamamatsu.com/>.
- [16] C.H. Hodges, *Phys. Rev. B* **25**, 5 (1970).
- [17] A. Howie, Positron Annihilation Lifetime Spectroscopy of Metals, Semiconductors, Thin Films and Zeolites, Bachelors thesis, Centre for Antimatter-Matter Studies at the School of Physics, University of Western Australia, 2009.
- [18] V. Irby. "Picosecond Timing Resolution Detection of Gamma Photons Utilizing Microchannel-plate Detectors: Experimental Tests of Quantum Nonlocality and Photon Localization." Department of Physics, University of South Alabama, 2004.
- [19] Kansy, Jerzy and D. Giebel. "Study of defect structure with new software for numerical analysis of PAL spectra." *J. Phys.: Conf. Ser.* 265, 1, 2011.
- [20] Andrzej Karbowski, Janusz D. Fidelus, Grzegorz P. Karwasz. "Testing an Ortec Lifetime System." *Materials Science Forum* Vol. 666, 2011, 155-159.
- [21] Knoll, Glenn F. *Radiation Detection and Measurement*. 3rd ed. Wiley, 2000.
- [22] T. Kohonen. "Positron Lifetime Measurements with Homogenized Sources in Metals. Positron Annihilation. Proceedings of the Conference Held at Wayne State University on July 27–29, 1965. Ed. A. T. Stewart and L. O. Roellig. New York: Academic Press, 1967. 277-280.

- [23] A.J. Koning and D. Rochman. "TALYS-based Evaluated Nuclear Data Library." TANDL-2009. OECD Nuclear Energy Agency. [www.oecd-nea.org/janis/](http://www.oecd-nea.org/janis/)
- [24] Krane, Kenneth. *Introductory Nuclear Physics*. New York: Wiley, 1988. Print.
- [25] Leo, William R. *Techniques for Nuclear and Particle Physics Experiments: A How-to Approach*. 2nd rev. ed. New York: Springer-Verlag, 1994. Print.
- [26] I.K. Mackenzie, T. L. Khoo, A. B. McDonald and B.T.A. McKee. "Temperature Dependence of Positron Mean Lives in Metals." *Phys Rev. Letters*, **19**, 19 (1967).
- [27] I.K. Mackenzie. "The Doppler-Broadened Annihilation Lineshape as an Indicator of Defects in Metallic Latices." *Physics Letters A*, Volume 30, Issue 2, 1969. 115-116.
- [28] J.D. McGervey, J. Vogel, P. Sen, C. Knox, "Time resolution measurements with an improved discriminator and conical scintillators." *Nuclear Instruments and Methods* 143, 1977, 435-439.
- [29] P.E. Mijnarends "Electron Momentum Densities in Metals and Alloys Positrons in Solids. Ed. P. Hautojrvi. New York: Springer-Verlag, 1979. 25. Print.
- [30] S. Mukhopadhyay. "Plastic gamma sensors: an application in search of radioisotopes." *Proc. SPIE* 5198, 62 (2004).
- [31] National Nuclear Data Center. Brookhaven National Laboratory. "Evaluated Nuclear Data File." Ver. VII.1, <http://www.nndc.bnl.gov/>
- [32] ORTEC. Modular Electronic Instruments. AMETEK, 2010. <http://www.ortec-online.com/Solutions/modular-electronic-instruments.aspx>
- [33] I. Øverbø, K. J. Mork, and H. A. Olsen. *Phys Rev. A* **8**, 2 (1973).
- [34] T. J. Paulus. "Performance Characteristics of Eighteen Positron Lifetime Spectrometers." 1991.
- [35] Nieminen, R. M. and Manninen, M. J. "Positrons in Imperfect Solids: Theory." *Positrons in Solids*. Ed. P. Hautojrvi. New York: Springer-Verlag, 1979. 145. Print.

- [36] I. Procházka. "Positron Annihilation Spectroscopy." Materials Structure, 8, 2, 2001.
- [37] M. J. Puska and R. M. Nieminen. "Theory of positrons in solids and on solid surfaces." Rev. Mod. Phys., 66(3):841897, 1994.
- [38] J. Ralph, Utilizing the  $^{27}\text{Al}(\text{p}, \gamma) ^{28}\text{Si}$  Reaction for Positron Annihilation Analysis, Masters thesis, Idaho State University.
- [39] J. M. Campillo Robles, E. Ogando and F. Plazaola. "Positron lifetime calculation for the elements of the periodic table." J. Phys.: Condensed Matter **19** (2007).
- [40] Saint-Gobain, <http://www.detectors.saint-gobain.com/>
- [41] H. Saito, Y. Nagashima, T. Kurihara, T. Hyodo. "A New Positron Lifetime Spectrometer Using a Fast Digital Oscilloscope and BaF<sub>2</sub> Scintillators." Nuclear Instruments and Methods A 487, 2002, 612-617.
- [42] A. Seeger, F. Barnhart, and W. Bauer, in *Positron Annihilation*, edited by L. Dorikens-Vanpraet, M. Dorikens, and D. Segers. World Scientific, Singapore, 1989, p. 275.
- [43] P. A. Sterne and J. H. Kaiser. Phys Rev. B **43**, 17 (1991).
- [44] L. Tchelidze, Positron Annihilation Energy and Lifetime Spectroscopy Studies on Radiation Damaged Stainless Steel 316L and Steel 9Cr1Mo, Masters thesis, Idaho State University, November 2005.
- [45] H Weisberg and S. Berko. Phys. Rev. **154**, 2 (1967).